METAMATERIAL BASED OPTICAL DEVICES: DESIGN AND ANALYSIS

A Thesis Submitted

In Partial Fulfilment of the Requirements

for the Degree of

DOCTOR OF PHILOSOPHY

by

Ankit
(Roll No. 2K20/PHD/AP/03)

Under the Joint Supervision of

PROF. RAVINDRA KUMAR SINHA

DR. KAMAL KISHOR

Professor
Department of Applied Physics
Delhi Technological University

Assistant Professor
Department of Applied Physics
Delhi Technological University

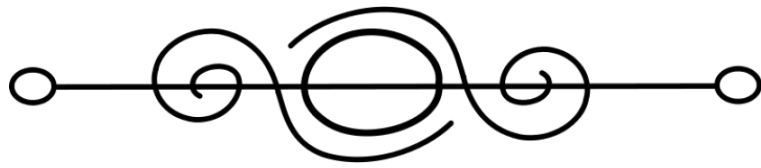**Department of Applied Physics**

DELHI TECHNOLOGICAL UNIVERSITY

(Formerly Delhi College of Engineering)

Shahbad Daulatpur, Main Bawana Road, Delhi-110042, India

April 2025

Dedicated

To My

Beloved Parents

DELHI TECHNOLOGICAL UNIVERSITY

(Formerly Delhi College of Engineering)

Shahbad Daulatpur, Main Bawana Road, Delhi-42

<u>CANDIDATE'S DECLARATION</u>
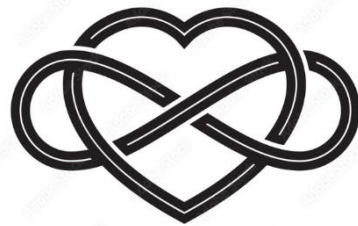
I ____**Ankit**____ hereby certify that the work which is being presented in the thesis entitled "**Metamaterial based Optical Devices: Design and Analysis**" in partial fulfillment of the requirements for the award of the Degree of Doctor of Philosophy, submitted in the Department of **Applied Physics   ,** Delhi Technological University is an authentic record of my own work carried out during the period from __**August 2020**__ to ____**April 2025**____ under the supervision of **Prof. Ravindra Kumar Sinha and Dr. Kamal Kishor, Department of Applied Physics, DTU.**

The matter presented in the thesis has not been submitted by me for the award of any other degree of this or any other Institute.

.

Candidate's Signature

Ankit

(2K20/PHD/AP/03)

This is to certify that the student has incorporated all the corrections suggested by the examiners in the thesis and the statement made by the candidate is correct to the best of our knowledge.

Signature of Supervisor (s)   **Signature of External Examiner**

DELHI TECHNOLOGICAL UNIVERSITY

(Formerly Delhi College of Engineering)

Shahbad Daulatpur, Main Bawana Road, Delhi-42

CERTIFICATE BY THE SUPERVISOR(s)

Certified that __**Ankit**__ **(2K20/PHD/AP/03)** has carried out the research work presented in this

thesis entitled __**"Metamaterial based Optical Devices: Design and Analysis"**__ for the award

of __**Doctor of Philosophy**__ from Department of Applied Physics, Delhi Technological University,

Delhi, under our supervision. The thesis embodies results of original work, and studies are carried

out by the student himself and the contents of the thesis do not form the basis for the award of any

other degree to the candidate or to anybody else from this or any other University/Institution.

Prof. Ravindra Kumar Sinha   **Dr. Kamal Kishor**

(Supervisor)   (Joint-Supervisor)

Professor   Assistant Professor

Department of Applied Physics   Department of Applied Physics

Delhi Technological University   Delhi Technological University

Date: 24-04-2025

ACKNOWLEDGEMENTS

A heartfelt thanks to my special friend, *Dr. Anu*, whose constant inspiration and support have been invaluable throughout my Ph.D. journey. Your unwavering encouragement and insightful discussions have given me the strength to persevere through challenges.

I am indebted to some of my dear friends **Dr. Jyoti,** *Ms. Komal Verma, Ms. Sangeeta and Ms. Seema Mor* for influencing me in a positive way and for their moral support and motivation, which drives me to give my best.

I would like to acknowledge all the teachers I learnt from since my childhood specially from *Satyanand Public School, Gohana and Hindu College, Sonipat*, I would not have been here without their guidance, blessings, and support.

Further, I would like to pay high regards to my father *Dr. Bhim Singh* and my mother *Mrs. Saroj Devi,* they always encouraged me to explore my potential and pursue my dreams. They helped me a lot to reach this stage in my life. I would also like to thank my brother *Dr. Yogesh* and sister-in-law *Dr. Parul*, along with my niece *Nishthi* and nephew *Daivik*, provided a stress-free and supportive environment, and I am grateful for their presence in my life.

Above all, my life partner, *Mrs. Bhawna*, has been my pillar of strength throughout my life and PhD journey. Her unwavering support, patience, and encouragement have been my greatest source of motivation. Through every challenge and triumph, she has stood by my side, offering her wisdom, love, and sacrifices to ensure I could pursue my dreams. Her belief in me has given me the confidence to push forward, even in the most difficult times. Without her, this journey would not have been possible, and for that, I am forever grateful.

Date: 24-04-2025   **(Ankit)**

Place: Delhi

ABSTRACT

Metamaterials possess distinctive and valuable characteristics that are not achievable in naturally occurring materials. This exceptional property of metamaterials contributes significantly to the advancements in various scientific and technological domains. This thesis delves into the author's extensive research on metamaterials, encompassing innovative application-specific designs and uses of existing metamaterial designs across a broad electromagnetic spectrum.

The exploration spans from positive to negative refractive indices, including the zero-index region, revealing unprecedented properties in zero refractive index metamaterials (ZIMs). One significant aspect of this research involves the utilization of an all-dielectric metamaterial to create impeccable reflectors for both visible and infrared wavelengths. This is achieved by leveraging Electric Dipole (ED) and Magnetic Dipole (MD) resonance, which are essential for controlling light-matter interactions at the nanoscale.

Notably, the thesis highlights two key contributions to the field of zero-index metamaterials. The first is a triple-band application in the microwave C, X, and Ku bands using a zero-index metasurface. This innovative design offers potential solutions for enhancing performance in microwave communications and radar systems. The second contribution is a unique design featuring Quadrupole plasmon resonance for refractive index sensing applications. This design provides a highly sensitive method for detecting changes in the refractive index, which is crucial for various sensing technologies. The research covers diverse metamaterial types and domains, suggesting novel designs and applications with potential in optical and wireless communication, and sensing. These applications demonstrate the transformative impact that metamaterials can have on multiple industries. Additionally, the work explores optical metamaterials, specifically hybrid metal-dielectric metamaterials with wide bandwidth designed for applications in wireless and Wi-Fi communication. These hybrid metamaterials offer significant advantages in terms of performance and efficiency, showcasing the vast possibilities that metamaterials offer for future technological advancements.

Overall, this thesis provides a comprehensive analysis of metamaterial-based optical devices, presenting new designs and insights that push the boundaries of what is possible with engineered materials. The findings and contributions presented in this work have the potential to drive innovation and pave the way for the development of next-generation technologies in various fields.

LIST OF PUBLICATIONS

Publications in Refereed International Journals (Thesis)

[1] **Ankit,** K. Kishor, R.K. Sinha, Design and analysis of wavelength tunable metamaterial reflector, **Results Opt.** 10 (2023) 100366.

[2] **Ankit,** K. Kishor, R.K. Sinha, Design, fabrication, and characterization of epsilon negative and near-zero index metasurface, **Appl. Phys. A**. 130 (2024) 98 **(I.F.= 2.7)**.

[3] **Ankit**, K. Kishor, R.K. Sinha, SOI Based metasurface for broadband perfect reflection in visible spectrum, **J. Opt.** 26 (2024) 045101 **(I.F.= 2.1)**.

[4] **Ankit,** M.N. Baitha, K. Kishor, R.K. Sinha, Quadrupole mode plasmon resonance enabled dual-band metamaterial for refractive index sensing application, **J. Appl. Phys.** 136 (2024) 023104 **(I.F. = 2.7)**

[5] **Ankit**, K. Kishor, R.K. Sinha, Design of wide bandwidth metamaterial for biosensor and wireless application, **Phys. Scr.** 100 (2025) 035503 **(I.F. = 2.6)**

[6] **Ankit**, K. Kishor, R.K. Sinha, Design and analysis of Far-Infrared Metamaterial Perfect Absorber with sensing applications, **Appl. Opt.** 63, 8994-9001 (2024) **(I.F. = 1.7)**

Publications in Refereed International Conferences and workshops (Thesis)

[1] **Ankit**, K. Kishor, and R. K. Sinha, "ENZ metamaterial for X-band in the microwave regime," in Frontiers in Optics + Laser Science 2022 (FIO, LS), Technical Digest Series (Optica Publishing Group, 2022), paper JTu4B.60.

[2] **Ankit .,** Kamal Kishor, Ravindra Kumar Sinha, "Design and analysis of multiband metamaterial in microwave regime," Proc. SPIE 12568, Metamaterials XIV, 125680V (6 June 2023).

International Conferences Attended/Participated

1. "**2022 Frontiers in Optics + Laser Science**" Virtual Conference and presented poster entitled "ENZ metamaterial for X-band in the microwave regime" online during 17th - 20th October 2022.

2. High-End workshop (Karyashala) on "**Recent Advances in Microwave & Millimeter-Wave Communication Technologies**" sponsored by SERB organized by the Department of Electrical Engineering, IIT Indore from 21st - 27th November, 2022.

3. A technical talk on **"Stronger Glass Products and an Overview of IYoG (International Year of Glass)"** organized by Department of Applied Physics, Delhi Technological University in association with The All-India Glass Manufacturers' Federation (AIGMF) on 30th November 2022.

4. One Day National Seminar on "Implementation of NEP-2020 in special reference to innovation & entrepreneurship" organized by the Department of Applied Physics, Delhi Technological University (DTU) on 24th February, 2023.

5. "**SPIE OPTICS+OPTOELECTRONICS 2023**" International conference in Prague, Europe during 23rd -27th April, 2023 and successfully presented the poster presentation titled "Design and analysis of multiband metamaterial in microwave regime".

6. One Day National Workshop on "**Ascertaining A Skill Centre for Glass and Glazing (ASCGG-2023)** Bringing Industry and Academia Together organized by Department of Applied Physics, DTU on 11th August, 2023.

7. "**Optica Student Leadership Program-2023**" in Tacoma, Seattle US during 08th - 12th October 2023.

8. "**International Conference on Atomic, Molecular, Material, Nano and Optical Physics with Applications**" International conference in DTU during 20th - 23rd Dec 2023 and successfully presented the poster presentation titled "A Comprehensive Design and study of microwave Zero Index metasurface".

9. High-End workshop (Karyashala) on "**Opportunistic control of Advances in Antenna Design**" sponsored by SERB organized by the Department of Electrical Engineering, NIT Tiruchirappalli from 11th - 17th March, 2024.

TABLE OF CONTENTS

Title	Page No.

LIST OF TABLES
_____

LIST OF FIGURES

LIST OF ABBREVIATIONS

_____

- ADS: Advanced Design Simulation
- CAD: Computer-Aided Design
- CNC: Computer numerical control
- DBEM: Dual-band electric meta-atom
- DNG: Double negative
- DSRR: Double split ring resonator
- DUT: Device Under Test
- ED: Electric dipole
- EM-MMs: Electromagnetic-metamaterials
- EMR: Effective medium ratio
- EMT: Effective medium theory
- ENZ: Epsilon Negative
- FEM: Finite Element Method
- FSS: Frequency Selective Surface
- LHM: Left-handed metamaterial
- MD: Magnetic dipole
- MNG: μ-negative
- MSRR: Metallic split-ring resonators
- MTM: Metamaterial
- NIM: Negative index material
- NRW: Nicolson-Ross Wier
- NZI: Near-Zero Index
- PCB: Printed circuit board
- PEC: Perfect electric conductor

- PMC: Perfect magnetic conductor
- RI: Refractive index
- RIU: Refractive Index Unit
- SNG: Single-negative
- SOI: Silicon on Insulator
- SOLT: Short-open-load-through
- SPP: Surface plasmon polaritons
- SPP: Surface Plasmon Polaritons
- SRR: Split ring resonator
- VNAs: Vector Network Analyzers
- ZIMs: Zero-index metamaterial

CHAPTER- 1

CHAPTER 1: INTRODUCTION AND BACKGROUND

1.1 INTRODUCTION

Electromagnetic metamaterials (EM-MMs) are composed of subwavelength elements and can be tailored to manipulate light in specific ways. The optical properties of these materials are dependent on the geometry of their constituent elements, making them highly scalable and applicable across various parts of the electromagnetic spectrum. They have proven to be effective in diverse applications, particularly in the development of efficient imaging devices for long wavelengths. This thesis aims to demonstrate the practicality of using metamaterials in real-world products. Furthermore, the study of metamaterials provides valuable insights into electromagnetic theory.

1.2 ELECTROMAGNETIC THEORY

1.2.1 Maxwell's Equations

To delve into the physics of metamaterials, it's essential to provide a concise introduction to electromagnetic theory. Maxwell's equations, foundational for understanding all interactions between light and matter, were synthesized by James Clerk Maxwell in 1865, consolidating contributions from various physicists in the early 19th century [1]. Although Maxwell's equations exist in various formulations, we present them here for a linear, isotropic medium:

$$\nabla . E = \frac{\rho_v(t)}{\varepsilon_0} \qquad \qquad 1.1$$

$$\nabla . B = 0 \qquad \qquad 1.2$$

$$\nabla \times E = -\frac{\partial B}{\partial t} \qquad \qquad 1.3$$

$$\nabla \times B = J(t) + \frac{\varepsilon_0}{\partial t} \frac{\partial E}{\partial t} \qquad \qquad 1.4$$

where, $\nabla = \left[\frac{\partial}{\partial x}, \frac{\partial}{\partial y}, \frac{\partial}{\partial z} \right]$, ρ_v and J is the density of charge and surface current, respectively.

These equations represent the microscopic manifestation of Maxwell's equations, accounting for densities of total charges ρ_v and currents (J) at the atomic level. These sources of excitation play a crucial role in determining experimental observations of the electric field (E) and magnetic induction (B). The vacuum dielectric constant (ε_0) is also a factor in these equations. Electromagnetic wave propagation occurs through the dynamic interplay of the third and fourth equations, where varying electric fields lead to varying magnetic fields, and vice versa. This perpetual phenomenon allows for the propagation of electromagnetic waves. The electric permittivity and magnetic permeability of different materials are influenced by the interaction of light with matter.

1.2.2 Characteristics of a Wave Traveling Through a Medium

The correlation between Maxwell's equations and constitutive relations establishes a link between the microscopic interactions of charges with dynamic fields and the macroscopic optical properties of media, represented by parameters like ε and μ. Furthermore, when we substitute the typical form of an oscillating electromagnetic wave into Maxwell's equations (1.1-1.4), we can deduce various characteristics of the electromagnetic waves propagating through the medium. One such derivation involves establishing the dispersion relation between the wavevector k and angular frequency ω:

$$k^2 = \omega^2 \varepsilon \mu \qquad \qquad 1.5$$

Expressing this in terms of the velocity of electromagnetic waves traversing a medium, it becomes evident that the speed of light is diminished by a factor of n:

$$v = \frac{c}{n} \qquad \qquad 1.6$$

If an electromagnetic wave consists of multiple wave vectors, each phase front will exhibit its own velocity:

$$v_p = \frac{\omega}{k} \qquad \qquad 1.7$$

known as the phase velocity. The wave packet will travel with speed defined as the group velocity:

$$v_g = \frac{d\omega}{dk}$$

<div align="right">1.8</div>

It is important to recognize that in dispersive media, various spectral elements travel at varying speeds, leading to the accumulation of a phase difference. This typically leads to distortion in the wave packet [2].

1.3   INTRODUCTION TO METAMATERIALS

Metamaterials are customized electromagnetic materials made up of subwavelength elements, whose effective optical properties (electric permittivity $\varepsilon\,(\omega)$ and magnetic permeability $\mu\,(\omega)$) are determined by the geometry of their constituents. Typically composed of unit cells, each on the order of $\lambda/10$ or smaller, arranged in a large array, these materials interact with electromagnetic waves as an effective medium with optical constants rather than diffracting off individual elements. The effective electric permittivity ($\varepsilon_{eff}(\omega)$) and magnetic permeability ($\mu_{eff}(\omega)$) of metamaterials are predominantly influenced by unit cell geometry rather than band structure or chemistry, making them scalable across a broad electromagnetic spectrum, from radio frequencies to the optical and visible regimes [3,4].

While the use of artificial elements in achieving specific electromagnetic responses dates back to Jagadish Chunder Bose's experiments in 1898 [5], metamaterials gained prominence in the 1940s with the development of Kock's metallic delay lens [6] at Bell Labs. Artificial dielectrics and engineered media with negative $\varepsilon\,(\omega)$ have been known since the 1960s [7,8].

However, the pivotal moment in metamaterial history is often considered to be John Pendry's introduction of artificial magnetism in 1999 [9], along with the subsequent numerical study of the first structure exhibiting simultaneously negative $\varepsilon_{eff}(\omega)$ and $\mu_{eff}(\omega)$ [10]. These publications marked a paradigm shift, enabling metamaterials to exhibit more exotic properties over a broader range of the electromagnetic spectrum, including shorter wavelengths.

The breakthrough came with the concept of negative index materials (NIM) introduced by Smith in 2000 [10], where the material simultaneously exhibited negative values of $\varepsilon_{eff}(\omega)$ and $\mu_{eff}(\omega)$,

resulting in an index of refraction ($n_{eff.}(\omega)$) less than zero. This development was a significant stride forward for the field of metamaterials.

1.3.1 History of Negative Refraction

In 1967, Veselago [11] explored materials characterized by both negative permittivity ($\varepsilon < 0$) and negative permeability ($\mu < 0$). Using macroscopic Maxwell Equations, he forecasted the existence of backward electromagnetic waves exhibiting opposite phases and group velocities. Veselago also delved into unconventional phenomena such as reversed Doppler shift and Cerenkov radiation at obtuse angles. Additionally, he determined that the refractive index should be represented as $n = -\sqrt{\varepsilon\mu}$, indicating that negative refraction occurs when light interfaces with such a medium and air. Expanding on this observation, he suggested that a planar slab made of a medium with $\varepsilon = \mu = -1$ functions as a lens by directing all rays emitted from an object to the focus, located twice the thickness of the lens away.
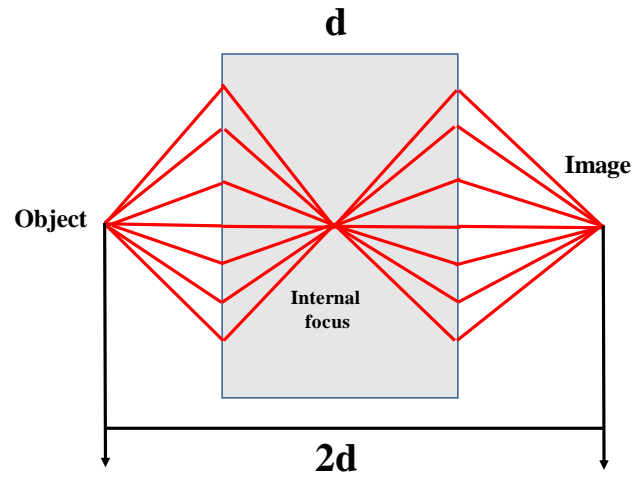
Figure 1.1 A flat lens composed of an $\varepsilon = \mu = -1$ material. It forms an image by refocusing all the light rays emitting from an object through negative refraction.

Veselago was not the originator of the concept of backward waves or negative refraction [12]; H. Lamb in 1904 [13] and Pocklington in 1905 [14] had discussed backward waves on specific mechanical systems. Veselago, however, was the first to propose a negative refractive index and introduce the idea of the flat lens in Figure 1.1. Despite speculating about potential physical systems with simultaneous negative ε and μ, no such material was known at the time, and his theoretical

exploration was deemed "purely formal" [11]. As a result, Veselago's work on the flat lens remained largely unnoticed for almost three decades.

In 1999, Sir John Pendry [9] presented a study on a magnetic material composed of nonmagnetic resonant elements, allowing for a tunable magnetic response at higher frequencies. Among Pendry's various magnetic metamaterials, the double split ring resonator (DSRR) gained significant attention for providing a frequency band with negative $\mu_{eff.}(\omega)$ in the microwave range. This discovery sparked excitement as it opened the possibility of creating a Negative Index Material (NIM). While some earlier research had touched on backward waves and NIM [15], a systematic analysis did not emerge until 1968 when V.G.Veselago proposed that a material with simultaneous negative ε and μ could exhibit unique properties like opposite phase and group velocity, Doppler shift inversion, and Snell's Law reversal [11].

Although negative ε materials, such as metals above the plasma frequency, were common, negative μ materials were rare and did not exist in frequency ranges accessible by negative ε materials [16]. Pendry suggested using an array of thin wires to act as a dilute plasma, shifting the plasma frequency to the microwave region. Thus, through the utilization of these artificial materials, components were identified that exhibited simultaneous negative $\varepsilon_{eff.}(\omega)$ and $\mu_{eff.}(\omega)$ frequency regimes. In 2000, David Smith and collaborators experimentally demonstrated a negative index material by combining two types of constituent elements: an array of thin copper wires to achieve negative $\varepsilon_{eff.}(\omega)$ and an array of DSRRs to achieve negative $\mu_{eff.}(\omega)$ [10].

1.3.2 Effective Medium Theory for Metamaterial

The natural range of permittivity and permeability in conventional materials is limited. At optical frequencies, it's uncommon to find materials with large ε and μ. Landau suggested that the lack of high-frequency magnetic response is due to the incompatibility between small atomic dimensions and macroscopic magnetism [17]. However, Merlin argued that this limitation might not apply to mesoscopic composite structures [18]. Composites of natural materials could potentially have a

broader range of ε and μ if their characteristic length scale of inhomogeneities is much smaller than the wavelength. The homogenization theory, which approximates composites as homogeneous media to calculate ε and μ, can be used to model these metamaterials in macroscopic Maxwell's Equations, giving rise to an effective medium theory (EMT).

Research on metamaterials focuses on two main questions based on the theoretical framework:

(1) What effects and applications are predicted by macroscopic Maxwell's Equations without restrictions on ε and μ?

(2) How can composites be designed and fabricated using available materials to achieve unusual values of ε and μ?

An equally important third question is whether the physical behavior predicted by EMT can be observed experimentally. While the accuracy and generality of macroscopic Maxwell's Equations for conventional materials are confirmed by numerous experiments, the applicability of EMT for metamaterial composites is not fully established. Efforts have been made to develop a general homogenization theory to predict the electromagnetic behavior of macroscopic composites based on their microscopic structure [19].

1.3.3 Classification of Metamaterials

Metamaterials, categorized into one-dimensional, two-dimensional, three-dimensional, exhibit unique optical properties by manipulating their structure. Another type, known as a metasurface, is a two-dimensional planar sheet metamaterial with a thickness significantly smaller than its other two dimensions. Initially, metal-dielectric composites were prominent, enabling phenomena like negative refraction and cloaking but suffered from significant ohmic loss. The pursuit of low-loss alternatives led to all-dielectric metamaterials, based on Mie resonance, with applications in perfect reflection, directive radiation, and wave shaping etc. To analyze shapes beyond this, numerical techniques such as the finite difference time domain method [20,21], finite element method [21,22], and others are required.

Metamaterials can be categorized based on their resonance characteristics, where the scatterer's response is most pronounced at a specific frequency of the incident wave. This resonance occurs when the incident frequency aligns with the natural vibration frequency of the system. Metamaterials demonstrating this property are known as resonant metamaterials, with examples like the split ring resonator (SRR) and wire mesh structures. The SRR, a magnetic meta-atom, exhibits resonant behavior due to its LCR circuit-like nature, with the split in the ring providing capacitive elements and the metal contributing inductance and resistive loss [10,23–28]. In contrast, the wire mesh structure, lacking breaks in its continuous metal wires, does not display resonant behavior as it lacks a capacitive element.

Metamaterials are structures that allow for the customization of optical properties, particularly the refractive index. There are three main types of metamaterials based on their effective refractive index: positive index, negative index, and zero-index metamaterials. In Figure 1.2, the refraction of light is depicted as it exits prisms made of positive, negative, and zero-index materials into the air. The illustration demonstrates that in a positive index medium, the emergent ray follows the usual pattern on the opposite side of the normal, whereas in a negative index prism, it aligns with the incident ray on the same side of the normal. Despite appearing unconventional, this behavior is consistent with Snell's law of refraction.
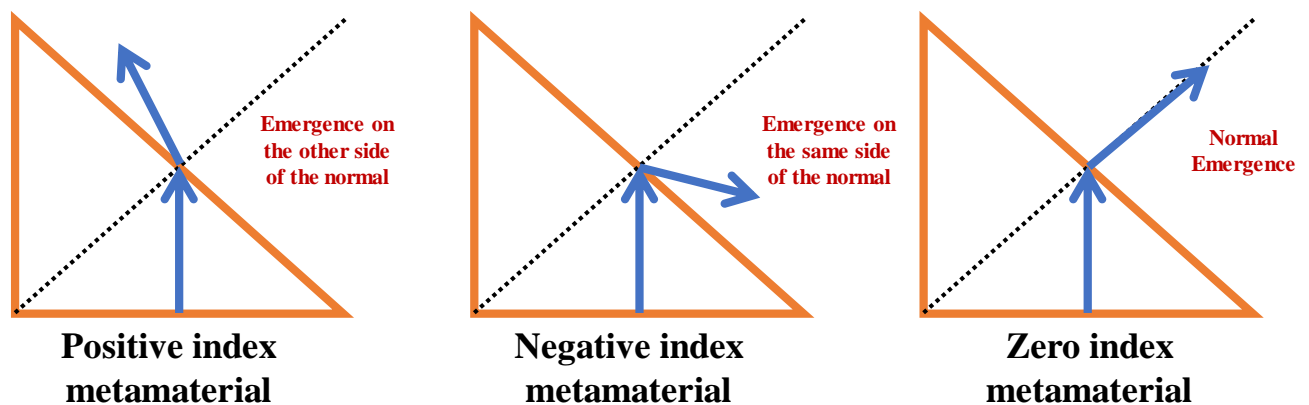
Figure 1.2 Refraction of light by positive, negative and zero index metamaterial.

According to Snell's law, the relationship between the refractive indices (n) and angles (θ) for a prism and its surrounding medium (air, in this case) is given by the equation:

$$n_1 \sin\theta_1 = n_2 \sin\theta_2 \hspace{4cm} 1.9$$

Here, n_1 is the refractive index of the prism, n_2 is the refractive index of the surrounding medium (which is air), and θ is the angle measured with respect to the normal, considered positive in a clockwise direction.

If n_1 is negative, n_2 is 1 (positive), and θ_1 is greater than 0, it is certain that θ_2 is less than 0. Consequently, the emergent ray is on the same side of the normal as the incident ray. Using the same equation (1.9), it can be inferred that when n_1 is 0, regardless of the angle of incidence (θ_1), the angle of emergence is inevitably zero. In other words, when light travels from a medium with a refractive index of zero to a medium with a positive refractive index, the emergent ray always follows the normal, irrespective of the angle of incidence.

Depending on the values of the effective permittivity and effective permeability parameters of the designed metamaterial structure, metamaterial can be categorized as single-negative (SNG), DNG, and double-positive materials. The SNG materials show either negative permeability or negative permittivity, whereas double-negative (DNG) materials show both negative characteristics [29]. Another type of metamaterial category is Near-zero index (NZI) metamaterials which represent a fascinating class of engineered materials that exhibit an effective refractive index close to zero. Unlike conventional materials, which have positive refractive indices, these metamaterials have the remarkable ability to manipulate light in unprecedented ways. By harnessing their unique optical properties, these metamaterials have the potential to revolutionize various fields, from optics and photonics to telecommunications, imaging and cloaking [30]. By manipulating the geometric arrangement and composition of the metamaterial unit cells, it is possible to engineer the effective permittivity and effective permeability of these structure.

1.4 FABRICATION OF METAMATERIALS

After determining the optimal geometric parameters of the metamaterial, various fabrication methods are available based on the structure's size and complexity, especially at microwave frequencies where

unit cell sizes are typically in the range of hundreds of microns or larger. These methods include printed circuit board (PCB) technology [31] and 3-D printing. The fabrication process initiates with the creation of a design layout using Computer-Aided Design (CAD) software, serving as the blueprint for the metamaterial structure. Subsequently, the design is transferred to a screen or mask for PCB Technology. Material deposition onto the substrate is carried out using screen printing, a method for depositing materials onto substrates, where the desired material is applied according to the design pattern. Etching is then employed to refine the metamaterial structure's geometry by removing excess material from the substrate. The final stages involve cleaning the fabricated metamaterial to eliminate any residues or contaminants left from the fabrication process.

As we transit into the terahertz (THz) frequency range with metamaterials featuring periodicities on the order of tens of microns, traditional PCB techniques become impractical. Instead, photolithographic methods are commonly employed, involving the deposition and patterning of metallic and dielectric layers [32]. Deep-UV photolithography allows for extending this method to metamaterials operating in the infrared range, where unit cells are in the micron range [33]. However, at these wavelengths, serial methods like electron beam lithography [34] and focused ion beam [35] are more prevalent. Various fabrication techniques, including nano-imprint lithography [36] and colloidal nanolithography [37], also exist. While the theoretical principles of metamaterials are applicable across the electromagnetic spectrum, practical challenges hinder their realization beyond the visible range. For instance, achieving subwavelength unit cells requires challenging fabrication of precise features. Additionally, metals can exhibit increased loss at higher frequencies, limiting the high-quality (Q) response in metamaterial structures.

1.5   SIMULATION AND CHARACTERIZATION OF METAMATERIALS

The equations (1.10-1.13) provide a straightforward analysis of how a metamaterial interacts with light by calculating effective electromagnetic parameters, the actual physical processes involved can be more complex. Electromagnetic simulation tools, such as HFSS [38], CST Microwave Studio

[39], and COMSOL Multiphysics [40], offer a mature and accurate means to predict and optimize how metamaterials interact with light before fabrication. These tools can delve into intricate physical mechanisms that are challenging to analyze analytically, such as interelement coupling, bianisotropy, or power loss density. These tools work on Finite element method (FEM) based numerical technique. FEM is employed to approximate solutions for boundary value problems associated with partial differential equations. It involves partitioning the problem domain into diverse shapes and sizes of elements such as triangles and quadrilaterals, catering to specific needs [41]. This adaptable element subdivision methodology positions FEM as the optimal mathematical tool for studying metamaterials and predicting scattering responses accurately. The FEM emerges as the preferred approach for analyzing structures characterized by irregular boundaries and varying precision requirements across the domain [42]. FEM provides high accuracy in predicting electromagnetic responses, especially when dealing with structures where the desired precision varies across the domain. This is main reason to use FEM in this thesis to determine the resonant frequencies for the fabricated structure. Metamaterials, typically large arrays with unit cells much smaller than the operational wavelength, can be simulated on a single unit cell with appropriate boundary conditions.

To align simulation results with experiments, a precise understanding of material properties in the relevant frequency range is crucial. Frequency-dependent models, like the Drude model for metals in the infrared and optical frequencies, are often necessary. The essential process in electromagnetic simulation tools involves discretizing the unit cell and solving Maxwell's Equations for each voxel. The output provides complex scattering parameters S_{11} and S_{21} to the user.

Ziolkowski et al. introduced a mathematical approach to extract effective permittivity, effective refractive index, effective permeability, and impedance using the Nicolson-Ross Weir (NRW) method, widely used for effective parameter extraction. The NRW method utilizes transmission coefficient (S_{21}) and reflection coefficient (S_{11}) to extract $\varepsilon_{\text{eff.}}(\omega), \mu_{\text{eff.}}(\omega),$ $\eta_{\text{eff.}}(\omega)$ and impedance (Z) through simplified equations [43–48]:

$$\varepsilon_{\text{eff.}} = \frac{2}{jk_0 d} \times \frac{(1 - V_1)}{(1 + V_1)} = \frac{c}{j\pi v d} \frac{(1 - S_{21} - S_{11})}{(1 + S_{21} + S_{11})} \qquad 1.10$$

$$\mu_{\text{eff.}} = \frac{2}{jk_0 d} \times \frac{(1 - V_2)}{(1 + V_2)} = \frac{c}{j\pi vd} \frac{(1 - S_{21} + S_{11})}{(1 + S_{21} - S_{11})} \qquad 1.11$$

$$\eta_{\text{eff.}} = \sqrt{\varepsilon_{\text{eff.}} \times \mu_{\text{eff.}}} = \frac{c}{j\pi vd} \sqrt{\left\{ \frac{(S_{21} - 1)^2 - (S_{11})^2}{(S_{21} + 1)^2 - (S_{11})^2} \right\}} \qquad 1.12$$

$$Z = \sqrt{\frac{(1 + S_{11})^2 - S_{21}^2}{(1 - S_{11})^2 - S_{21}^2}} \qquad 1.13$$

In the provided context, the variables are defined as follows:

$$V_1 = |S_{21}| + |S_{11}| \qquad 1.14$$

$$V_2 = |S_{21}| - |S_{11}| \qquad 1.15$$

$$k_0 = \frac{2\pi v}{c} \qquad 1.16$$

d represents the thickness of the metamaterial slab, and c represents the speed of light.

Like the fabrication approach, the method for characterization or configuration relies not only on the operational frequency or wavelength but also on the electromagnetic phenomenon one aims to observe. In the case of microwave frequencies, Vector Network Analyzers (VNAs) are employed for producing and detecting both phase and amplitude signals (expressed as S_{11} and S_{21}), connected to free space through horn antennas.

The process of characterizing and configuring S_{11} and S_{21} measurements involve setting up an antenna test configuration using connectors, RF cables, and calibration standards to ensure accuracy. A Vector Network Analyzer (VNA) is utilized for this purpose. The Device Under Test (DUT), in this case, is a fabricated planar Frequency Selective Surface (FSS), positioned within the test setup. The VNA is responsible for determining both the reflected signal (S_{11}) and the transmitted signal (S_{21}) through the DUT. The VNA connects one port to a transmitting horn antenna and the other port to a receiving horn antenna, with the DUT placed between them. To minimize external interference and reflections, the entire antenna setup is enclosed in an anechoic chamber. Calibration of the VNA

is crucial for accurate measurements, involving the use of short-open-load-through (SOLT) calibration standards connected to the VNA's ports to establish precise reference points.

The VNA generates a swept RF signal transmitted through the DUT, and the transmitted signal is measured in terms of magnitude and phase, expressed in dB. Technology advancements, such as multipliers, extenders, and filters, have expanded this characterization technique to the low terahertz (THz) range, although it is more commonly applied from low radio frequency (RF) frequencies to millimetre-wave regimes. In addition to this method, various other techniques like ellipsometry and optical microscopy exist to characterize metamaterials across the electromagnetic spectrum.

The main objectives of this thesis are-

A. Design and analysis of wavelength tunable metamaterial reflector.

B. Design and analysis of wide bandwidth metamaterial for Wi-Fi and Satellite Applications.

C. Electric field enhancement in ENZ/ZIM metamaterial and its applications.

D. Metasurface for Broadband Perfect Reflection in visible spectrum.

E. Dual band metamaterial for refractive index sensing application.

1.6   OVERVIEW OF THE THESIS

This thesis commences with an introductory exploration of metamaterials in Chapter 1, delving into electromagnetic theory, the historical evolution of negative refraction, and a detailed examination of metamaterial classification, fabrication, simulation, and characterization. Various metamaterial platforms are introduced with specific applications, such as perfect reflectors, satellite communication, and enhanced electromagnetic fields. Subsequent chapters focus on distinct designs and models related to the author's contributions.

Chapter 2 discusses the fabrication and characterization of Epsilon Negative (ENZ) and Near-Zero Index (NZI) metasurfaces. It covers the design geometry, fabrication process, methodology, results, and discussions, along with an equivalent circuit model of the metasurface.

Chapter 3 explores the design and performance of a perfect reflector tunable metamaterial (MTM) optimized for nearly 100% reflection at the resonance wavelength (λ_r) of 1550 nm. The structure exhibits μ-negative (MNG) metamaterial characteristics and a negative effective refractive index at λ_r. The chapter also presents tunability through varying the number of unit cell arrays and using mirror image configurations.

Chapter 4 details the modelling and design of a low-loss all-dielectric metasurface on a Silicon on an Insulator (SOI) substrate for a perfect reflector in the visible spectrum. It demonstrates nearly 100% reflectance and broad perfect reflectance spectrum tuning within the visible region. The tunable characteristics of the all-dielectric metasurface, with variations in gap region 'g', dielectric layer thickness (t_s), and Si resonator thickness (t_m), make it suitable for applications in filters, color printing, slow-light devices, and nonlinear optics.

Chapter 5 focuses on the design and fabrication of a novel MTM structure using copper on an epoxy resin fiber (FR-4) dielectric substrate for refractive index sensing applications. The chapter details the resonance mechanism, experimental measurements, alignment with simulated results, and the MTM structure's potential in sensors, detectors, and optoelectronic devices operating in the GHz region.

Chapter 6 outlines the design of a metamaterial (MTM) structure for wide bandwidth wireless applications in the microwave region, showcasing left-handed characteristics in various frequency bands. The chapter includes parametric and material analysis, evaluation of effective electromagnetic parameters (i.e., effective permeability ($\mu_{eff.}$) effective permittivity ($\varepsilon_{eff.}$) and effective refractive index ($\eta_{eff.}$)) and metamaterial application in technology, concluding with a summary.

Chapter 7 provides insights into the design and analysis of a far-infrared metamaterial perfect absorber with sensing applications. The results demonstrate that the designed structure achieves nearly perfect absorption of transverse electric (TE) polarization at a resonance wavelength of $\lambda_r =$

9.40 μm. This high absorption efficiency, reaching 99.47%, is due to the perfect impedance matching condition, which minimizes reflection at the resonating wavelength.

Finally, Chapter 8 provides a comprehensive summary of the entire research presented in the thesis, along with specific conclusions drawn from the findings. It also suggests avenues for future research and improvements to advance the field.

CHAPTER- 2

CHAPTER 2: EPSILON NEGATIVE AND NEAR-ZERO INDEX METASURFACE

2.1 INTRODUCTION

Metasurfaces have gained considerable attention globally for their distinctive features and potential applications, especially in the microwave frequency spectrum. These artificial structures are designed to exhibit properties not naturally found in materials [49,50]. Constructed as two-dimensional arrays of subwavelength unit cells, metasurfaces achieve desired electromagnetic properties through specific configurations, typically involving periodic arrays of metal-dielectric or metal-dielectric-metal structures on a substrate [51]. The metal components, often in the form of split-ring resonators (SRR) or wire structures, generate the desired electromagnetic response, while dielectric materials control the propagation of electromagnetic waves.

With a metasurface length shorter than the microwave frequency, electromagnetic field calculations allow for the determination of reflection and transmission coefficients [52]. Sub-wavelength metasurfaces are currently a focal point in research due to their unique electromagnetic properties, offering lightweight, compact designs with optimal output properties [53,54]. These properties make them highly desirable and versatile for various applications, such as tunable negative refractive index materials [55], invisibility cloaking [56], microwave antennas [57], refractive index and temperature sensors [58], filters [59–61], wavelength-tunable reflectors [62], energy harvesting techniques [63], absorbers [64], nano absorbers [65], multi-mode propagation filter [66,67] and superlenses [68].

Several researchers have proposed innovative metamaterial structures for diverse applications, spanning L-band, X and Ku-bands, and triple band resonance. In this chapter, a novel metasurface unit cell in the shape of an eye with a CC-SRR design is introduced for triple-band microwave applications. The proposed structure demonstrates characteristics of epsilon-negative (ENG) and negative-zero-index (NZI) in the frequency range of 1-15 GHz. Equivalent circuit modeling using

Advanced Design Simulation (ADS) and experimental measurements align excellently with simulated results. The designed structure exhibits triple resonance frequencies corresponding to the C, X, and Ku-bands, presenting a novel metasurface structure analyzed through experimental, theoretical, and simulated methods.

2.2 FABRICATION AND MODELLING OF THE DESIGNED METASURFACE STRUCTURE

In Figure 2.1 (a), the simulated design of the metasurface unit cell structure is illustrated, while Figure 2.1 (b) displays the fabricated prototype array with the same configuration. The proposed structure includes a circular split ring resonator (CSRR), two interconnected circular shapes, and metallic elements coupled to the two circular shapes. The outer circular SRR is characterized by a split gap 'g' and a resonator width 'w_o'. The interconnected circles feature a gap 'g,' forming an eye with a diameter 'd' at the center of the structure and a resonator width 'w_i' along with four gaps 'c' around the eye shape. The unit cell of the metasurface, measuring 16 mm × 16 mm, is comprised of a copper resonator fabricated in a 6×6 array on an FR-4 dielectric substrate with a thickness (t_s) of 1.6 mm, using an automated base CNC machine as depicted in Figure 2.1 (b). Table 2.1 provides a comprehensive list of all relevant parameters.

The proposed structure is designed and simulated using the Finite Element Method (FEM) through the COMSOL Multiphysics 4.3b simulation tool, as depicted in Figure 2.1 (a). In the simulation, a physics-controlled mesh with an extra fine element size is employed, allowing physics to automatically determine size attributes and sequence operations for creating a mesh tailored to the specific problem. The copper material patch has a thickness (t_m) of 0.35 mm and an electrical conductivity (σ) of 5.8×10^7 S/m [69]. The epoxy resin fiber (FR-4) substrate material is characterized by a dielectric constant (ε_r) of 4.3 and a loss tangent (tan δ) of 0.025 [70]. The dielectric constant signifies the material's capacity to store electrical energy in the presence of an electric field, while the dielectric loss tangent represents the energy dissipated as heat when an electric field is

applied. The high dielectric constant of FR-4 results in more pronounced electric field confinement within the substrate material.
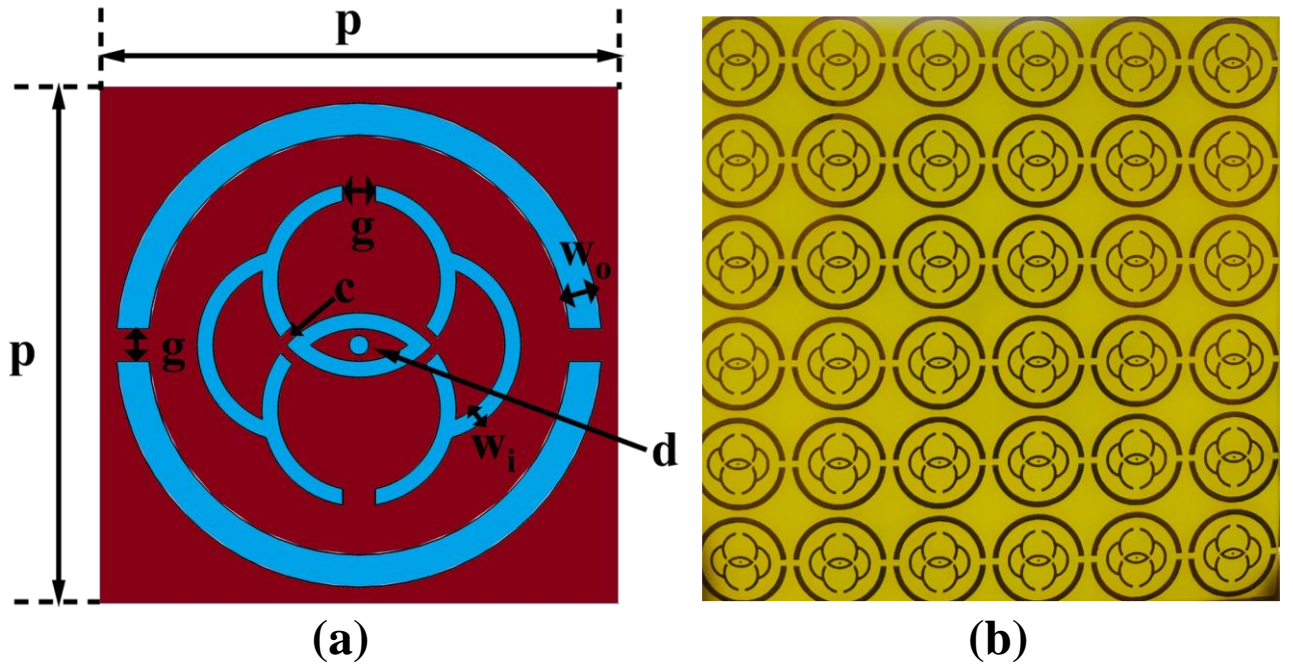
Figure 2.1 (a) Unit cell (Orthogonal view) and **(b)** Fabricated array prototype of the simulated metasurface design.

Table 2.1 The parameters of the fabricated and simulated designed unit cell metasurface structure.

Parameter	Value (mm)	Description
p	16	period of the unit cell
g	1	circular split gap
c	0.3	gap between circular and eye-shaped
d	0.6	diameter of an inner small circle
w_i	0.5	width of the inner resonator
w_o	1	width of the outer resonator

2.3 METHODOLOGY OF THE DESIGN STRUCTURE

Figure 2.2 visually presents the evolution of the design process, starting from the initial phases and culminating in the final assessment of the proposed structure by analyzing the transmission coefficient response across various designs. The evaluation of the design for the proposed system is directed towards fulfilling the requirements for Epsilon negative (ENG) and Near-Zero Index (NZI), while targeting maximum frequency bands. Consequently, several steps are undertaken to attain a

favorable and effective outcome.
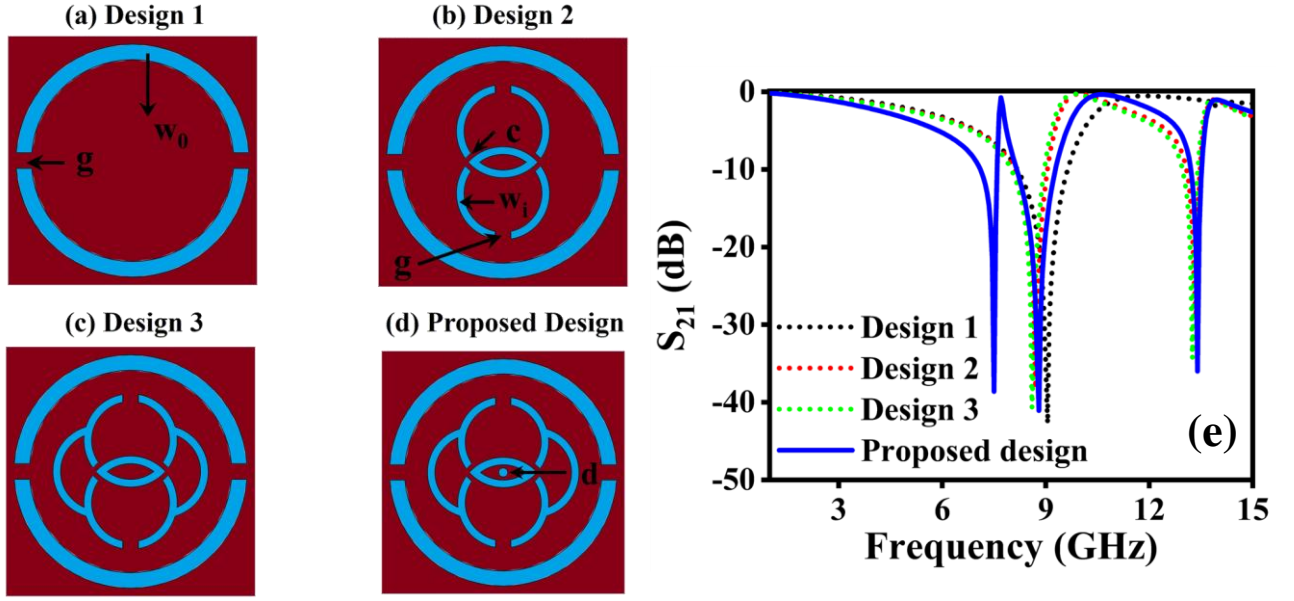
Figure 2.2 Step-by-step design evolution **(a-d)** of the designed CC-SRR metasurface unit cell and **(e)** Transmission coefficient corresponding to the various designed structures using simulation.

The design progression involves distinct steps. In the initial phase (step 1), a Circular Split Ring Resonator (CSRR) is constructed on the dielectric substrate, resulting in two separate parts, portrayed in Figure 2.2 (a). These two circular arcs function as inductors, while the gaps between them act as capacitors. This configuration yields a single resonance frequency within a specific band, approximately 9 GHz, as depicted in Figure 2.2 (e). In the second step, two interconnected circular-shaped SRR circles are formed with a split gap 'g' of 1 mm and a gap 'c' of 0.1 mm, leading to dual-band resonance in the X and Ku bands, as shown in Figure 2.2 (b) and (e). Here, the four circular arcs serve as inductors, including the middle inductor, and the gaps function as capacitors.

Moving to the third step, the CSRRs are coupled together using an arc on the backside (Figure 2.2 (c)), resulting in a shift in resonance within the microwave region. This coupling leads to an increase in the magnitude of S_{21} up to the desired maximum, attributed to the addition of two more capacitors and inductors in this step. However, the triple-band resonance goal is not achieved, as displayed in Figure 2.2 (e). In the final step, a small circle with a diameter 'd' of 0.6 mm is introduced at the center of the resonator, resulting in three frequency bands: C-band (7.5 GHz), X-band (8.8 GHz), and Ku-band (13.4 GHz). This aligns with the intended objective for the proposed design, illustrated in Figure

2.2 (d) and (e). The addition of gaps in all design configurations alters the resonance frequency, influenced by the inclusion of capacitors and inductors in the structure.

2.4 RESULTS AND DISCUSSION

The metasurface unit cell's scattering parameters encompass both the transmission coefficient (S_{21}) and reflection coefficient (S_{11}), and a simulation approach employed a two-waveguide port configuration. In this setup, Port 1 functioned as the signal transmitter, while Port 2 served as the receiver, as illustrated in Figure 2.3 (a). The simulation incorporated periodic boundary conditions, with a perfect magnetic conductor (PMC) along the x-axis and a perfect electric conductor (PEC) along the y-axis. The simulation process involved creating the geometry using predefined parameters, assigning materials to the designed structure, and introducing electromagnetic waves in the frequency domain along with boundary conditions. Subsequently, meshing was applied as per the defined study requirements. Various simulation parameters, including meshing, geometry, and physics, were considered in Finite Element Method (FEM) simulations. The electromagnetic wave propagated vertically along the *z*-axis, enabling accurate simulations and analysis of the electromagnetic behavior of the proposed design. This comprehensive setup allowed for a thorough investigation of the metasurface unit cell's performance through the examination of scattering parameters.

(a)   **(b)**
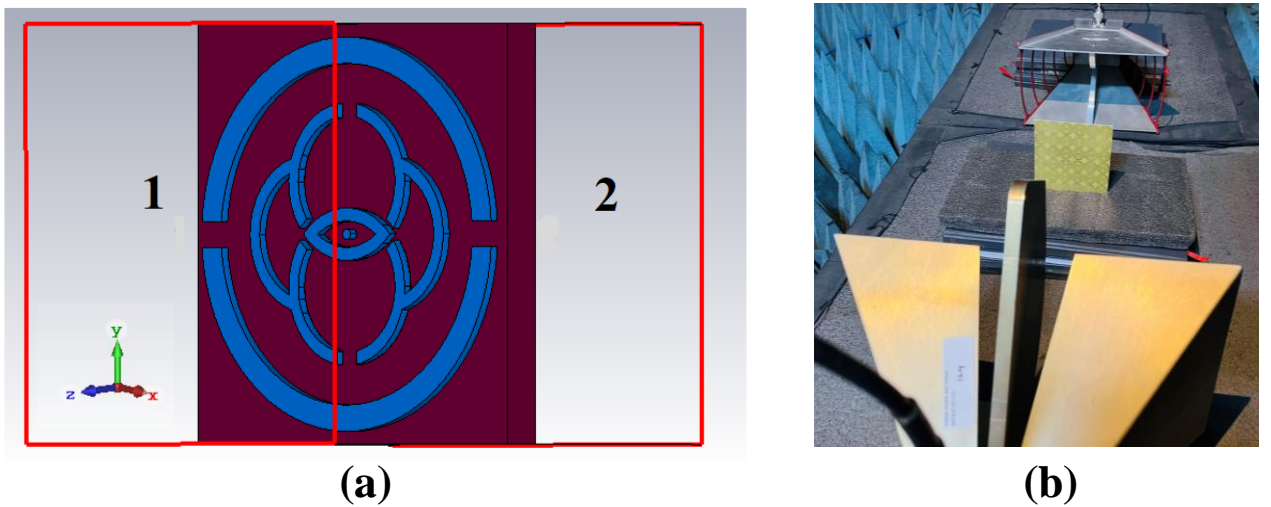
Figure 2.3 (a) Simulation analysis and **(b)** Experimental measurement setup of the designed metasurface.

The experimental setup used for the measurement of S_{21} is an Antenna test setup as shown in Figure

2.3 (b). The whole measurement technique explained briefly in the Section 1.5 of CHAPTER 1: .

Figure 2.4 presents a comparative analysis of the transmission coefficient (S_{21}) response, showcasing (a) the simulation versus the measurement response of the fabricated design and (b) a comparison between two simulation software tools response, namely COMSOL Multiphysics and CST Microwave Studio.
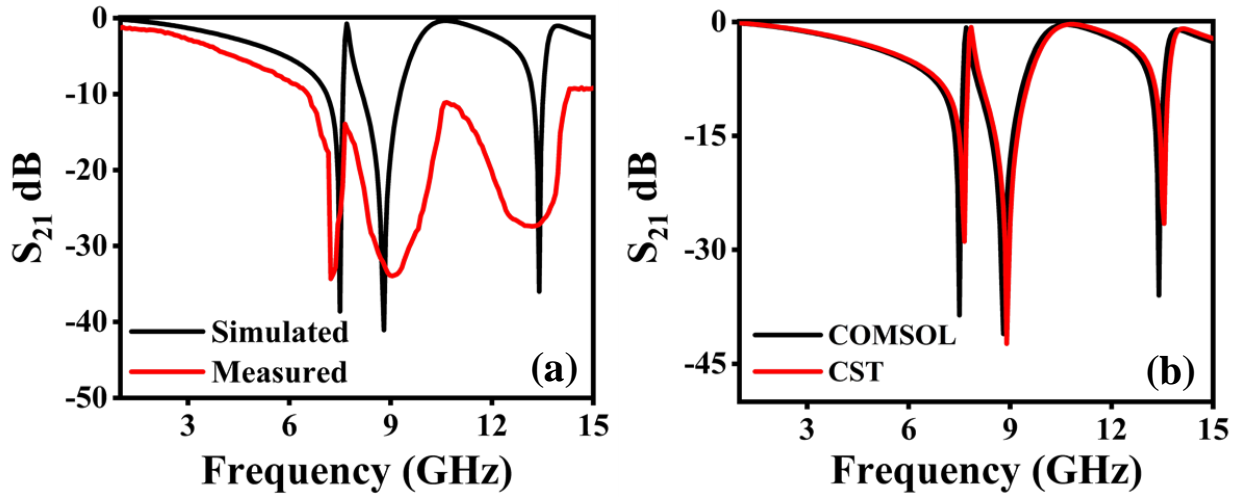
Figure 2.4 Transmission coefficient (S_{21}) of the proposed metasurface structure for **(a)** the Simulated and measured response and **(b)** COMSOL Multiphysics and CST Microwave studio response.

As depicted in Figure 2.4 (a), a noticeable discrepancy exists between the measured and simulated results. This difference could be attributed to factors such as fabrication tolerances, signal leakage, and reflection noise. The experimental setup has inherent constraints, primarily reliant on precise alignment of the two horn antennas to achieve the desired performance. To mitigate potential calibration errors that could impact experimental outcomes, careful calibration of the network analyzer is imperative. The collective impact of these constraints is evident in the measured results, reflecting a slight shift in resonance frequencies. However, both simulated and measured results encompass the C (4-8 GHz), X (8-12 GHz), and Ku (12-18 GHz) bands.

The experimental findings were validated against the simulation results obtained from COMSOL Multiphysics, staying within the experimental limits. In the simulation, the proposed structure demonstrated triple resonance frequencies at 7.5 GHz, 8.8 GHz, and 13.4 GHz, with maximum magnitude values of -38.6 dB, -41.0 dB, and -35.9 dB, respectively. In the experimental results, the resonance frequencies experienced slight shifts to 7.2 GHz, 9.0 GHz, and 13.1 GHz, with maximum

magnitude values of -34.3 dB, -33.9 dB, and -27.3 dB, respectively. Notably, a left shift was observed

between the simulated and experimental results at 7.5 GHz to 7.2 GHz and 13.4 GHz to 13.1 GHz,

while a right shift occurred at 8.8 GHz to 9.0 GHz. The results of S_{21} from both simulation platforms,

COMSOL Multiphysics and CST, were compared and illustrated in Figure 2.4 (b). Remarkably, the

simulation outcomes from both platforms exhibited a high degree of similarity, affirming the

accuracy of the designed structure for the proposed metasurface unit cell in the triple bands (C, X &

Ku).
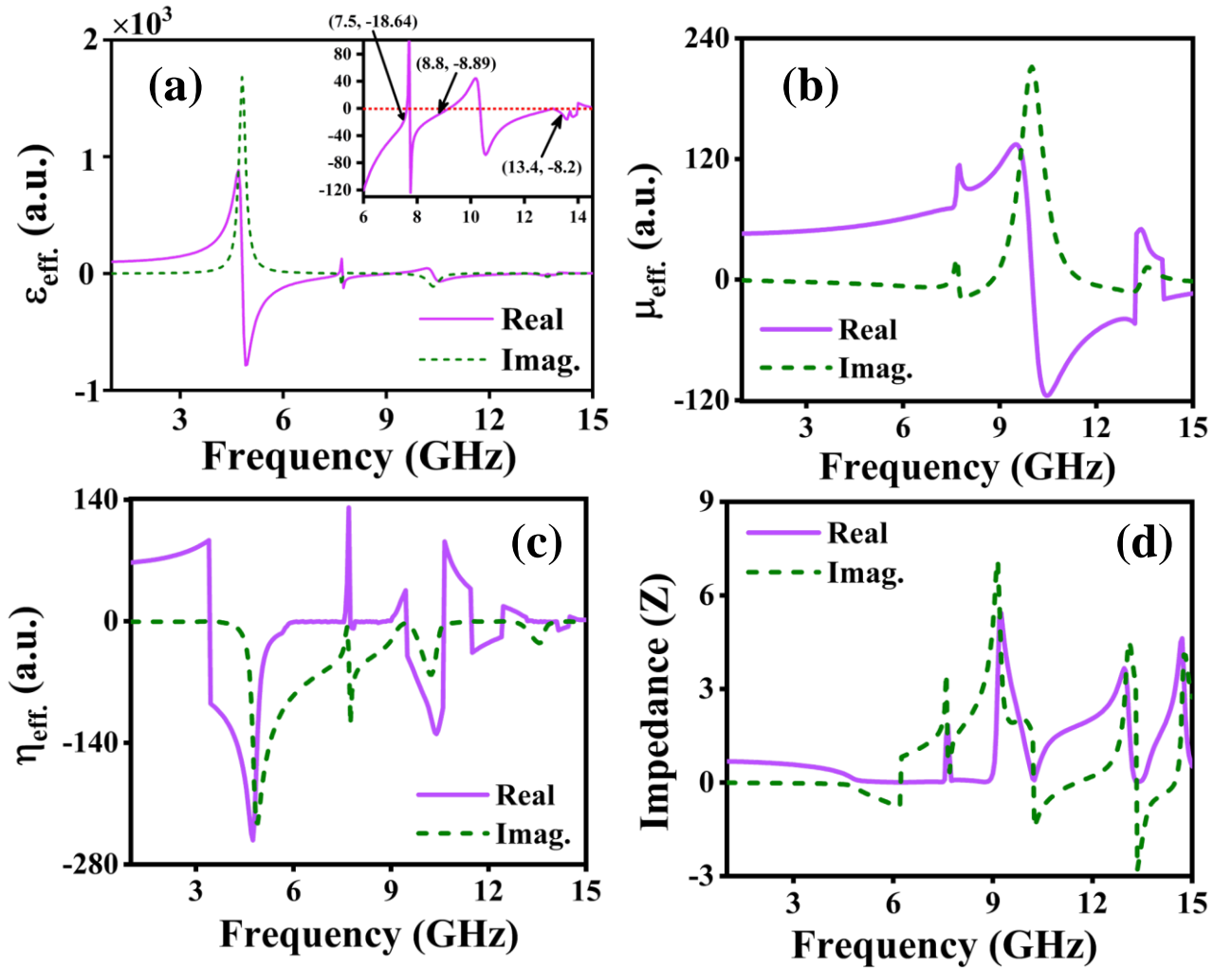
Figure 2.5 Variation of **(a)** effective permittivity ($\varepsilon_{eff.}$), **(b)** effective permeability ($\mu_{eff.}$), **(c)** effective refractive index ($\eta_{eff.}$) and **(d)** impedance (Z) with the frequency of the designed metasurface structure.

Figure 2.5 (a) displays the negative permittivity at three resonance frequencies i.e., 7.5 GHz, 8.8

GHz, and 13.4 GHz, with magnitudes of -18.64 , -8.89, and -8.20, respectively. In Figure 2.5 (b), the

permeability graph shows positive $\mu_{eff.}$ at the resonance frequencies, indicating that the designed

structure behaves as a Single Negative (SNG) metasurface. Figure 2.5 (c) presents the plot of η_{eff}, revealing near-zero characteristics at the resonance frequencies i.e., -0.53 at 7.5 GHz, -0.36 at 8.8 GHz, and -0.46 at 13.4 GHz. These results signify that the proposed design satisfies the properties of Near Zero Index (NZI) along with Epsilon Negative (ENG). Figure 2.5 (d) illustrates the impedance characteristics. The surface current, magnetic field, and electric field distributions for the triple resonance frequency are analyzed and presented in Figure 2.6 - Figure 2.8, respectively. The electric and magnetic field distributions offer insights into the resonance occurrences within the designed metasurface, aiding in identifying frequencies with strong field enhancements or interactions. The confinement of the electric field emerges from the interaction of electromagnetic fields within the designed metasurface.
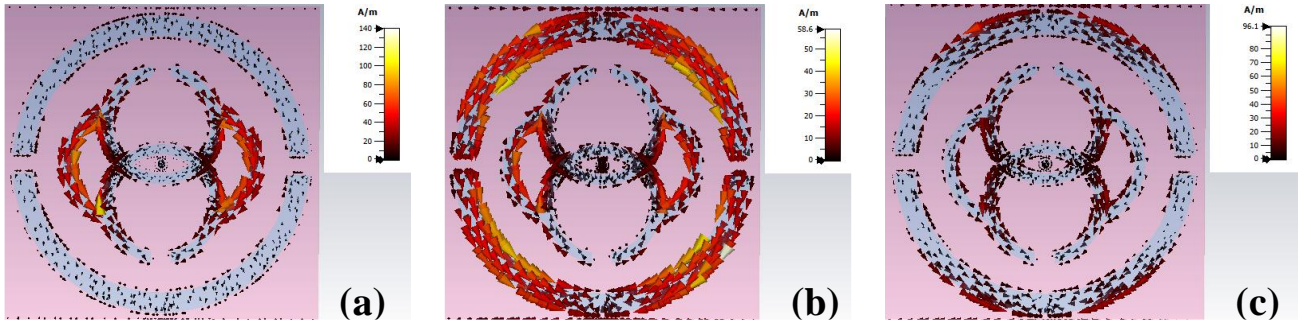
Figure 2.6 Surface current distribution at **(a)** 7.5 GHz, **(b)** 8.8 GHz, and **(c)** 13.4 GHz resonance frequency, respectively.

Figure 2.6 (a) illustrates that at 7.5 GHz, there is a clockwise current flow in the right half and anticlockwise in left half of the circular coupled Split Ring Resonator (SRR) structure. A relatively even current distribution is observed in the inner coupled SRR structure, with higher intensity along the inner circular edges compared to the remaining portion. At 8.8 GHz, as depicted in Figure 2.6 (b), there is a decrease in current due to the distribution in the outer Circular Split Ring Resonator (CSRR) along with the inner coupled SRR. The surface current intensity, indicated by the color bar, increases again at the frequency of 13.4 GHz compared to the 8.8 GHz frequency. In Figure 2.6 (c), the outer region of the CSRR exhibits the maximum current, while the remaining portion has negligible current distribution.

Magnetic field and surface current density are correlated, as shown in equation (1.4). In Figure 2.7 (a), high magnetic field intensities are shown in those regions where a larger current density is observed; this satisfies Maxwell's equation represented by equation (1.4). The H-field distribution of the proposed structure is of the order of 345 A/m in the inner layer of the circular coupled ring for the 7.5 GHz resonance frequency as shown in Figure 2.7 (a).
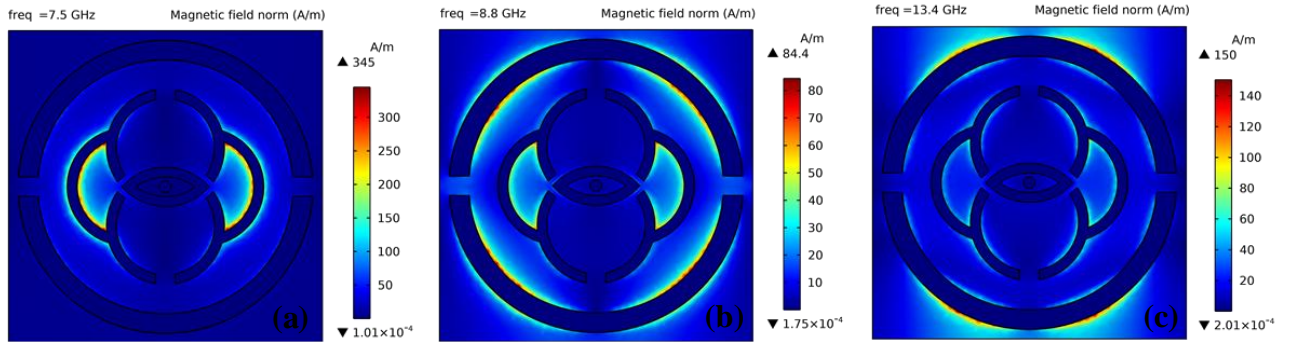
Figure 2.7 Magnetic field distribution at (a) 7.5 GHz, (b) 8.8 GHz, and (c) 13.4 GHz resonance frequency, respectively

Figure 2.7 (b) shows a low-intensity magnetic field owing to the low current intensity at this frequency due to the current getting more distributed in outer CSRR. In contrast, in Figure 2.7 (c), the outer circular edges exhibit significant magnetic field intensity due to knowledgeable current distribution. However, the field intensity is low in other parts of the metasurface structure. The magnetic field distributions at the 8.8 GHz and 13.4 GHz resonance frequencies show lesser accumulation of the field as compared to the magnetic field at 7.5 GHz resonance frequency as shown in Figure 2.7 (b) & (c). The distributions of the electric and magnetic fields are in contradiction to one another, with the magnetic field being the largest where the electric field is minimum and vice versa.

According to equation (1.3), variations in the magnetic field influence the induced electric field. The comparison between Figure 2.8 (a) and Figure 2.7 (a) highlights that areas with maximum changes in the magnetic field exhibit an intense electric field. The capacitive effect leads to a pronounced electric field near the gaps in the metasurface structure. In the proposed metasurface design, the gap regions 'g' and 'c' represent the capacitance of the resonator structure [71].
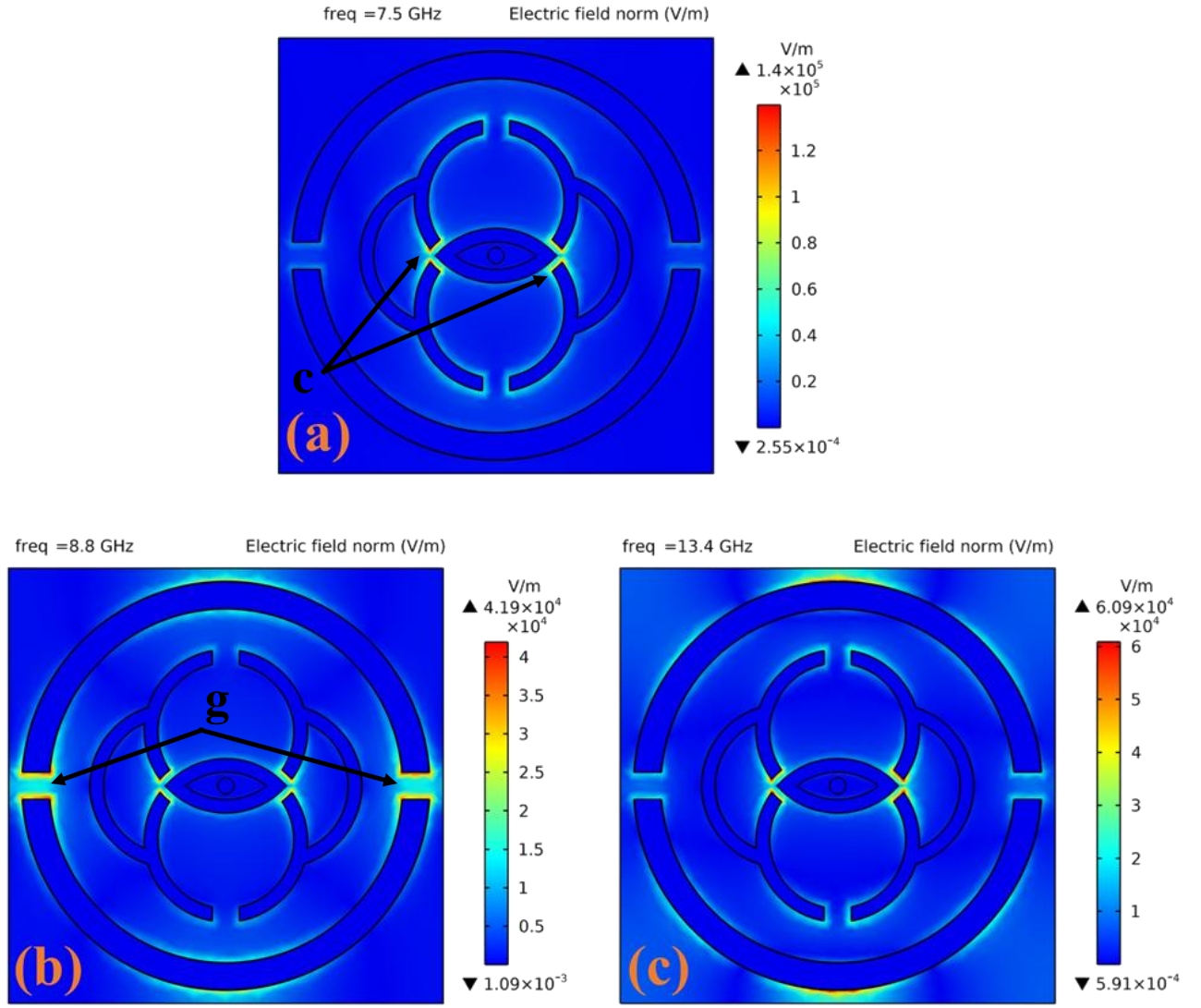
Figure 2.8 Electric field distribution at (a) 7.5 GHz, (b) 8.8 GHz, and (c) 13.4 GHz resonance frequency, respectively

The capacitance is inversely proportional to the gap region of the resonator, and the electric field is more confined in the gap region, signifying the capacitance area in the metasurface. The capacitance can be expressed as $C = \frac{\varepsilon_0 A}{d}$, where ε_0 is the dielectric constant, A is the area between the plates, and d is the distance between the plates. At the resonance frequency of 7.5 GHz, Figure 2.8 (a) depicts a strong electric field near the gap's 'c' of the central coupled circular ring, reaching the order of 1.4×10^5 V/m. As the resonance frequency increases to 8.8 GHz, the electric field accumulates in the gap region of the circle 'c' and the gap 'g' of CSRR, with a reduced order of 4.19×10^4 V/m, as shown in Figure 2.8 (b). Subsequently, at the 13.4 GHz resonance frequency, the magnitude of electric field accumulation is slightly higher than at 8.8 GHz, reaching the order of 6.09×10^4 V/m, as depicted in Figure 2.8 (c). The lower electric field intensity is attributed to low electric current, resulting in less

magnetic field intensity. Additionally, the electric field neutralizes when the magnetic field remains constant in the resonator. The interconnected nature of electromagnetic fields and currents plays a crucial role in the resonances at the specified frequencies.

2.4.1 Equivalent circuit model of the designed metasurface

To validate the outcomes of the designed metasurface, Advanced Design System (ADS) is employed to generate and execute an estimated electrical equivalent circuit model. The components in this model correspond to the capacitance and inductance of individual resonators within the designed metasurface, where metal strips and split gaps are used to construct the unit cell. In the proposed metasurface, these resonators are represented by copper metallic patches. Each metal strip serves as an inductor, and each split gap functions as a capacitor [71]. To ensure effective coupling of electromagnetic waves with the metasurface, impedance-matching components are integrated into the equivalent circuit model, optimizing reflection and transmission properties.

The equivalent circuit model predicts the resonance frequencies in the proposed structure by connecting inductors and capacitors, forming an LC circuit similar to an LCR tank circuit. These components can be arranged in series or parallel configurations to create the circuit. The resonance frequency of an LCR circuit occurs when inductive and capacitive reactance are equal, resulting in a cancellation of these reactive components and leaving only the resistance in the circuit. At resonance, the impedance becomes purely resistive, and the circuit responds most strongly to the applied frequency. Thus, an LC resonance circuit is utilized to represent the entire unit cell, with inductance (L) and capacitance (C) serving as fundamental variables to calculate the resonance frequency (f).

The impedance (Z) of an LCR circuit is a complex quantity, considering resistance (R), inductive reactance (X_L), and capacitive reactance (X_C), and is given by $Z = R + j(X_L - X_C)$, where j is the imaginary unit. At resonance, $X_L = X_C$, leading to the cancellation of reactive components, rendering Z purely resistive. The frequency at which impedance is minimized (equal to resistance) defines the resonance frequency, calculated by the formula [72]:

$$f = \frac{1}{2\pi\sqrt{LC}}$$
<div align="right">2.1</div>
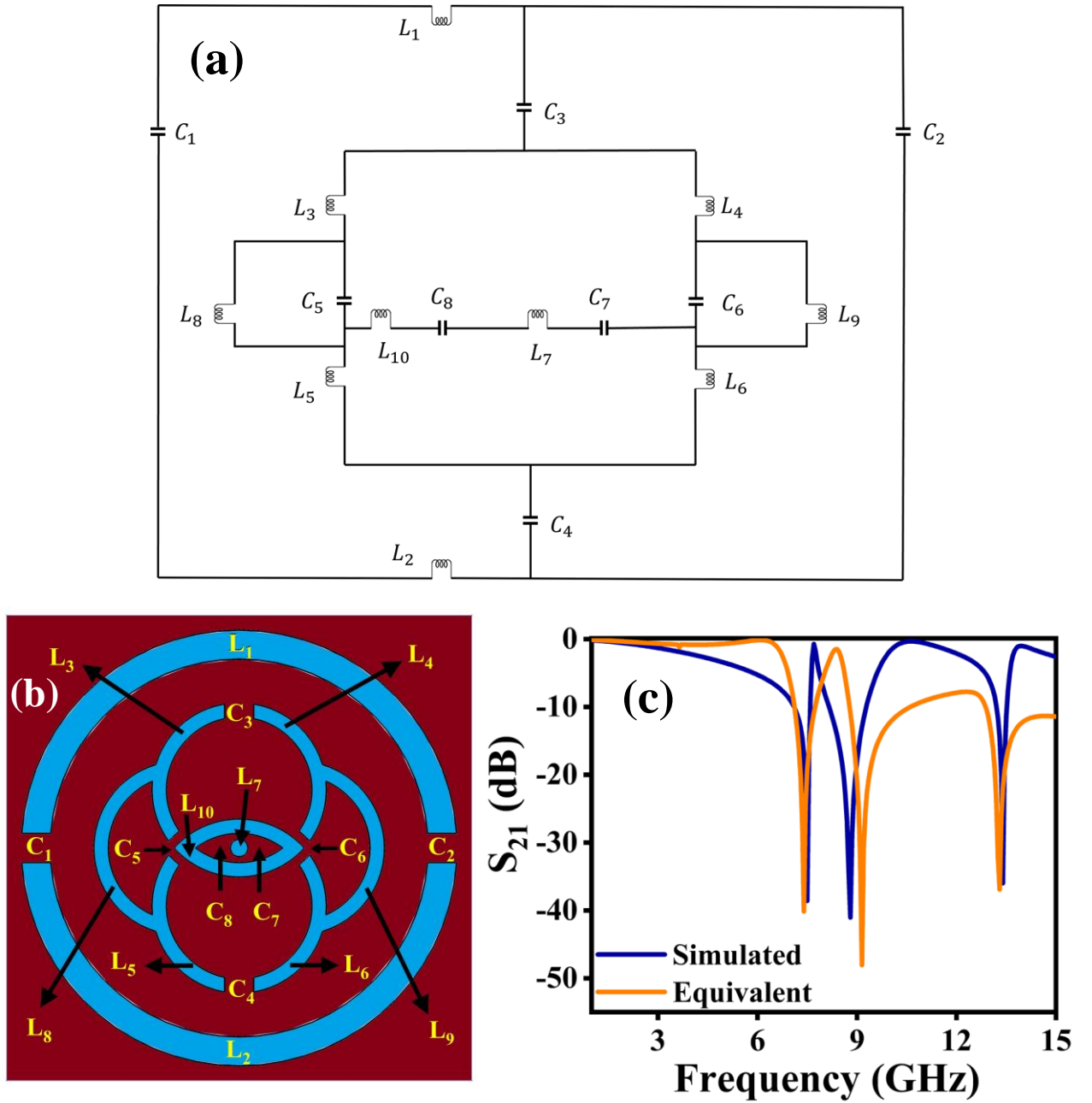
Figure 2.9 (a) Equivalent circuit model with lumped elements, **(b)** inductance (L) and capacitance (C) representation of the equivalent circuit model, and **(c)** corresponding results of S_{21} (transmission coefficient) from the simulated structure and the equivalent structure of the proposed metasurface.

Figure 2.9 (a) shows the proposed metasurface resonator equivalent LC circuit model and Figure 2.9 (c) represents the obtained results from the simulated structure and the equivalent circuit model of the proposed metasurface. The L_1C_1 and L_2C_2 correspond to the outer ring of the circular-shaped split ring resonator LC combination. The C_3 and C_4 correspond to the upper and lower split gap 'g',

L_8 and L_9 represent the coupled circular arc inductors, L_3 C_5 L_5 and L_4 C_6 L_6 represent the centered cross circle and L_{10} C_8 L_7 C_7 corresponds to the centered eye shaped, and circle shaped respectively as shown in Figure 2.9 (b). It is evident from Figure 2.9 (c) that the result for the equivalent LC circuit modeling of the proposed metasurface unit cell structure resonates in the triple band which matches the simulated result. The corresponding values of all lumped elements are listed in Table 2.2.

Table 2.2 Corresponding values of all lumped components of the equivalent circuit for the proposed metasurface design.

Lumped components	Value (nH)	Lumped components	Value (pF)
L_1	1.04	C_1	0.85
L_2	0.534	C_2	0.265
L_3	0.98	C_3	0.406
L_4	0.8	C_4	1.38
L_5	1.19	C_5	0.59
L_6	1.5	C_6	2.525
L_7	0.86	C_7	0.9
L_8	1.136	C_8	1.5
L_9	0.156		
L_{10}	0.3		

2.5   SUMMARY

In summary, this study focused on the fabrication and simulation of an eye-shaped CC-SRR metasurface structure on an FR-4 dielectric substrate, showcasing ENG and NZI characteristics across the frequency range of 1-15 GHz. The experimental measurements were compared with simulated results, revealing a close match and minimal frequency shift, indicating acceptable agreement. The structure exhibited tunable features with variations in dielectric substrate thickness (t_s) and copper resonator thickness (t_m). Validation of simulated results was conducted using different simulation software and an equivalent electrical circuit model. Examination of electric and magnetic field distributions provided insights into electromagnetic characteristics at various resonant frequencies. Overall, these findings suggest that the designed metasurface structure holds promise for applications in microwave components and devices, particularly in C, X, and Ku-bands.

CHAPTER- 3

Ankit, K. Kishor, R.K. Sinha,
Design and analysis of wavelength tunable metamaterial reflector,
Results Opt. 10 (2023) 100366.

CHAPTER 3: WAVELENGTH TUNABLE METAMATERIAL REFLECTOR

3.1 INTRODUCTION

In the preceding chapter, the epsilon-negative (ENG) and near-zero index (NZI) metasurfaces has designed, engineered to induce resonance frequencies across the C, X, and Ku bands within the microwave spectrum. This chapter focuses on the creation and performance attributes of a tunable metamaterial (MTM) designed as a perfect reflector, achieving nearly 100% reflection at a resonance wavelength (λ_r) of 1550 nm.

Over the past decades, metamaterials have exhibited intriguing electromagnetic properties across a wide frequency range, spanning from GHz [73] and THz [74] to the infrared and visible regions. Early research centred on utilizing electric-dipole resonance in metallic wires and magnetic-dipole resonance in SRRs to attain negative permittivity and negative permeability, respectively [10], particularly in the GHz and THz ranges. However, the challenge lies in applying these concepts to structures with submicron or nanoscale dimensions in the infrared and optical frequencies due to the inherent losses in resonant metallic structures [75]. An alternative approach, involving dielectric particles, has proven effective in achieving electric or magnetic resonances with reduced loss, offering potential applications in photonic devices such as perfect reflectors [76,77]. While Bragg reflectors can also achieve high reflectivity, their drawback lies in the requirement of numerous layers for sufficient reflectivity, resulting in a time-consuming and costly deposition process involving various dielectric materials [78]. MTMs present an advantageous alternative to metallic mirrors as they are suitable for large-area applications without the need for periodicity in truly homogeneous media [79].

This chapter introduces an MTM unit cell designed to achieve nearly 100% reflection at an operating wavelength of 1550 nm within the C-band of the optical communication window. The tunability of

the operating wavelength demonstrated by adjusting the number of arrays and employing a mirror image arrangement, leading to a significant shift in resonance wavelength from the C-band to the S-band of optical communication. The proposed MTM structure displays characteristics of μ-negative (MNG) materials and a negative effective refractive index at λ_r. The calculated effective medium ratio (EMR) attains a value of 2.23, highlighting its importance in the design and development of compact tunable photonic devices, including perfect reflectors, antennas, and filters.

3.2   METAMATERIAL DESIGN AND SIMULATION GEOMETRY
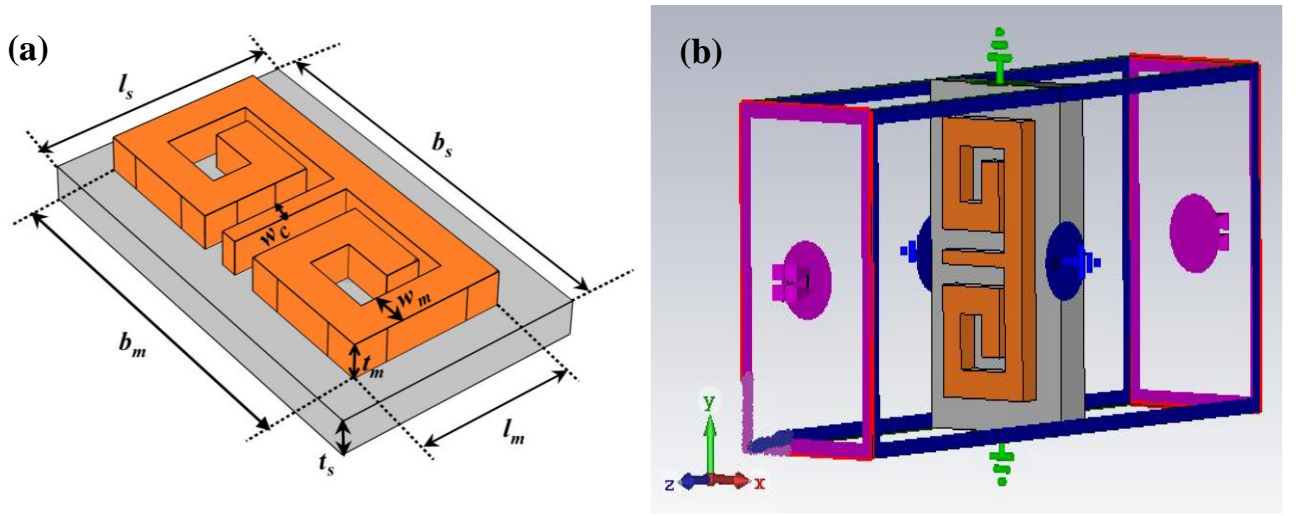
Figure 3.1 (a) Designed MTM structure and **(b)** setup arrangement for scattering parameters.

The designed MTM unit cell comprises a silicon layer with a thickness of 90 nm and a permittivity (ε) of 11.7 [80], situated on a silica substrate measuring 1180 nm × 690 nm, with a refractive index (n_s) of 1.45 [81]. Figure 3.1 illustrates the schematic representation of the MTM unit cell, with (a) displaying a perspective view and (b) depicting the configuration including input and output ports for measuring the scattering parameters of the MTM.

The x-axis and y-axis are characterized by PMC and PEC boundary conditions, respectively. In the MTM unit cell, an electromagnetic wave is incident perpendicularly along the z-axis, with a linearly polarized electric field in the y-axis direction. Two waveguide ports positioned in the specified positive and negative z-directions to assess the MTM behavior within the operational wavelength range of 1400 nm to 1700 nm.

3.3 OPTIMIZATION OF MTM UNIT CELL

3.3.1 Design Methodology

The design methodology for the proposed MTM structure is illustrated in Figure 3.2, comprising five sequential design steps.
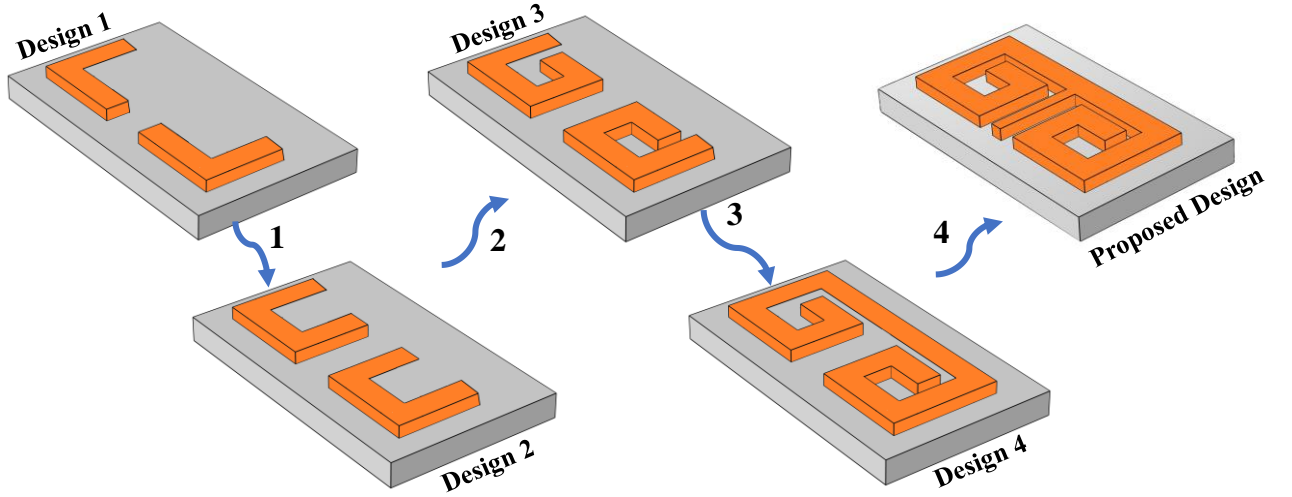
Figure 3.2 MTM unit cell design methodology.
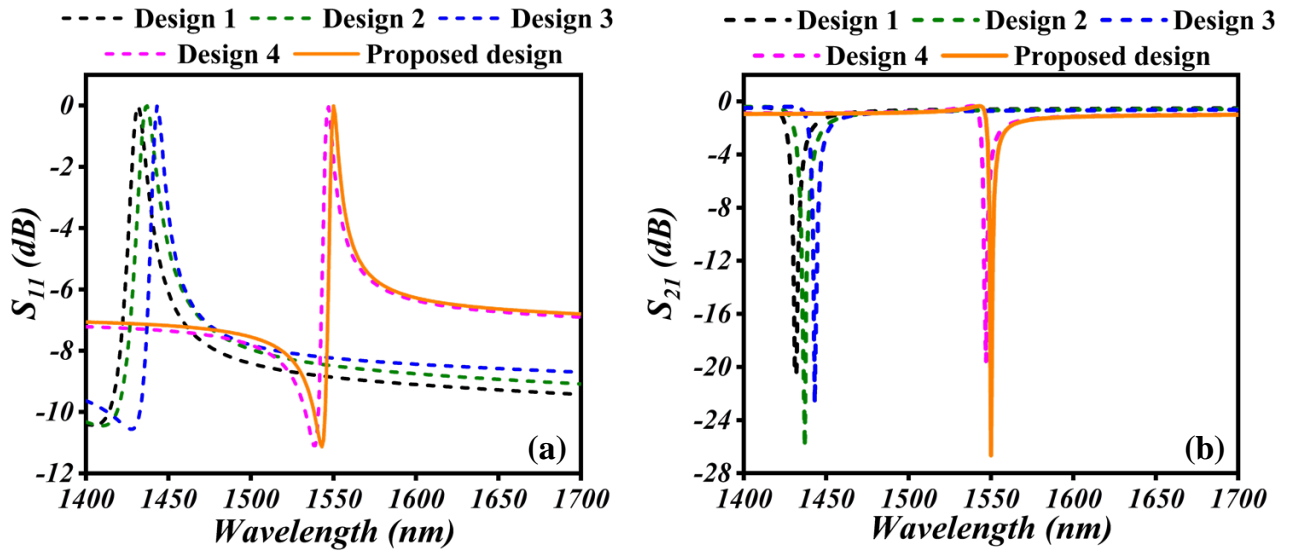
Figure 3.3 **(a)** The Reflection (S_{11}) and **(b)** Transmission coefficient (S_{21}) for the different designs step (design 1 to proposed design) with respect to wavelength from 1400 nm to 1700 nm.

Design 1 created by combining two L-shaped mirror strips on the substrate, inducing resonance when electromagnetic waves propagate along the z-axis. This configuration achieves an almost 100% reflection coefficient at a resonance wavelength of 1432 nm, as depicted in Figure 3.3 (a). Design 2

enhances Design 1 by adding two additional horizontal strips, resulting in a resonance wavelength of 1437 nm. Design 3 extends this by incorporating two more vertical strips at the ends of Design 2, achieving a resonance wavelength of 1443 nm.

In Design 4, a vertical strip connects the two mirror shapes, leading to a resonance wavelength of 1547 nm. Finally, Design 5 is obtained by adding a horizontal strip between the two similar shapes, aiming to achieve nearly 100% reflection coefficient at the resonance wavelength λ_r, as shown in Figure 3.3 (a).

3.3.2 Parametric investigation on proposed MTM unit cell

In this section, an in-depth computational analysis has been conducted to investigate the influence of diverse factors, such as substrate material, resonator geometrical parameters, and substrate characteristics, on the resonance wavelength.

3.3.2.1   Effect of different substrate materials
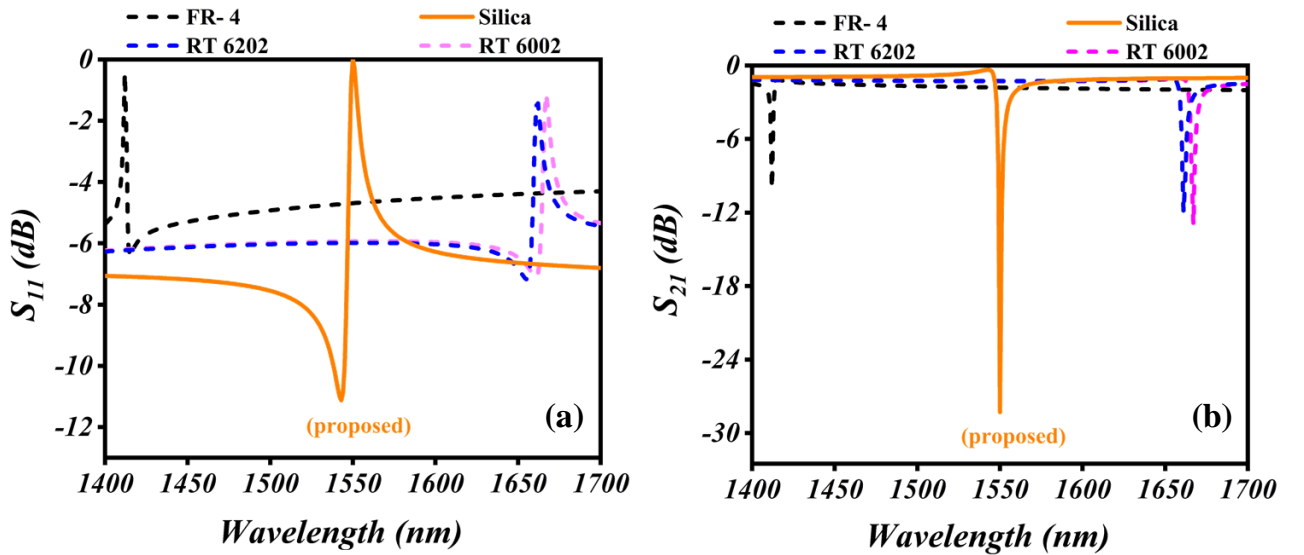
Figure 3.4 Variation of (a) reflection coefficient and (b) transmission coefficient (S_{21}) with the incident wave with the change in the different dielectric substrates.

Various dielectric materials, including FR-4, Roger's versions (RT 6002 and RT 6202), and Silica, have been evaluated as potential substrates. As depicted in Figure 3.4, the resonance wavelengths for MTM were observed at 1412 nm, 1661 nm, 1667 nm, and 1550 nm when utilizing FR-4, RT 6202,

RT 6002, and Silica as substrate materials, respectively. The summary of these findings presented in Table 3.1.

Table 3.1 Various properties and S_{21} parameters result from different substrate materials.

Sr. No.	Substrate	Relative permittivity	Resonance wavelength of S_{21} (nm)	Optical wavelength	Magnitude (dB)
1.	FR-4	4.5	1412	E (Extended band)	-10
2.	**Silica (proposed)**	**3.75**	**1550**	**C (Conventional band)**	**-28.2**
3.	Roger's RT 6202	2.9	1661	U (Ultra long wavelength)	-11.9
4.	Roger's RT 6002	2.94	1667	U (Ultra long wavelength)	-12.9

Notably, a shift towards lower wavelengths occurred when employing FR-4 and Silica substrates compared to Roger's versions, suggesting that MTM performance is influenced by substrate selection, as illustrated in Figure 3.4. The substantial impact of the silica substrate on the resonance wavelength, along with its nearly 100% reflection, led to the decision to adopt Silica as the substrate material for the proposed MTM unit cell.

3.3.2.2 Effect of silica substrate thickness (t_s)
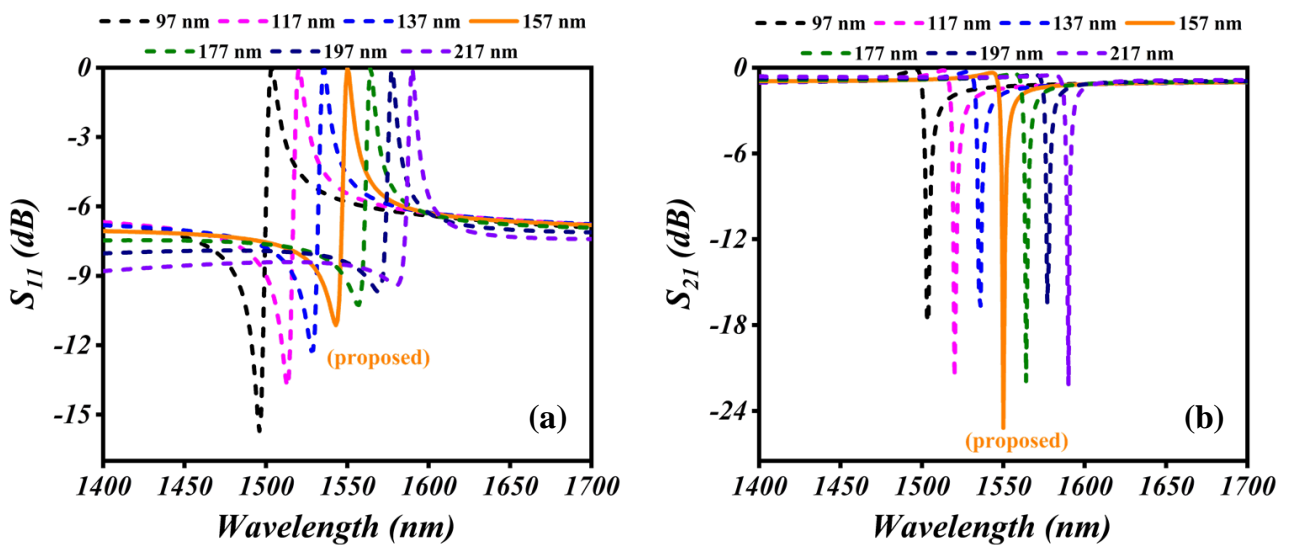
Figure 3.5 Variation of different substrate thicknesses (t_s) of the designed MTM with the incident wave resulting in its impact on **(a)** reflection coefficient (S_{11}) and **(b)** transmission coefficient (S_{21}).

The substrate functions as a dielectric medium, introducing capacitance between the two waveguide ports. As the thickness of the substrate (t_s) is increased, the parallel capacitance also increases, leading to a higher resonance wavelength [69]. In our analysis, we examined the impact of varying the thickness of the silica substrate from 97 nm to 217 nm, and the results are depicted in Figure 3.5. Within the proposed MTM unit cell, both S_{11} and S_{21} parameters exhibited a shift towards higher wavelengths as t_s increased. Figure 3.5 highlights that the desired resonance wavelength in the C-band at λ_r is achieved when the substrate thickness is 157 nm.

3.3.2.3 Effect of resonator material (silicon) thickness (t_m)
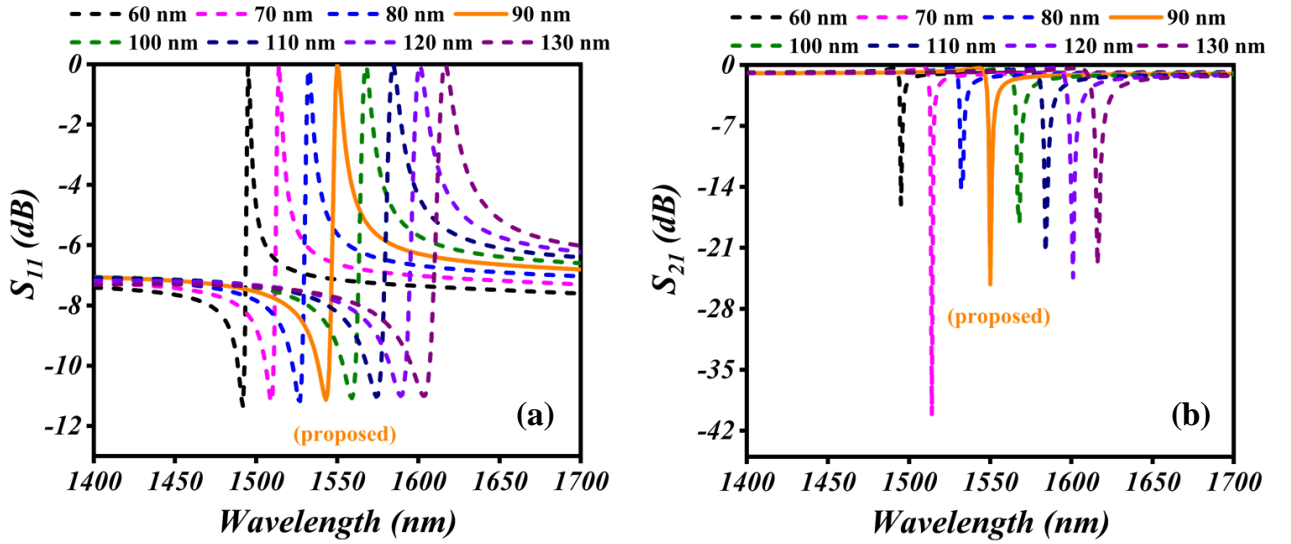
Figure 3.6 Variation of silicon dielectric resonator thickness (t_m) of the designed MTM with the incident wave resulting in its impact on **(a)** reflection coefficient (S_{11}) and **(b)** transmission coefficient (S_{21}).

Table 3.2 Unit Cell Dimension

Parameters	Values (nm)	Description
b_s	1180	breadth of substrate in y
l_s	692	length of substrate in x
l_m	425	material length in x
b_m	949	material length in y
t_s	157	substrate thickness
w_c	47	width of central line
t_m	90	thickness of material
w_m	94	width of MTM strip

The thickness of the resonator material has been varied within the range of 60 nm to 130 nm, and the resulting changes in resonance wavelength were examined. The plotted data in Figure 3.6 illustrates a noticeable redshift, indicating that the resonance wavelength shifts towards the higher wavelength side with an increase in thickness. As per the findings in Figure 3.6, it is noted that the proposed MTM unit cell, featuring a silicon resonator, achieves the desired resonance wavelength in the C-band at λ_r when the thickness is set at 90 nm. The optimized geometrical parameters for the MTM unit cell are detailed in Table 3.2.

3.4   RESULTS AND DISCUSSION
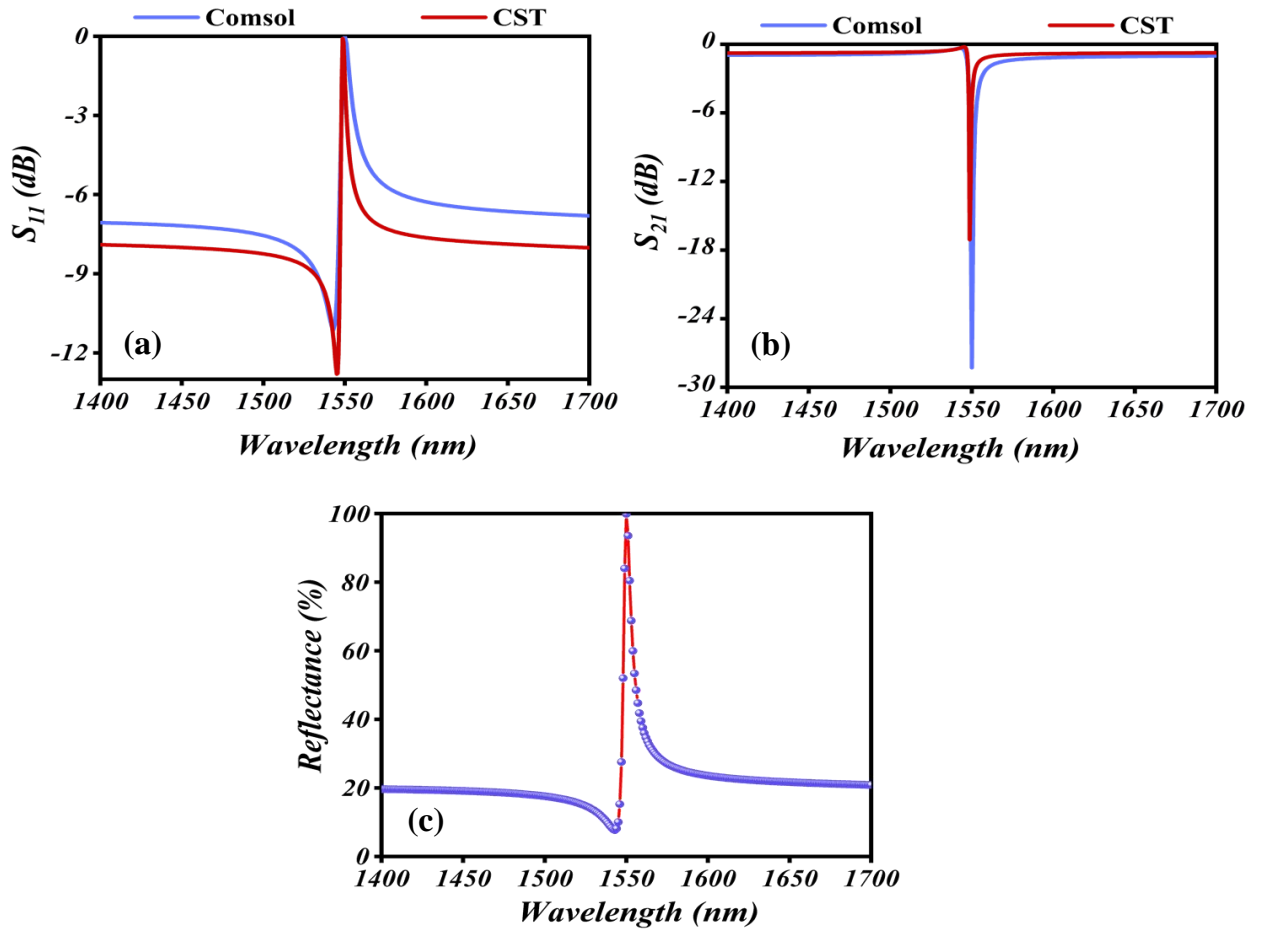
Figure 3.7 (a) Reflection (S_{11}) and **(b)** Transmission (S_{21}) coefficient have been calculated from both COMSOL and CST software **(c)** calculated reflectance spectra of the proposed metamaterial from COMSOL.

This section involves the calculation and analysis of the effective electromagnetic parameters of the designed MTM. Additionally, the tunability characteristics of the MTM are explored and discussed through an array analysis and mirror image approach.

3.4.1 Scattering parameters of optimized MTM unit cell

The Drude-Lorentz variables were utilized for assessing the scattering parameters through simulations conducted with FEM-based COMSOL Multiphysics and CST Microwave Studio. As depicted in Figure 3.7 (a)-(b), the analysis of S_{11} and S_{21} from the two simulation platforms exhibited notable similarity. In Figure 3.7 (c), the reflectance spectra of the proposed structure are presented, revealing nearly 100% reflectance at the resonance wavelength (λ_r) due to magnetic dipole resonance. The achievement of perfect reflectance is contingent on the characteristics of permeability (μ) and permittivity (ε). Specifically, when $\mu > 0$ and $\varepsilon < 0$, it corresponds to electric dipole resonance, while $\mu < 0$ and $\varepsilon > 0$ correspond to magnetic dipole resonance [78,82]. Table 3.3 provides a comprehensive comparison of the % reflectance of the proposed MTM structure with findings from prior literature [78,82–84].
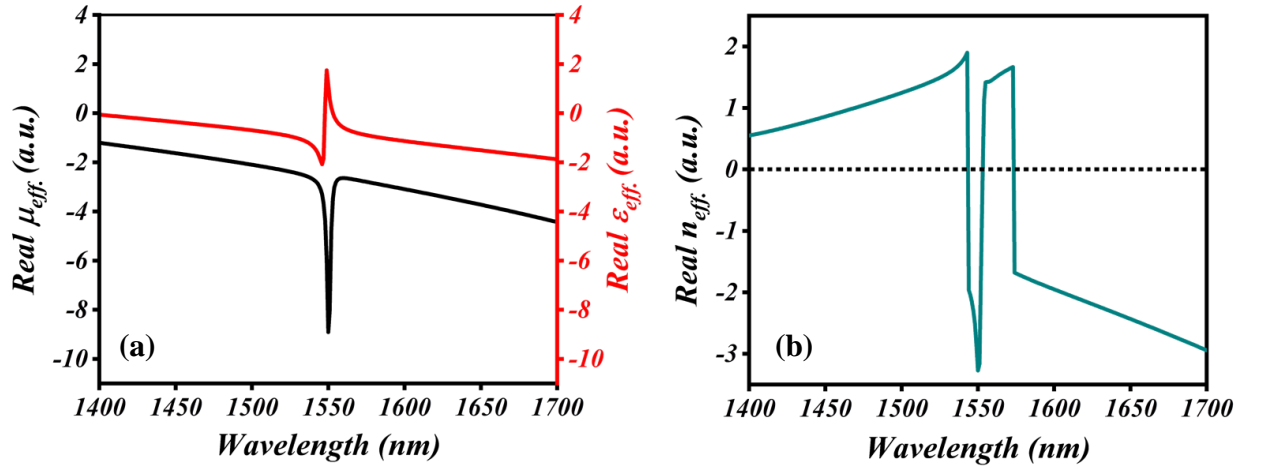
Figure 3.8 **(a)** The real parts of $\mathbf{\mu_{eff.}}$ (effective permeability) and $\mathbf{\varepsilon_{eff.}}$ (effective permittivity), **(b)** $\mathbf{n_{eff.}}$ (effective refractive index) curves of the proposed MTM structure.

3.4.2 Effective Electromagnetic Parameters

Using the equations. (1.10-1.12) in section 1.5 of CHAPTER 1: , the effective permittivity ($\varepsilon_{eff.}$), effective permeability ($\mu_{eff.}$) and effective refractive index ($n_{eff.}$) is calculated with respect to the operating wavelength and plotted in Figure 3.8.

In Figure 3.8 (a), it is evident that at the resonance wavelength (λ_r) of 1550 nm, $\varepsilon_{eff.}$ assumes a positive value, while $\mu_{eff.}$ takes on a negative value. Moreover, $\mu_{eff.}$ consistently exhibits negativity

beyond 1560 nm, confirming the entirely negative behavior of effective permeability in the 1400-1700 nm range, indicating the metamaterial's characteristic of having a negative refractive index (MNG). The attainment of negative permeability at the resonance wavelength could be advantageous in long-distance communication. Additionally, Figure 3.8 (b) illustrates that $n_{eff.}$ has a negative value at λ_r.

Table 3.3 Comparison of % reflectance of the proposed designed MTM structure with previously reported data

Ref.	Period (nm)	Shape	Resonance wavelength	Reflectance (%)
[78]	820×820	Silicon cubes	1500 nm	99.9
[83]	660×660	Silicon cylinder	1450 nm	99.9
[82]	820×820	Silicon cylinder	1530 nm	99.7
[84]	720×720	• Si disk array • Diamond disc array	• 1050-1110 nm • 1040-1100 nm	> 97
Our work	**692×1180**	**Silicon structure**	**1550 nm**	**99.8**

Furthermore, EMR plays a pivotal role in the design and advancement of metamaterials as it aids in compacting the structure and is calculated using the formula [85]:

$$EMR = \frac{\text{Operating Wavelength for the unit cell}}{\text{length of the unit cell}} \qquad 3.1$$

The EMT is applied to assess the designed metamaterial structure. According to EMT, the dimensions of the unit cell should be smaller than the operating wavelength [86]. The reported MTM unit cell achieves an EMR of 2.23 at the operating resonance wavelength of 1550 nm. This relatively high EMR value ensures the compactness of devices constructed using the proposed MTM.

3.4.3 Analysis of Normalized Electric and Magnetic field Distribution

The MTM unit cell is exposed to a perpendicular electromagnetic wave along the z-axis, featuring a linearly polarized electric field oriented along the y-axis. The split gap within the proposed MTM induces capacitance, leading to electric resonance, while the resonator strip introduces inductance,

resulting in magnetic resonance [87]. The distribution of electric and magnetic fields within the MTM structure has been assessed at the resonance wavelength (λ_r) and is depicted in Figure 3.9 (a) and (b).
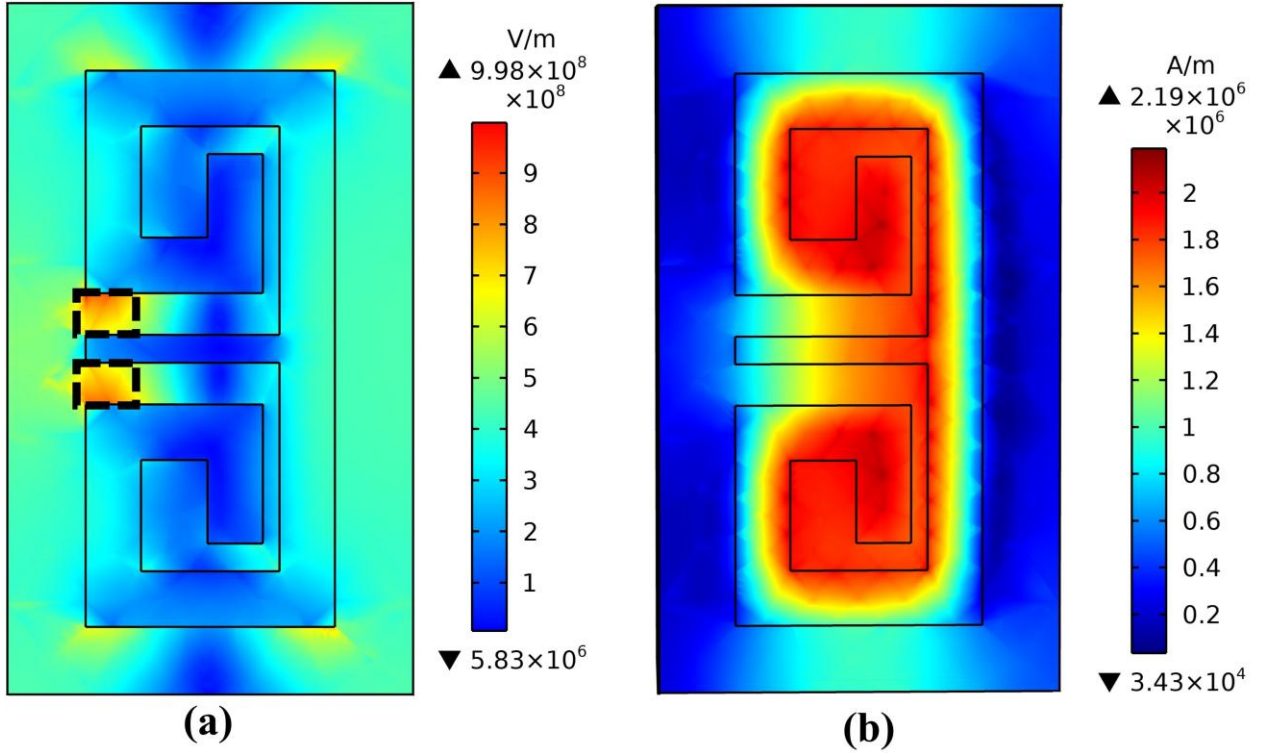
Figure 3.9 A plot of normalized **(a)** Electric Field and **(b)** Magnetic Field Distribution of the MTM structure at λ_r

Figure 3.9 (a) reveals that the highest concentration of electric field distribution reaches approximately 10^8 V/m. Specifically, this concentration occurs along the gap between the edge of the central line (w_c) and the edge of the MTM resonator strip, as indicated by the yellowish region enclosed by a black dotted rectangle. In Figure 3.9 (b), the maximum accumulation of magnetic field distribution is observed at the center of the structure, with an order of magnitude around 10^6 A/m.

3.4.4 Tunability characteristic of MTM unit cell

The investigation delves into the arrangement of multiple MTM unit cells in a regular pattern to analyze the tuning characteristics of the proposed MTM structure. This exploration is crucial for designing and developing tunable MTMs suitable for diverse applications.

The study encompasses (1×1), (1×2), (1×3), (1×4), as well as (2×1), (3×1), and (4×1) array structures of MTM unit cells, as illustrated in Figure 3.10. Each unit structure within every assembly maintains

consistent physical dimensions, as detailed in Table 3.2. The boundary conditions, wavelength range, and direction of an incident plane wave on an MTM unit cell remain the same as previously mentioned to investigate the impact of different array structures.
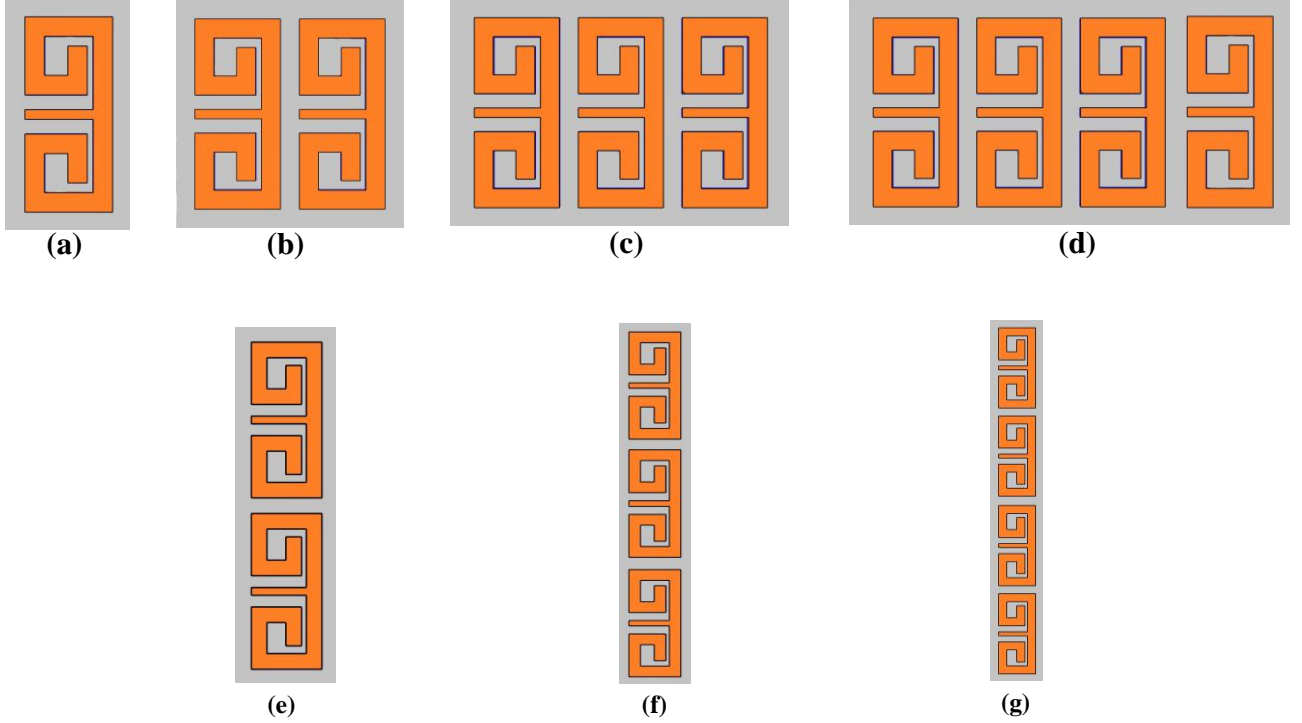
Figure 3.10 Top view of the arrays of the metamaterial **(a)** (1×1), **(b)** (1×2), **(c)** (1×3), **(d)** (1×4), **(e)** (2×1), **(f)** (3×1) and **(g)** (4×1) of the proposed structure.

Initially, the variations in scattering parameters, effective permeability, effective permittivity, and effective refractive index with the wavelength of an incident wave for (1×1), (1×2), (1×3), and (1×4) MTM array structures have been computed and presented in Figure 3.11. In Figure 3.11, the formation of arrays like (1×1), (1×2), (1×3), and (1×4) results in the parallel arrangement of the inductors of individual unit cells. Consequently, the equivalent inductance decreases, leading to a blue shift in the resonance wavelength, as indicated by equation:

$$\lambda = \frac{c}{f} = c\sqrt{LC}$$

3.2

Additionally, Figure 3.12 illustrates the changes in scattering parameters, effective permeability, effective permittivity, and effective refractive index in relation to the wavelength of an incident wave for (2×1), (3×1), and (4×1) MTM array structures. In this figure, it is observed that when forming arrays such as (1×1), (2×1), (3×1), and (4×1), the inductor of one unit cell is in series with the other.

As a result, the equivalent inductance increases, leading to a redshift in the resonance wavelength (according to eq. (3.2)).
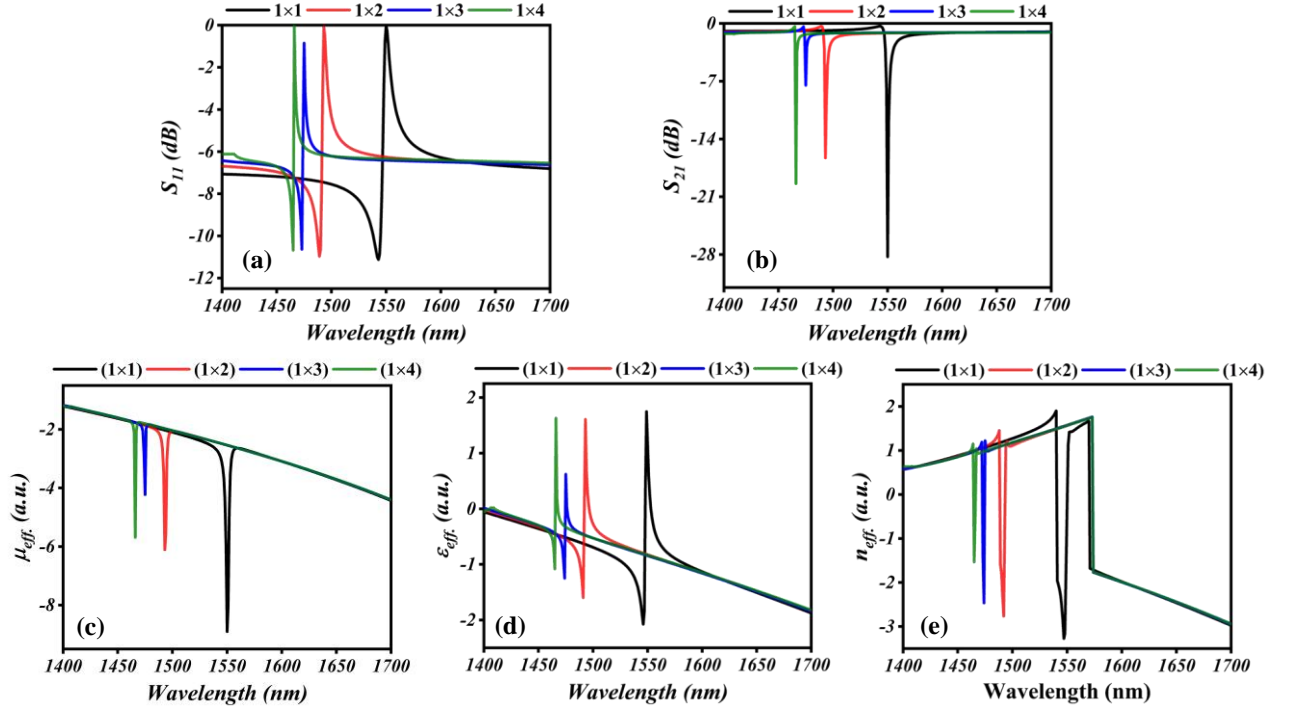
Figure 3.11 Variation of **(a)** S_{11} (reflection coefficient), **(b)** S_{21} (transmission coefficient), **(c)** $\mu_{eff.}$ (effective permeability), **(d)** $\varepsilon_{eff.}$ (effective permittivity) and **(e)** $n_{eff.}$ (effective refractive index) with wavelength for the proposed structure's (1×1), (1×2), (1×3) and (1×4) arrays.
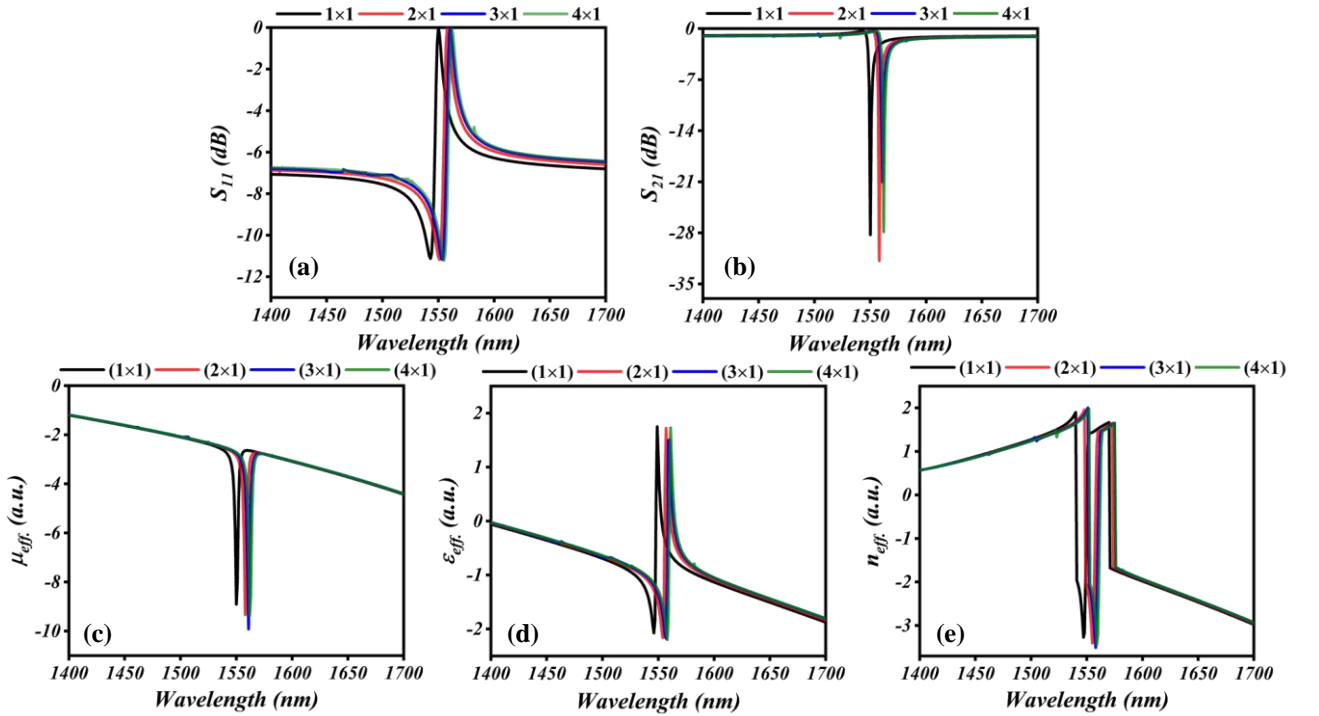
Figure 3.12 Variation of **(a)** S_{11} (reflection coefficient), **(b)** S_{21} (transmission coefficient), **(c)** $\mu_{eff.}$ (effective permeability), **(d)** $\varepsilon_{eff.}$ (effective permittivity) and **(e)** $n_{eff.}$ (effective refractive index) with wavelength for the proposed structure's (1×1), (2×1), (3×1) and (4×1) arrays.
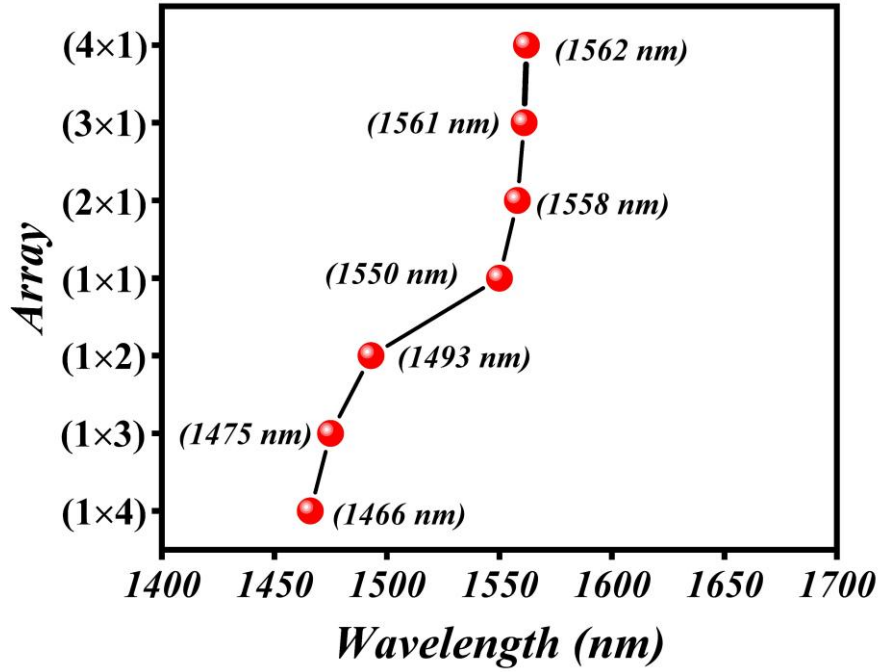
Figure 3.13 Variation of resonance wavelength with the array of the MTM structure.

Furthermore, it is noted that when moving column-wise in the array structure (i.e., (2×1), (3×1), and (4×1)) while keeping one row fixed, the shift in resonance wavelength is minimal. This suggests that structuring the array in this manner has a lesser impact on the resonance wavelength. Figure 3.13 depicts the variation of resonance wavelength with the array of the MTM unit cell. The graph indicates that the change in resonance wavelength is substantial with an increase in columns (i.e., (1×1), (1×2), (1×3), and (1×4)), decreasing from 1550 nm to 1466 nm. However, the variation is insignificant with changes in rows ((2×1), (3×1), and (4×1)) in the MTM structure array.

3.4.5 Mirror Image of the proposed MTM unit cell structure

Moreover, an analysis to assess the impact on resonance wavelength by incorporating the mirror image of the design into the MTM unit cell has been conducted, as depicted in the inset of Figure 3.14 (a). The reflection and transmission characteristics, along with variations in electromagnetic parameters (μ_{eff}, ε_{eff}, n_{eff}), were computed and illustrated in Figure 3.14. The results indicate that incorporating the mirror image of the structure in the MTM unit cell yields similar behavior, albeit with a shift in resonance wavelength from 1550 nm (C-band) to 1504 nm (S-band). This finding suggests that our work presents a potentially more straightforward approach to tuning the resonance

wavelength for specific applications. Consequently, this investigation contributes valuable insights for the design and development of tunable MTM.
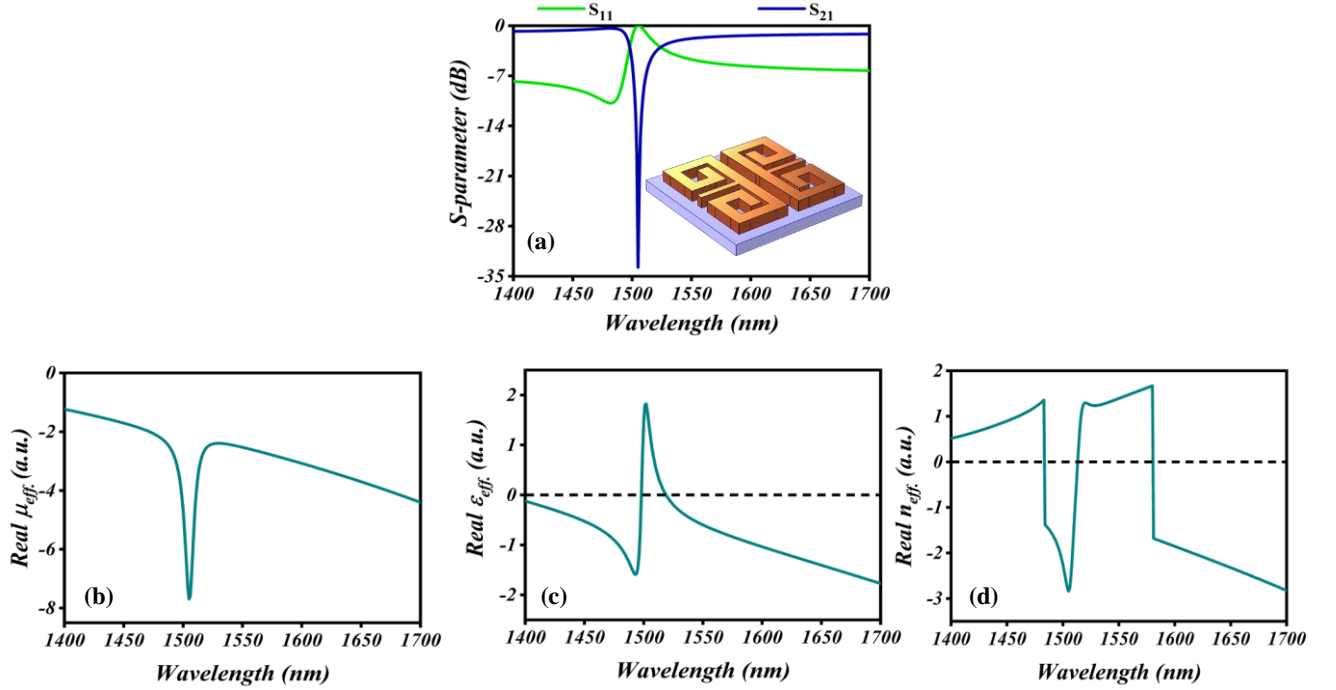
Figure 3.14 Variation of **(a)** scattering parameter i.e., S_{11} (reflection coefficient) and S_{21} (transmission coefficient), and inset shows the designed mirror image of the metamaterial unit cell **(b)** $\mu_{eff.}$ (effective permeability), **(c)** $\varepsilon_{eff.}$ (effective permittivity) and **(d)** $n_{eff.}$ (effective refractive index) of the mirror image of MTM structure with wavelength

3.5 SUMMARY

In summary, a highly efficient tunable metamaterial (MTM) structure with nearly 100% reflectance has been designed and analyzed for optical communication, targeting a resonance wavelength of 1550 nm. The optimization process involved a systematic approach and parametric investigation focusing on the MTM unit cell. Various factors, including different substrate materials, silica substrate thickness (t_s), and silicon resonator thickness (t_m), were considered in the design process to achieve the desired resonance wavelength (λ_r=1550 nm).

The effective propagation characteristics of the proposed MTM were explored across the 1400-1700 nm wavelength range, leading to the determination of effective medium parameters. The analysis revealed that the proposed MTM exhibits an effective negative refractive index and metamaterial with MNG characteristics at the resonance wavelength (λ_r). The electric and magnetic field

distributions at the resonance wavelength were visualized through normalized plots. Additionally, the designed MTM structure arrays, such as (1×2), (1×3), (1×4), and (2×1), (3×1), (4×1), were found to confirm the tunability of the proposed MTM. Furthermore, the mirror image of the proposed MTM structure exhibited resonance at a wavelength of 1505 nm, falling within the S-band commonly used in Passive Optical Network systems. The combination of perfect reflectance and tunable performance positions the reported MTM unit cell as a promising candidate for devices and components employed in long-distance transmission systems.

CHAPTER- 4

CHAPTER 4: METASURFACE FOR BROADBAND PERFECT REFLECTION IN VISIBLE SPECTRUM

4.1 INTRODUCTION

In the last chapter, perfect tunable MTM structure has been designed for the infrared optical communication window. In this chapter, a different approach of Silicon on Insulator metasurface has been utilized to obtain broadband perfect reflection in visible spectrum.

Metasurface offer a wide array of applications owing to their capacity to demonstrate properties like negative permeability and permittivity [88], alongside intriguing features such as perfect lenses [89] and antennas [90]. Frequently, metallic resonators such as Metallic split-ring resonators (MSRR) [9] and metallic cut-wire arrays [91] are utilized extensively in metamaterial design. Split-ring resonators (SRR) generate magnetic dipole (MD) resonances, while cut-wire arrays produce electric dipole (ED) resonances. These structures have shown efficacy in manipulating electromagnetic waves across various wavelengths from gigahertz to terahertz and even n-IR. However, the significant absorption loss in metal-based metamaterials presents a challenge for their application in photonics where minimizing energy dissipation is vital for efficient light manipulation and transmission. To address this issue, alternative materials or strategies need exploration. One such approach involves investigating alternative materials with lower losses within the desired spectral range. For instance, dielectric materials can replace metals to mitigate energy dissipation [92]. Dielectric resonators can maintain resonant behavior, contributing to metamaterial functionality while exhibiting lower losses compared to their metallic counterparts [93].

Recent progress in metasurface research indicates that low-loss dielectric nanoparticle-based metasurfaces can offer viable alternatives to metallic metasurfaces for generating electric or magnetic resonances in the visible or near-infrared spectrum [93,94]. Specifically, experiments have explored the use of silicon (Si) nanospheres to exhibit strong magnetic dipole (MD) resonances at visible

frequencies [95]. When electromagnetic waves interact with these dielectric nanoparticles at specific resonance frequencies, unique light-matter interactions and properties emerge. Precise control over resonant behavior and light interaction is enabled by employing high refractive index dielectric nanoparticles. Manipulating properties such as size, shape, and refractive index of these nanoparticles allows for achieving desired optical responses, including high transmission efficiency or low-loss high reflection [96]. For example, arrays of silicon (Si) nanodisks can achieve high transmission efficiency in metasurfaces [97,98].

While metals like gold and silver are renowned for their reflective properties, their inherent absorption loss hinders achieving perfect reflection. Bragg reflectors, composed of multilayer arrays of high and low-index dielectric films, create photonic band gaps for effective light reflection within specific wavelength ranges. However, to ensure desired functionality and effective reflection, the thickness of Bragg reflector layers must exceed the incident light's wavelength [99–101]. The primary limitation of Bragg reflectors lies in the time-consuming and costly process of depositing multiple layers of dielectric materials. To overcome this limitation, Silicon on Insulator (SOI) dielectric metasurfaces emerge as a promising alternative, utilizing silicon's low-loss properties to achieve optimal reflectivity. SOI dielectric metasurfaces leverage silicon's unique properties atop an insulating layer typically made of silicon dioxide (SiO_2). This configuration establishes a distinctive interface facilitating light manipulation at subwavelength scales. The design of dielectric metasurfaces capitalizes on the interaction between incident electromagnetic waves and the structured silicon layer.

In this chapter, we initially showcased the feasibility of exciting ED and MD responses within the visible range of the electromagnetic spectrum. We thoroughly investigated significant parameters such as effective permittivity ($\varepsilon_{eff.}$) and effective permeability ($\mu_{eff.}$), alongside reflection coefficient (S_{11}) and transmission coefficient (S_{21}), to characterize the proposed metasurface. Moreover, we identified a wide spectral region conducive to achieving perfect reflection at the resonance wavelength. The tunability of the proposed structure was demonstrated by adjusting

parameters such as the gap region 'g', the thickness of the dielectric silica layer (t_s), and the silicon resonator's thickness (t_m). Finally, we illustrated that the scattering parameter's response remains consistent regardless of the structure's rotation, highlighting the homogeneity of the designed structure across the entire visible spectrum.

4.2 MATERIALS AND STRUCTURE

A thick substrate made of silica aerogel, which is an insulator material with exceptional properties such as a very low refractive index close to that of air and high optical transparency [102–104], is utilized in conjunction with a Si metasurface reflector unit cell. This unit cell consists of V and W shaped structures with nanometer-scale gaps between them, forming a pattern resembling the letters V and W along with their mirror images. The substrate's refractive index in the visible wavelength range (400-700 nm) is approximately 1.08, which is close to air [105]. The design parameters of the proposed metasurface unit cell are represented symbolically and detailed in Table 4.1, with a schematic illustration provided in Figure 4.1 depicting both side and top views of the unit cell.
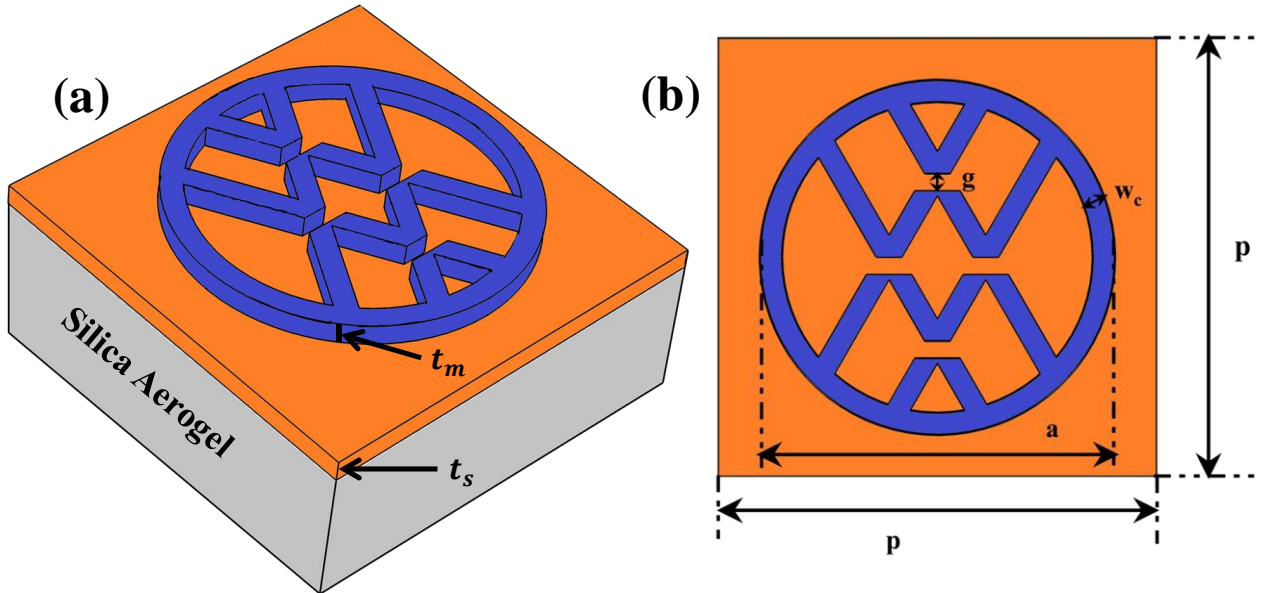
Figure 4.1 The schematic diagram of the proposed dielectric metasurface reflector showing its **(a)** Side view and **(b)** top view with blue, orange and silver portions representing the Si resonator, Silica dielectric layer and Silica Aerogel substrate, respectively.

In the simulation setup, an electromagnetic plane wave is employed to illuminate the reflector from above (along the vertical direction or k direction), with the electric field oriented along the y-axis.

To simulate the behavior of each unit cell of the metasurface reflector, specific boundary conditions are applied. PEC conditions are enforced along the x-axis, ensuring complete reflection and zero penetration of electric fields. Similarly, PMC conditions are imposed along the y-axis, reflecting magnetic fields entirely and preventing their penetration.

Table 4.1 Unit cell parameters

Parameters	Value (nm)	Description
p	350	period of unit-cell
a	280	diameter of the outer circle
w_c	17.5	width of edges
g	13	gap between edges
t_s	17.5	thickness of Silica layer
t_m	17.5	thickness of material

4.3   DESIGN METHODOLOGY

The iterative process of optimizing the design of the proposed dielectric metasurface reflector has been conducted, as illustrated in Figure 4.2.

In the initial design (Design 1), a W-shaped silicon resonator with a thickness of 17.5 nm (w_c) is placed on a Silica aerogel substrate, achieving a reflectance of 99.66%, shown in Figure 4.3. To improve upon this, Design 2 introduces a mirrored version of Design 1 with a gap of 13 nm, resulting in a reflectance of 99.68%. Moving on to Design 3, a V-shaped structure is added along with its mirror image, along with the gap 'g' and resonator thickness 'w_c', increasing the reflectance to 99.85%. However, the goal is to create a nearly perfect reflectance metasurface, leading to the creation of Design 4. In this design, Design 3 is enclosed in a circle with the same resonator thickness and a diameter of 245 nm, achieving a reflectance of 99.99%. Design 4 stands out as the nearly perfect reflector with this high reflectance value.

Design 1

Design 2

Design 3
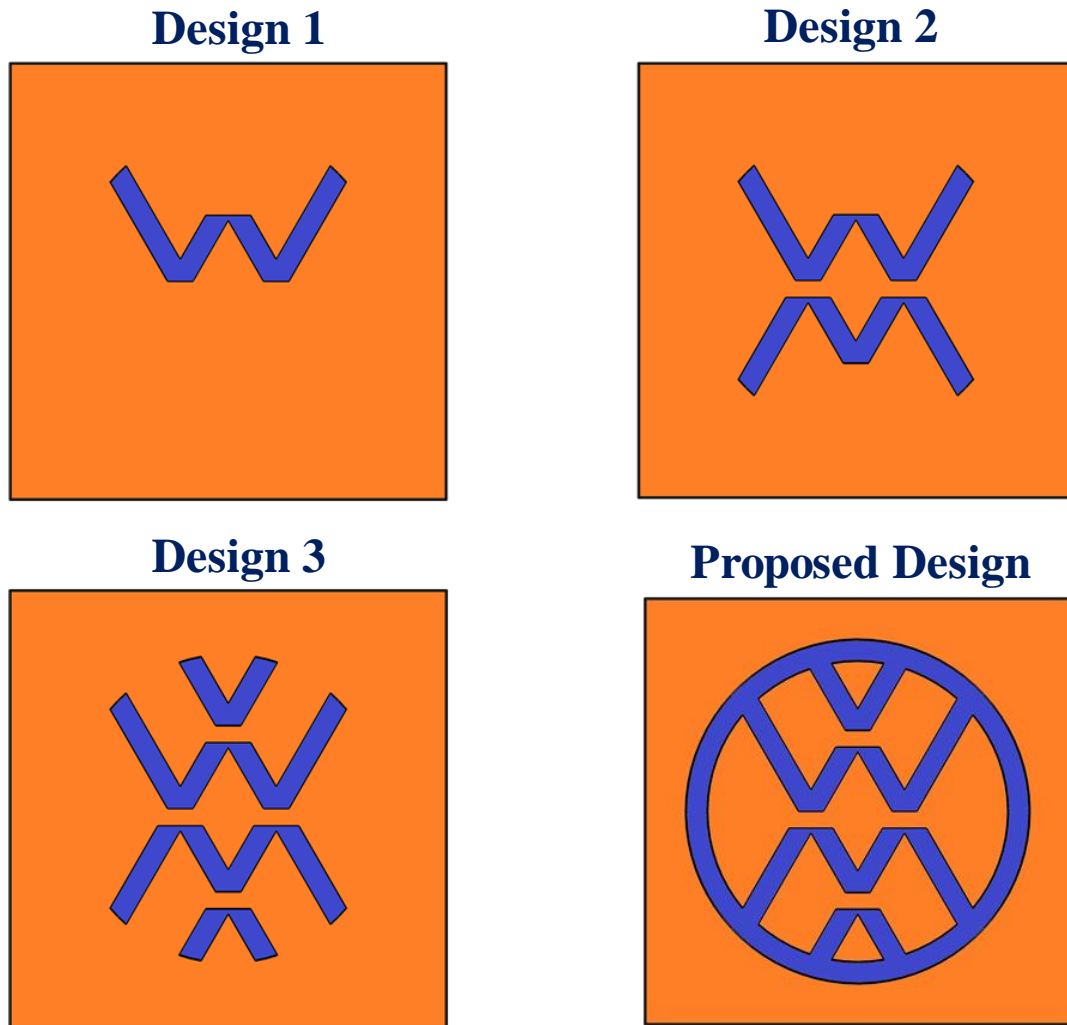
Proposed Design

Figure 4.2 Design layout for the proposed dielectric metasurface reflector unit cell.
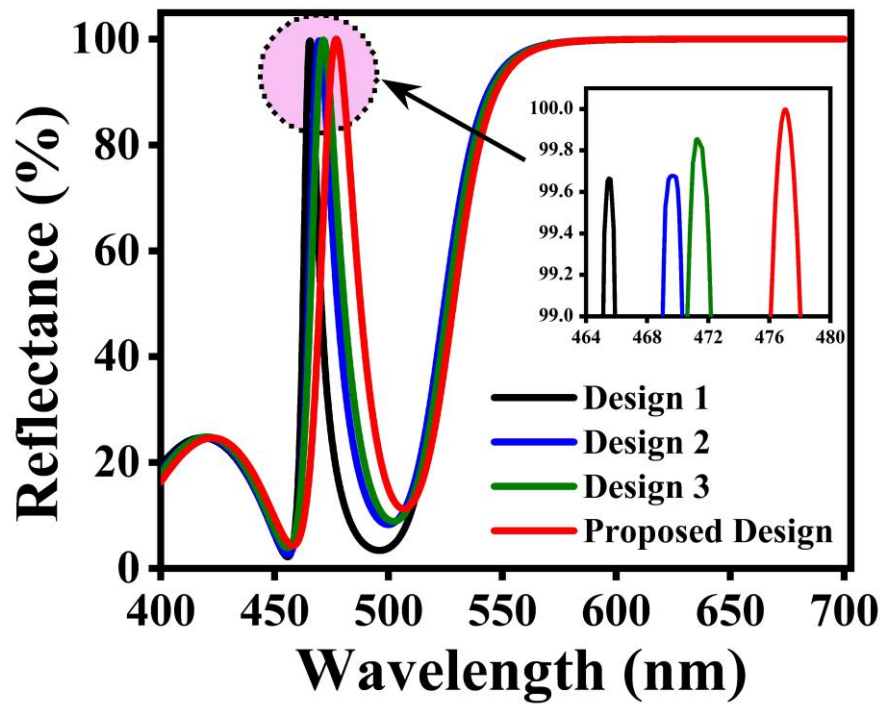
Figure 4.3 The variation of reflectance based on the evaluation of metasurface unit cell designs.

4.4   RESULTS AND DISCUSSION

Figure 4.4 illustrates the changes in reflectance across different wavelengths for the suggested dielectric metasurface, displaying both ED and MD resonances. Our observation reveals a distinct reflection peak at approximately 477 nm, where the reflectance nearly reaches 100%. Additionally, a wide-ranging perfect reflection is evident beyond the 600 nm wavelength.
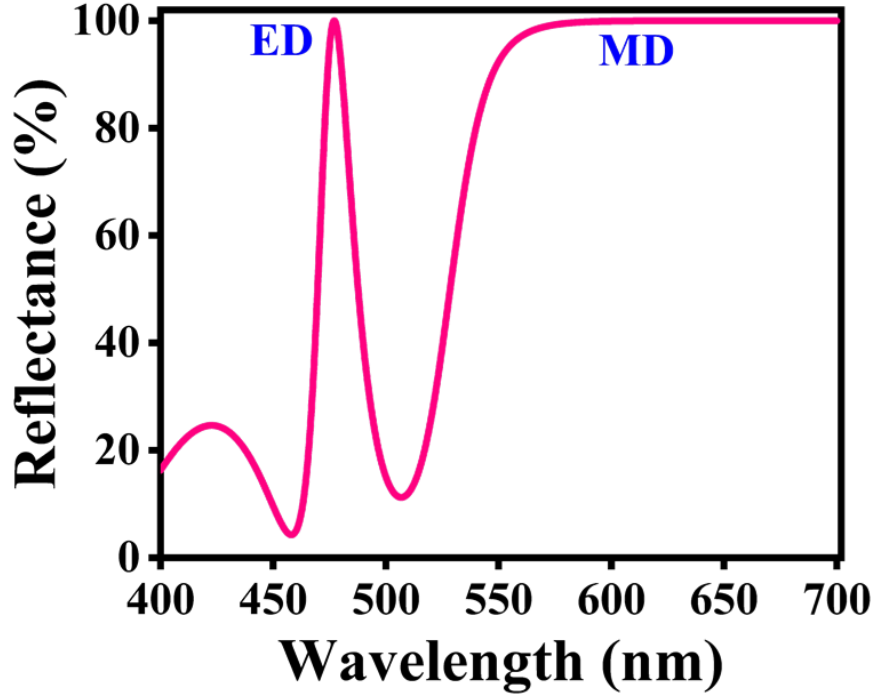
Figure 4.4 Simulated Reflectance for the proposed designed structure. Perfect reflectance is present at both the ED and MD modes.

We utilized a theoretical approach to leverage the underlying physics to efficiently analyze the perfect reflection attributes of our silicon-on-insulator (SOI) dielectric metasurface. When light undergoes vertical reflection from a surface, the complex reflection coefficient can be expressed as stated in reference [78]:

$$r = r_o e^{i\varphi} = \frac{Z - \eta_m}{Z + \eta_m} \qquad\qquad 4.1$$

$$Z = z' + iz'' = \sqrt{\mu/\varepsilon} \qquad\qquad 4.2$$

$$\eta_m = \sqrt{\mu_m/\varepsilon_m} \qquad\qquad 4.3$$

Here, r_o and φ represent the magnitude and phase of the reflection, respectively, while Z denotes the effective complex impedance of the reflector, and η_m is the characteristic impedance of the incident medium, which depends on its permeability and permittivity. In our case, the surrounding medium is air, so $\eta_m = 1$. Consequently, the reflectance (R) can be expressed as provided in reference [106]:

$$R = |r|^2$$

4.4

Using equations. 4.1 and 4.2 we get,

$$R = \left|\frac{Z-1}{Z+1}\right|^2 = \left|\frac{(z'-1)+iz''}{(z'+1)+iz''}\right|^2 = \frac{(z'-1)^2 + z''^2}{(z'+1)^2 + z''^2}$$

4.5

Achieving $R = 1$ is essential for perfect reflection. It can be proven that all solutions require $z' = 0$, without any constraint on z''. Following some simple mathematical manipulations, a solution where $z' = 0$ leads to perfect reflection, meeting the following criteria:

$$\frac{\varepsilon'}{\mu'} < 0$$

4.6

$$\varepsilon''\mu' - \varepsilon'\mu'' = 0$$

4.7

Equation (4.6) can be fulfilled if either ε' or μ' possesses negative values, meaning they must exhibit opposite polarities. This illustrates the necessity for a single-negative metasurface characteristic at the operational wavelength to achieve perfect reflection. Conversely, negative index metasurfaces require both ε' and μ' to be negative. However, meeting the criterion in equation (4.7) seems more challenging, although lossless metasurfaces can achieve it effortlessly. The reflectance of the proposed SOI dielectric metasurface under various incident angle variations is depicted in Figure 4.5. The findings derived from Figure 4.5 reveal a steady decline in the overall reflectance as the incident angle deviates from normal incidence. The graph consistently trends downward as the incident angles increase, indicating that the proposed structure achieves its highest broad reflectance in the visible region when the wave is incident normally.
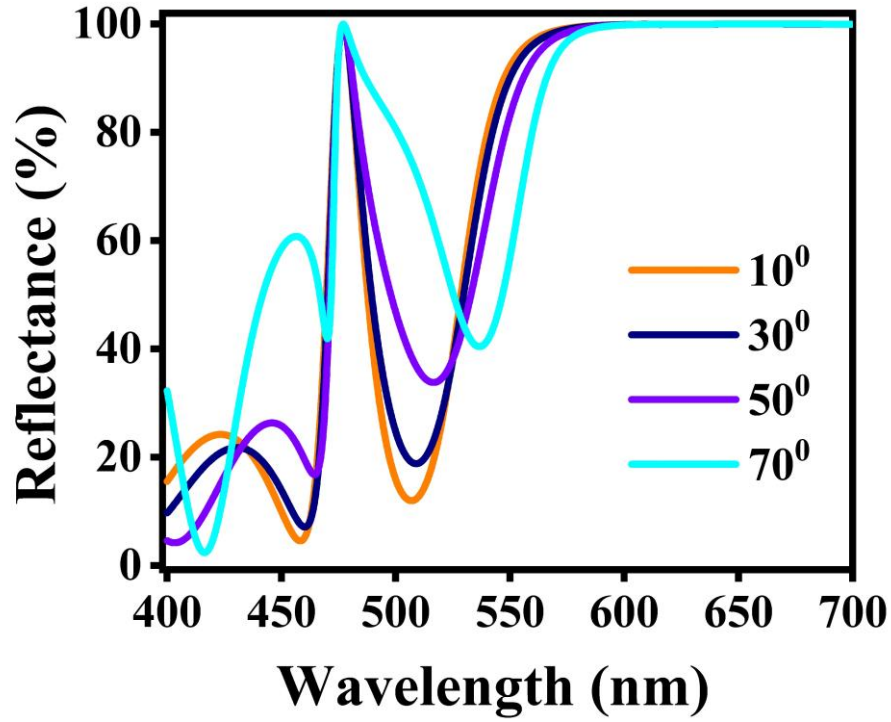
Figure 4.5 Simulated curves of reflection vs wavelength with different incident angles.
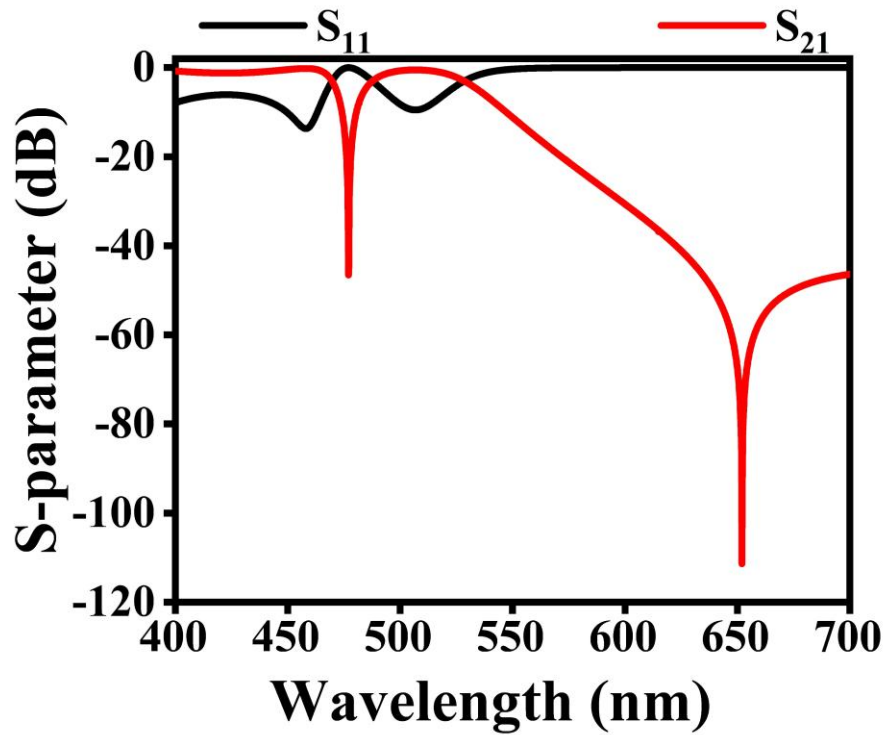
Figure 4.6 Reflection (S_{11}) and Transmission (S_{21}) coefficient of the proposed metasurface reflector.

The designed structure functions as a reflector due to the resonance of the transmission coefficient (S_{21}) at 477 nm, with a magnitude exceeding -30 dB, indicating nearly negligible transmission at the operating wavelength. This is evident from Figure 4.6. Moreover, at the same wavelength (477 nm), the reflection coefficient (S_{11}) approaches 0 dB, indicating nearly 100% reflectance, as illustrated in

Figure 4.6. Figure 4.7 (a) illustrates the variation of the $\varepsilon_{eff.}$ with wavelength. In the visible wavelength range, $\varepsilon_{eff.}$ displays negative values, with the most negative values aligning with the ED resonance, precisely at the wavelength corresponding to perfect reflectance. This alignment supports the condition of a single-negative (SNG) metasurface (equation 4.6). Moreover, both the real and imaginary components of the $\mu_{eff.}$ approach zero at the electric resonance wavelength (indicated by the green arrow in Figure 4.7 (b)), indicating complete satisfaction of equation (4.7). Similarly, $\mu_{eff.}$ exhibits negative values at the magnetic dipole resonance, while the real and imaginary parts of $\varepsilon_{eff.}$ approach zero at the point indicated by the orange arrow in Figure 4.7 (a), meeting the requirements for perfect reflection outlined in equation (4.7). From this analysis, it is evident that the all-dielectric metasurface demonstrates perfect reflection performance with both electric and magnetic dipole resonances.
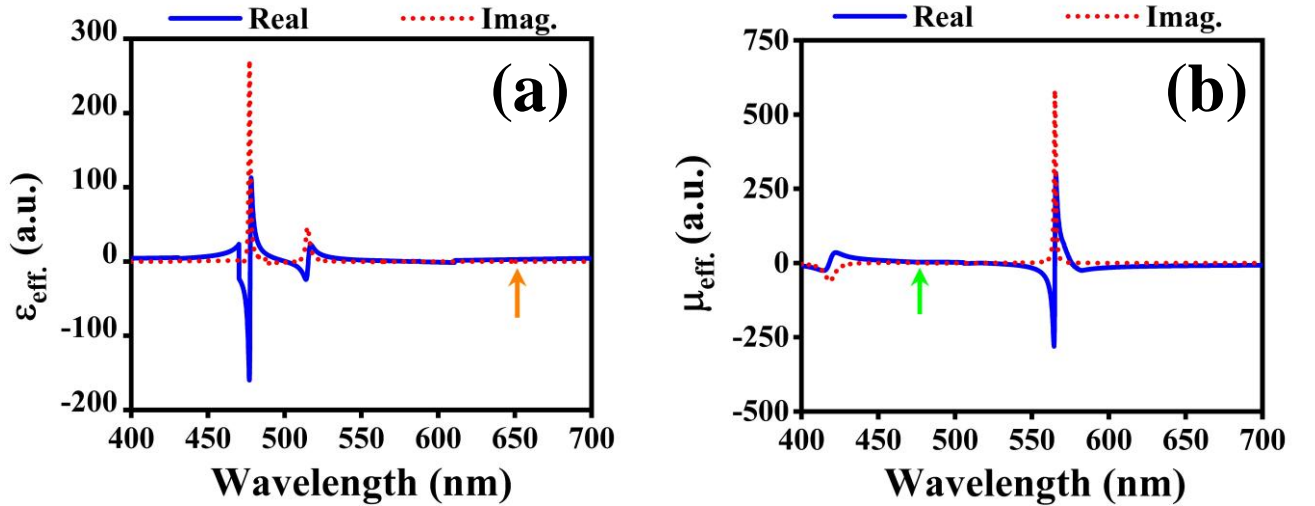
Figure 4.7 (a) Effective permittivity ($\boldsymbol{\varepsilon_{eff.}}$) and **(b)** Effective permeability ($\boldsymbol{\mu_{eff.}}$) for the structure, calculated using S-parameter retrieval method. The solid (dotted) lines show the real (imaginary) parts, and the arrow lines show the points where the conditions for perfect reflection in Eq. (6) are fully satisfied.

The nanogaps demonstrate the highest electric field intensity, reaching 1.12×10^9 V/m at 477 nm, as shown in Figure 4.8 (a). This finding highlights the significant confinement of incident light within the gaps at the resonance wavelength. Additionally, at a resonance wavelength of 652 nm, the electric field achieves a maximum value of up to 1.85×10^8 V/m. Within the unit cell, the gap region exhibits an enhanced and normalized electric field distribution characterized by a vortex-like pattern at wavelengths of 477 nm and 652 nm when the incident electric field is polarized along the y-axis,

as depicted in Figure 4.8 (c) and (d). This enhanced normalized electric field within the gap is attributed to the Capacitive Effect, wherein the gaps in metasurface resonators act as capacitors [107]. As the gap size decreases, the capacitance also decreases. In a capacitor, the electric field is inversely proportional to the gap size and directly proportional to the charge stored on the capacitor plates.
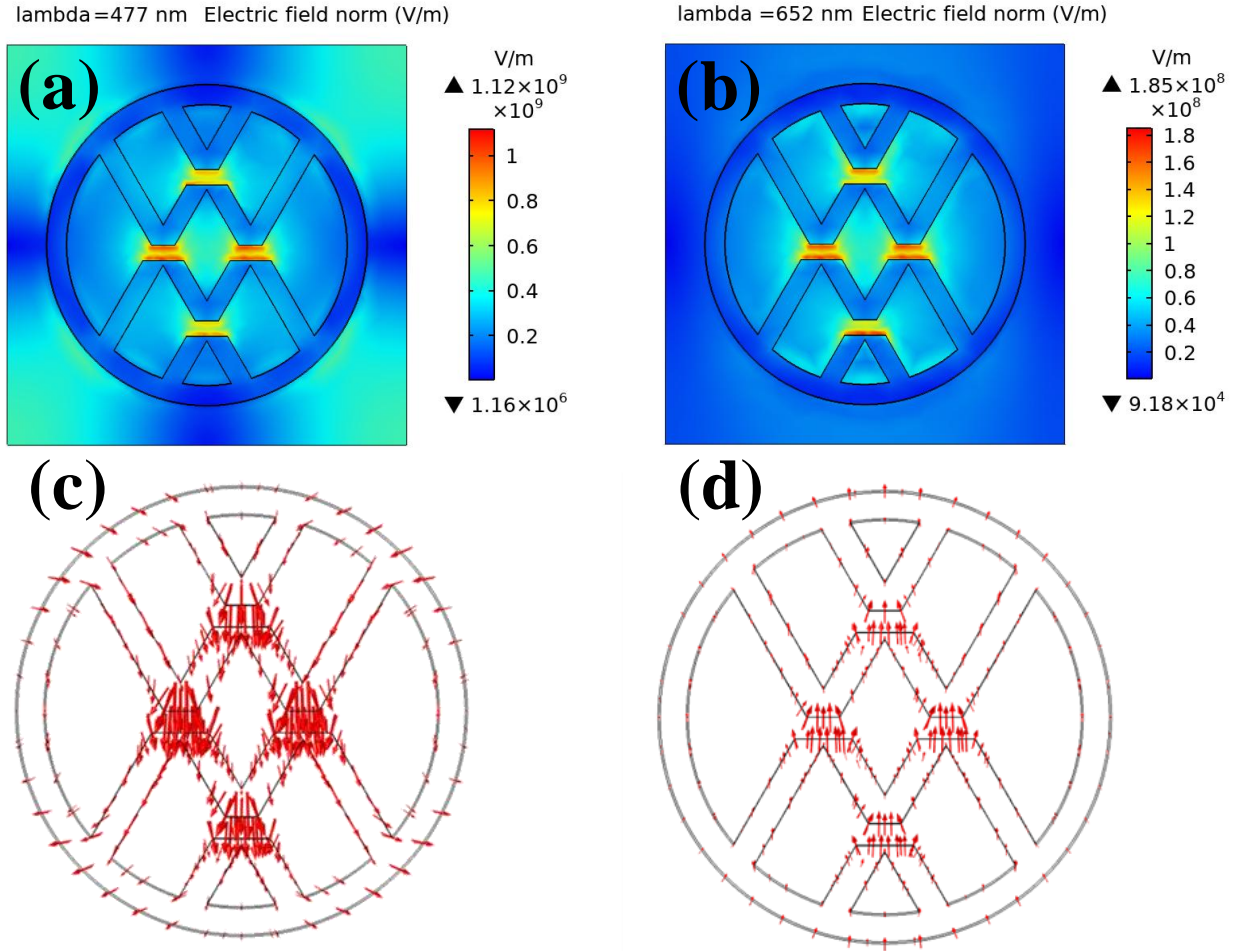
Figure 4.8 Simulated electric field at **(a)** 477 nm and **(b)** 652 nm for proposed designed dielectric metasurface, **(c)** Vortex-like normalized and enhanced electric field distribution at the gap region of unit-cell at a wavelength of 477 nm and **(d)** 652 nm when the incident electric field is polarized along the y-axis.

This suggests that, for a constant voltage across the gap, a reduction in gap size results in an increase in the electric field. The graphical representation of the normalized electric field in a vortex-like pattern clearly indicates that the electric field is primarily confined within the gap region of the unit cell. Moreover, the confinement of the magnetic field is also investigated at resonance wavelengths of 477 nm and 652 nm, as depicted in Figure 4.9. It is noted that the magnetic field reaches its maximum intensity at areas where the electric field is at its minimum, and vice versa. Consequently, the resonance wavelength has a minimal impact on the magnetic field within the gap regions.

However, in the left and right segments of the proposed metasurface, magnetic fields of approximately 1.53×10^6 A/m and 2.06×10^5 A/m are present at resonance wavelengths of 477 nm and 652 nm, respectively. The vortex-like pattern depicted in Figure 4.9 (c) and (d) illustrates that the normalized magnetic field attains its maximum extent at the resonance wavelength. Within this visualization, the maximum concentration of magnetic field lines occurs in the right and left sections of the unit cell, coinciding with the areas where the electric field is minimized.
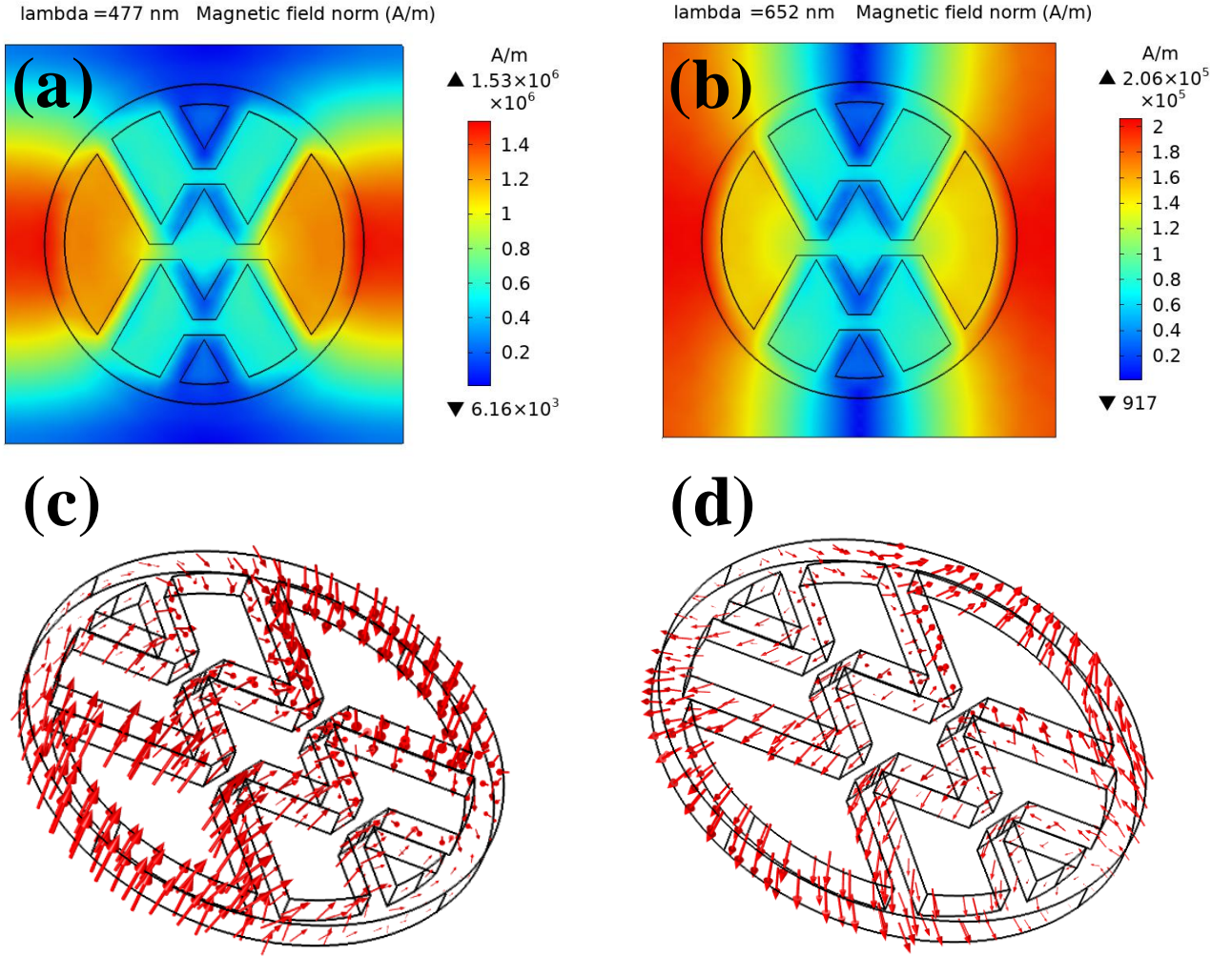
Figure 4.9 Simulated magnetic field at **(a)** 477 nm and **(b)** 652 nm for proposed designed dielectric metasurface, **(c)** Vortex-like normalized and enhanced magnetic field distribution in the unit-cell at a wavelength of 477 nm and **(d)** 652 nm.

4.4.1 Tunability characteristics of the proposed structure

In this section, the tunability properties of the proposed dielectric metasurface structure are explored through three different approaches: (1) by varying different gap (g) values, (2) by adjusting the

thickness of the silica layer (t_s), and (3) by varying the thickness of the silicon resonator (t_m). To begin with, the investigation focuses on the variation of the electric field with different gap values (g) at the resonance wavelength for the designed structure, as illustrated in Figure 4.10.
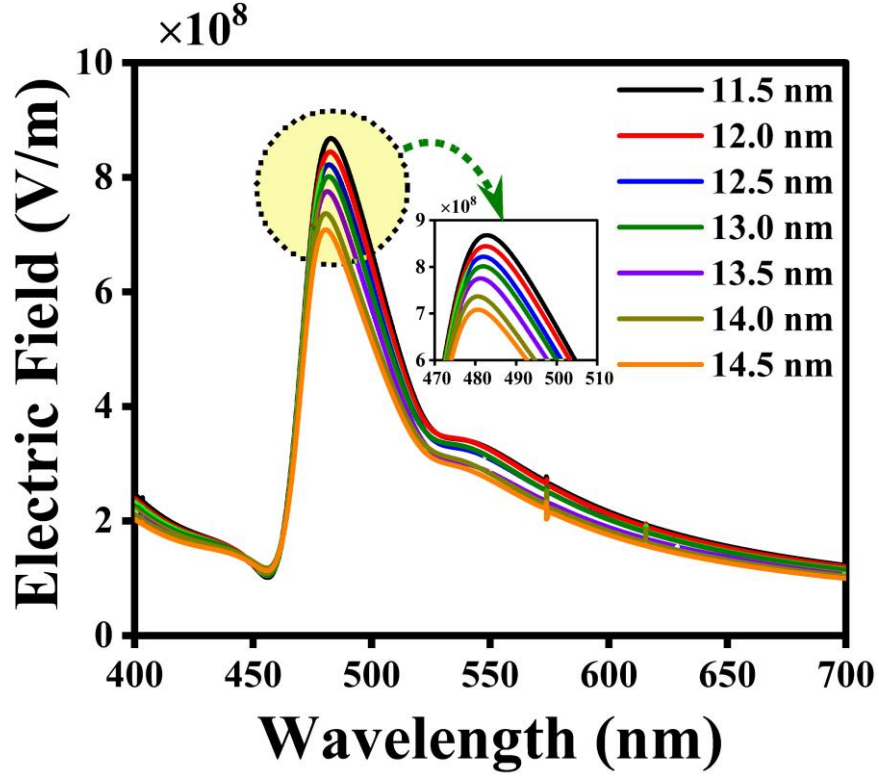
Figure 4.10 Variation of electric field with different gap values (g) at resonance wavelength of the proposed dielectric metasurface.

Figure 4.10 clearly demonstrates that as the gap 'g' increases from 11.5 nm to 14.5 nm, the electric field decreases. This variation is evident in the inset of Figure 4.10. The decrease in electric field values within the gap as the gap size increases is attributed to the Capacitive Effect, where the gaps in metasurface resonators function as capacitors [107]. With an increase in gap size, the capacitance of the gap also increases. In a capacitor, the electric field is inversely proportional to the gap size and directly proportional to the charge stored on the capacitor plates. Consequently, for a fixed voltage across the gap, an increase in gap size leads to a decrease in the electric field. The tunable characteristics of the proposed structure are dependent on the variation of different gap values, resulting in a change in the electric field at the resonance wavelength. Moving forward, the thickness of the dielectric silica layer (t_s) is adjusted to observe the variation in the resonance wavelength of the proposed metasurface structure, as depicted in Figure 4.11 (a).

Increasing the thickness of the dielectric silica layer (t_s) from 7.5 nm to 37.5 nm induces a noticeable redshift at the lower resonance wavelength (S_{21}), while at higher resonance wavelengths, the shift is towards the lower side, resulting in a blueshift, as depicted in Figure 4.11 (a). Subsequently, the behavior of the resonance wavelength is examined with variations in the thickness of the silicon resonator (t_m), as illustrated in Figure 4.11 (b). As t_m changes from 7.5 nm to 37.5 nm, there is a shift in the resonance wavelength towards higher values, indicating a redshift at the lower resonance wavelength in the S_{21} parameter. Similarly, at higher wavelengths, the shift is towards lower values, demonstrating a blueshift in S_{21}. This modulation of t_s and t_m aligns with the tunability characteristics of the designed structure, resulting in shifts in the resonance wavelength.
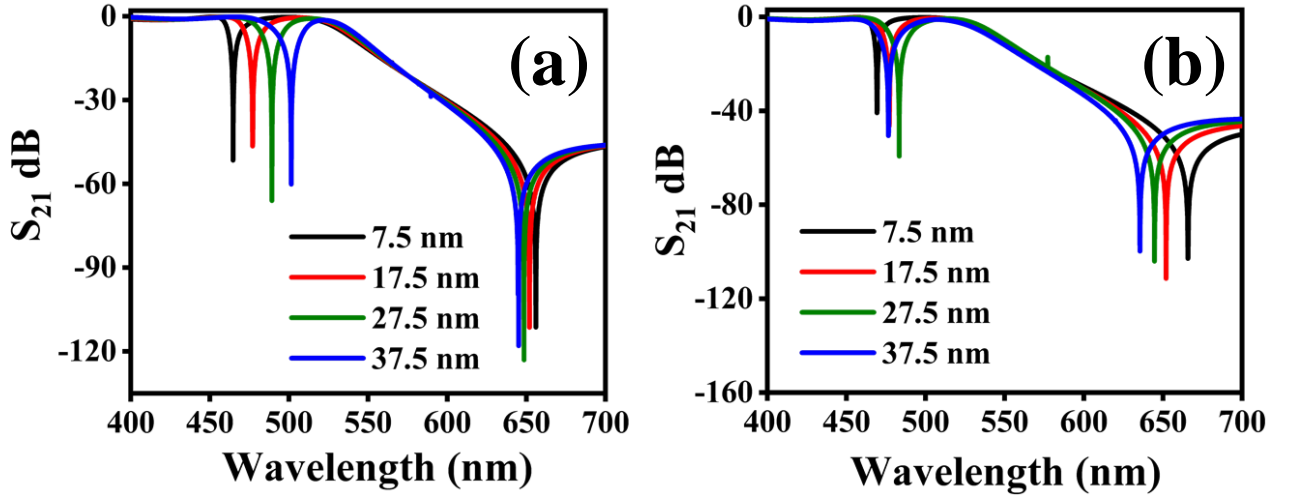
Figure 4.11 The variation in S_{21} parameter with (a) the thickness of Silica dielectric layer ($\boldsymbol{t_s}$) and (b) thickness of Si resonator ($\boldsymbol{t_m}$).

4.5 SUMMARY

In summary, we have proposed design and structure of an innovative all-dielectric metasurface serving as a perfect reflector, constructed from SOI material. Utilizing Finite Element Method-based COMSOL Multiphysics simulation software, we examined the optical scattering properties of the designed metasurface structure. Our analysis revealed the excitation of ED and MD resonances within the visible region. Employing the NRW method, we calculated the effective electromagnetic parameters and further investigated the distribution of electric and magnetic fields at the resonant wavelengths, showcasing their opposite symmetry. By manipulating the gap region 'g', the thickness

of the dielectric silica layer (t_s), and the Si resonator (t_m), we explored the tunability characteristics of the proposed structure. Additionally, we demonstrated the consistent response of the scattering parameters, regardless of the rotation of the structure, highlighting the uniformity of the designed structure across the entire visible spectrum.

CHAPTER- 5

CHAPTER 5: DUAL BAND METAMATERIAL FOR REFRACTIVE INDEX SENSING APPLICATION

5.1   INTRODUCTION

In the previous chapter, Silicon on Insulator metasurface has been utilized to obtain broadband perfect reflection in visible spectrum. This chapter focuses on designing, fabricating and analysing a metamaterial structure, with refractive index sensing application. Designed structure features a quad-band plasmon resonance-enabled dual-band metamaterial, operating in the S and C bands of the microwave region. The S (2-4 GHz) and C (4-8 GHz) bands are crucial for various applications such as wireless communications [108], radar navigation [109] and remote sensing [110], etc. However, conventional materials face limitations in achieving desired performance levels in these frequency ranges. MTMs have emerged as a groundbreaking solution, manipulating electromagnetic waves in unconventional ways [102,111,112]. Zero-index metamaterials (ZIMs) offer unique advantages like electromagnetic cloaking and beam splitting due to their zero refractive index [30]. In sensor applications, MTMs have shown promise in achieving high sensitivity, but challenges remain in simplifying fabrication processes. Previous studies have attempted to improve sensitivity in specific frequency bands but have encountered limitations [113–115]. Therefore, there's a need for an enhanced dual-band MTM sensor capable of achieving high sensitivities in both S and C bands.

Improving the bandwidth is crucial for compactness and miniaturization of MTMs. Prior research has introduced various MTM structures with different bandwidths across multiple frequency bands. However, existing structures have shown limitations [69,107,116–118], indicating the necessity for improved designs with wider bandwidths, especially in the C-band.

In this chapter, we have developed and analyzed a new MTM structure tailored for dual-band functionality, emphasizing a broad bandwidth within the C-band for applications in refractive index

sensing. Through Finite Element Method (FEM) simulations, we examined the scattering parameters of the MTM unit cell, or meta-atom, and corroborated our findings with experimental data. Our analysis highlights the presence of negative and near-zero effective refractive index (NZI) and epsilon near zero (ENZ) characteristics within the dual-band range, encompassing both S and C bands in the microwave spectrum. The designed MTM structure exhibits a substantial EMR of up to 6.93, affirming the compact nature of our design. Our findings suggest that this MTM structure holds promise for enhancing the efficiency and compactness of devices and components in wireless communication systems, owing to its compact size, dual-band resonance, and wide C-band bandwidth. When employed as a refractive index sensor, our proposed MTM demonstrates high sensitivity, specifically reaching 1 GHz/RIU and 3 GHz/RIU. This study introduces a promising alternative technique for creating high-performance multi-function sensors with exceptional sensing capabilities, suitable for applications in biochemical sensing, medical detection, and diagnostics.

5.2 FABRICATION AND MODELLING OF THE DESIGNED MTM STRUCTURE

The diagram illustrating the meta-atom of the intended MTM structure is shown in Figure 5.1 (a), which is also utilized for simulation purposes. Figure 5.1 (b) depicts the actual prototype array of the structure, extended periodically on all sides with a 16×16 mm² periodicity. A top view of the fabricated meta-atom (unit cell) structure is presented in Figure 5.1 (c). This MTM design comprises a Copper (Cu) resonating patch on a 1.6 mm thick epoxy resin fiber substrate. The fabrication process involves using a computer numerical control (CNC) machine to create unit cells of 16×16 mm² dimensions and a prototype array of 10×10, as depicted in Figure 5.1 (b). Beginning with designing the layout using Computer-Aided Design (CAD) software, the blueprint guides subsequent steps. The design is then transferred onto a screen or mask for printing, followed by material deposition using screen printing, which applies the material onto the substrate according to the design. Etching is conducted to refine the MTM structure's geometry by removing excess material. Finally, the

fabricated MTM undergoes cleaning to remove any residues or contaminants. All relevant physical parameters are detailed in Table 5.1.
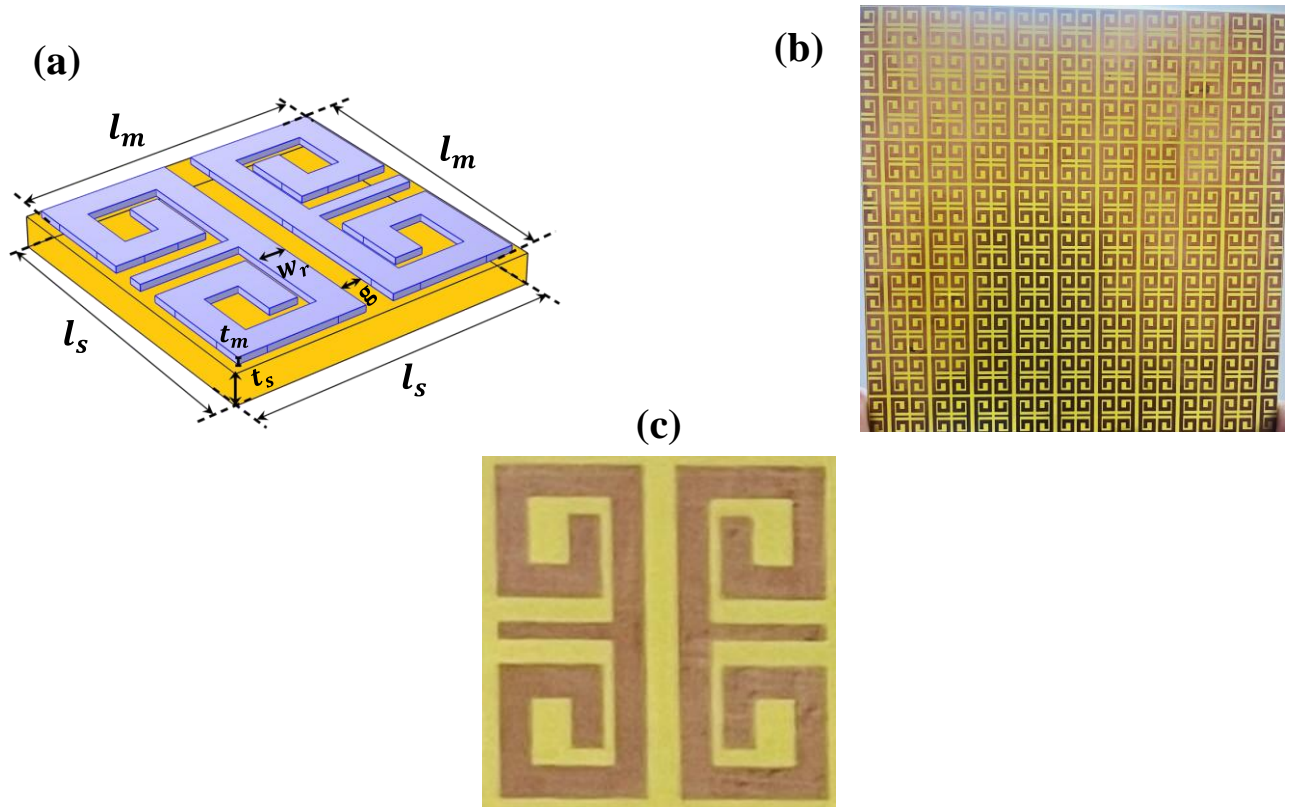
Figure 5.1 (a) The meta-atom or unit cell of the simulated MTM design from an orthogonal view. **(b)** The physical prototype array of the fabricated MTM design, and **(c)** the top view of the meta-atom of the fabricated sample.

Table 5.1 The parameters of the fabricated and simulated designed unit cell MTM structure.

Parameter	Value (mm)	Description
l_m	15	length of material
g	1.5	middle gap
l_s	16	length of substrate
w_r	1.5	width of resonator
t_s	1.6	thickness of substrate
t_m	0.35	thickness of resonator

The structure proposed is designed and simulated through the FEM based COMSOL Multiphysics simulation software, as illustrated in Figure 5.1 (a). In this design, the copper material patch has a thickness (t_m) of 0.35 mm and an electrical conductivity (σ) of 5.99×10^7 S/m [69]. The dielectric substrate employed in the research has a loss tangent (δ) of 0.025 radians and a permittivity (ε) of 4.3 [69,107].
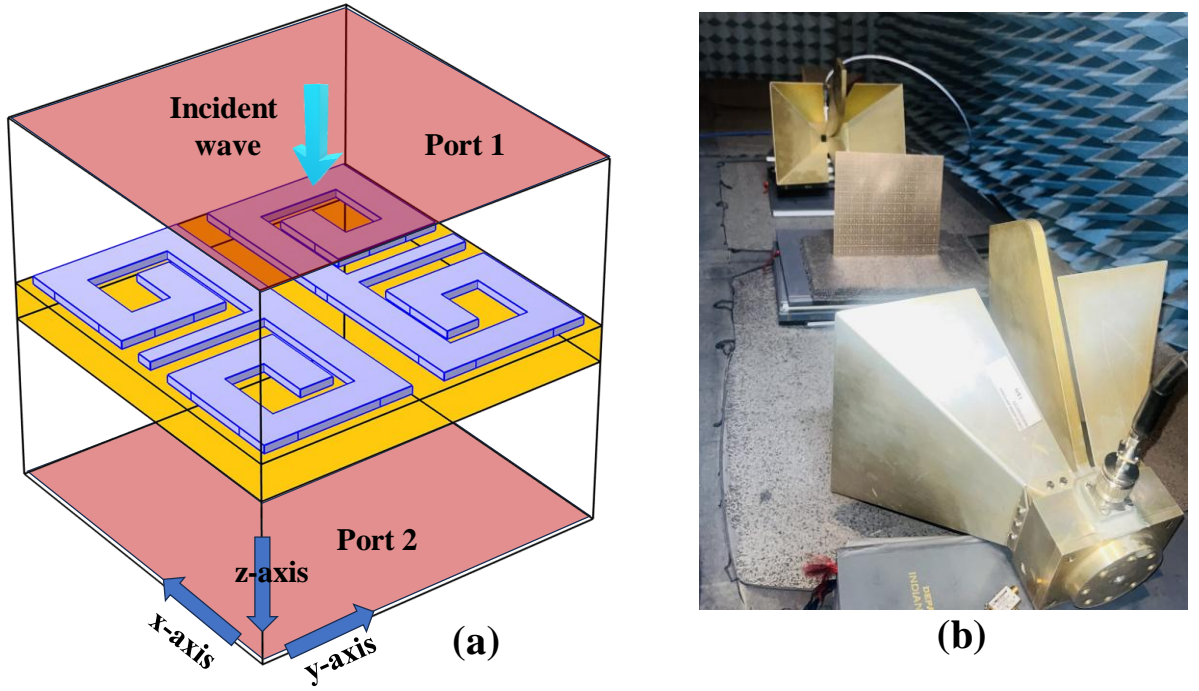
Figure 5.2 (a) Simulation analysis and **(b)** Experimental measurement setup of the designed MTM.

The S_{21} measurement in the experiment utilizes an Antenna test setup, as shown in Figure 5.2 (b). The whole measurement technique explained briefly in the Section 1.5 of CHAPTER 1: . Figure 5.3 (a) shows a comparison between the simulated and experimentally observed transmission coefficient (S_{21}) responses for the fabricated design structure. Additionally, Figure 5.3 (b) displays the phase plot of scattering parameters.
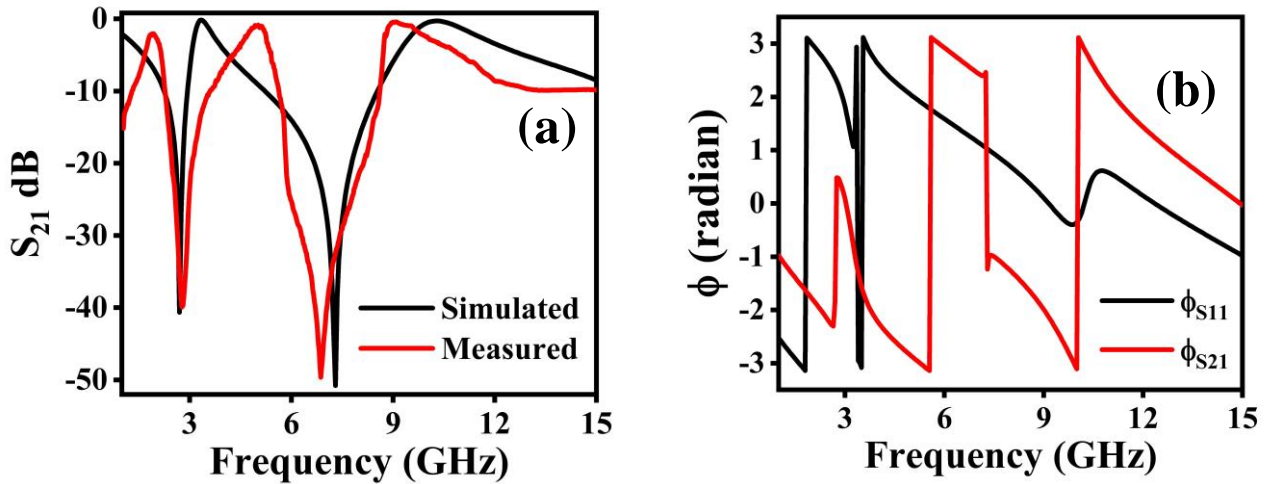
Figure 5.3 (a) The transmission coefficient (S_{21}) for the Simulated and measured response and **(b)** the phase plot of the scattering parameter at different incident wave frequencies of the unit cell structure.

The experimental findings closely match the results obtained through simulation, considering the limitations of the experimental setup. In Figure 5.3 (a), a slight deviation between the experimentally

measured and simulated transmission coefficient (S_{21}) is observed, likely due to factors such as manufacturing discrepancies, signal interference, and reflection noise. These factors contribute to minor shifts in resonance frequencies, evident in the measurement outcomes. However, both simulated and experimental data cover the S and C frequency bands. Analysis of the S_{21} parameter of the designed MTM unit cell reveals resonance frequencies at 2.7 GHz and 7.3 GHz, corresponding to the microwave S-band and C-band commonly used in wireless communication. Figure 5.3 (b) illustrates the phase plot of output scattering parameters (S_{11} and S_{21}), showing variations from -π to +π with a total phase change of 2π. The bandwidth of S_{21}, crucial for wireless communication, is significant across different frequency bands, spanning 0.44 GHz (2.42-2.86 GHz) and 1.98 GHz (6.10-8.08 GHz) for the S and C bands, respectively. Notably, the proposed MTM unit cell exhibits a broader bandwidth for the C band compared to previously published data, as summarized in Table 5.2, making it suitable for various wireless communication applications, including satellite and Wi-Fi technologies [69].

Table 5.2 Comparison of different bandwidth of proposed work with the previously published work.

References	Dimension (physical and electrical)	Resonance Frequencies (GHz)	Frequency band	Effective Bandwidth (GHz)
[116]	8×8 mm^2 (0.070λ×0.070λ)	2.61, 6.32, 9.29	S, C, X	0.11, **0.79**, 0.15
[107]	8×8 mm^2 (0.06λ×0.06λ)	2.48, 4.28, 9.36, 13.7	S, C, X, Ku	0.19, **0.4**, 1.3, 0.6
[117]	10×10 mm^2 (0.14λ×0.14λ)	4.20, 10.14, 13.15, 17.1	C, X, Ku	**0.72**, 1.55, 0.17, 0.24
[69]	10×10 mm^2 (0.17λ×0.17λ)	5.0, 6.88, 8.429	C, X	**1.67**, 0.52, 0.98
[118]	15×15 mm^2 (0.20λ×0.20λ)	3.36, 7.41, 10.16	S, C, X	1.51, **0.94**, 0.89
Present work	16×16 mm^2 (0.07λ×0.07λ)	2.7 and 7.3	S, C	0.44, **1.98**
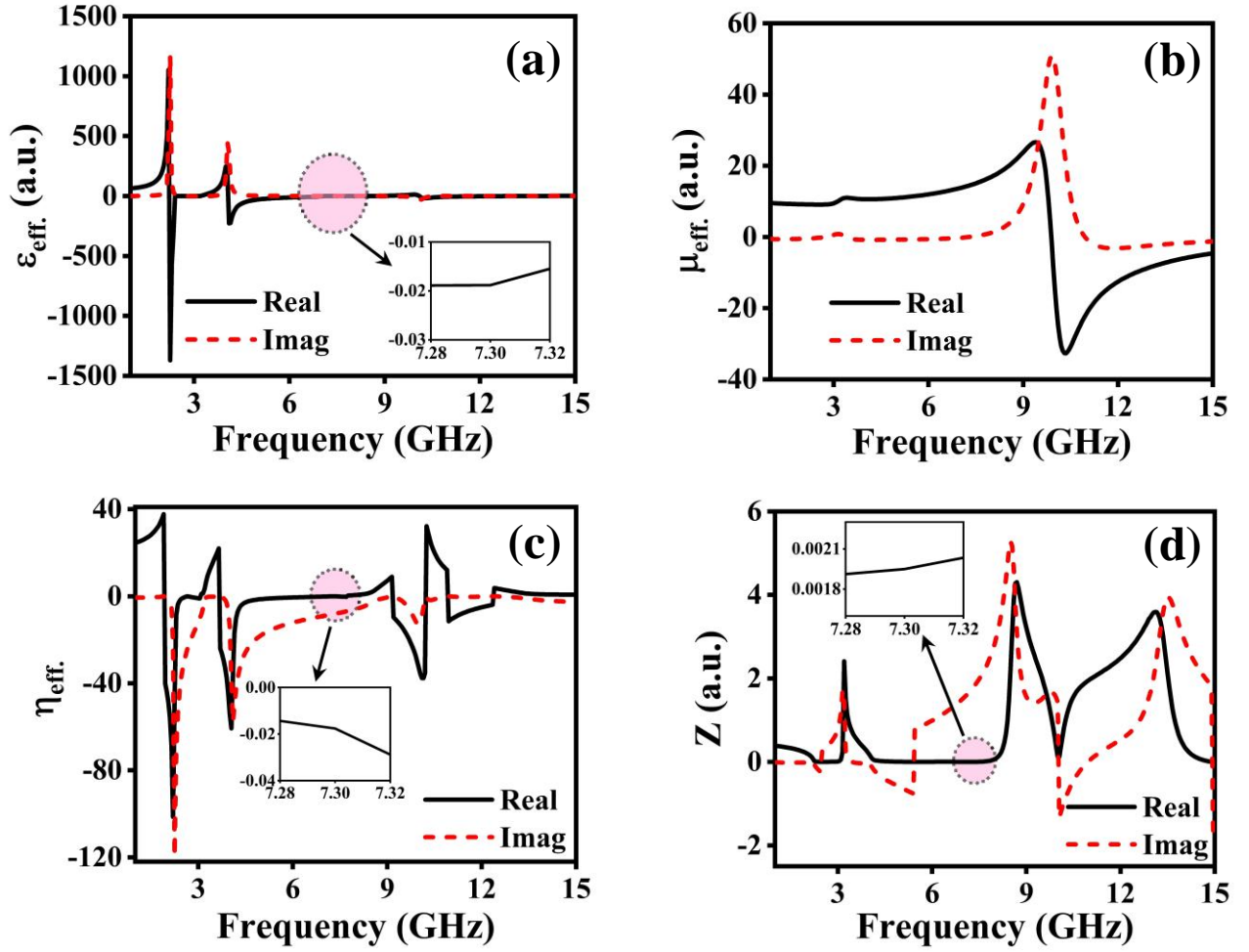
Figure 5.4 Variation of **(a)** effective permittivity ($\boldsymbol{\varepsilon_{eff.}}$), **(b)** effective permeability ($\boldsymbol{\mu_{eff.}}$), **(c)** effective refractive index ($\boldsymbol{\eta_{eff.}}$) and **(d)** normalized impedance (Z) concerning the frequency of the designed MTM unit cell.

The data presented in Figure 5.4 (a, b) illustrate that the proposed Metamaterial (MTM) structure exhibits negative effective permittivity ($\varepsilon_{eff.}$) at resonance frequencies of 2.7 GHz and 7.3 GHz, approaching near-zero values (ENZ) at these frequencies, as depicted in the inset of Figure 5.4 (a). Conversely, the effective permeability ($\mu_{eff.}$) remains positive across all resonance frequencies for the designed metamaterial structure, as shown in Figure 5.4 (b). Additionally, Figure 5.4 (c) indicates that the effective refractive index ($\eta_{eff.}$) displays negative and near-zero values at dual resonance frequencies corresponding to the S and C bands, illustrated in the inset of Figure 5.4 (c). In Figure 5.4 (d), the normalized impedance (Z) shows positive and near-zero real values across the resonance frequencies, as represented in the inset of Figure 5.4 (d). The lower values of normalized impedance at resonance frequencies suggest the passive nature of the designed metamaterial unit

cell, characterized by fixed properties determined by its structural design. Table 5.3 summarizes the overall parameter properties.

Table 5.3 Effective parameter property

Parameters	Resonance Frequency (GHz)	Magnitude	Extracted property
Effective permittivity ($\varepsilon_{eff.}$)	2.7, 7.3	-0.085, -0.588	$\varepsilon_{eff.} < 0$ (ENG), $\varepsilon_{eff.} \sim 0$ (ENZ)
Effective permeability ($\mu_{eff.}$)	2.7, 7.3	9.118, 14.493	$\mu_{eff.} > 0$ (SNG)
Refractive index ($\eta_{eff.}$)	2.7, 7.3	-0.144, -0.017	$\eta_{eff.} < 0$ (LHM), $\eta_{eff.} \sim 0$ (NZI)
Impedance (Z)	2.7, 7.3	0.0030, 0.0019	$Z \sim 0$

In the proposed structure, the unit cell size is observed to be 16 mm, significantly smaller than the operating wavelength for all quad-frequency bands. This adherence to the EMT condition results in the desired characteristics of the metamaterial (MTM). Equation (3.1) can be employed to calculate EMR. The proposed MTM unit cell demonstrates a notably high EMR alongside compact dimensions, allowing it to cover all dual frequency bands (S and C) commonly utilized in satellite and multi-band applications. The calculated EMR value for the designed metamaterial at its operating resonance frequency of 2.7 GHz is 6.93. This relatively high EMR value contributes to the enhanced compactness of the structure, rendering it a promising option for various practical applications.

5.2.1 Optimization of the designed MTM geometry

The optimization process for the proposed MTM structure involves five sequential design steps, outlined in Figure 5.5. Design 1 features four L-shaped metallic strips positioned at the corners of the substrate, resulting in resonance frequencies at 11.65 GHz for the transmission scattering parameter (S_{21}), as illustrated in Figure 5.6. Progressing to Design 2, four horizontal metallic wires are added to the middle edges, leading to resonance frequencies at 7.6 GHz. Design 3 incorporates a central metallic strip into Design 2, generating resonance frequencies at 7.45 GHz. These designs resonate within the single S band.
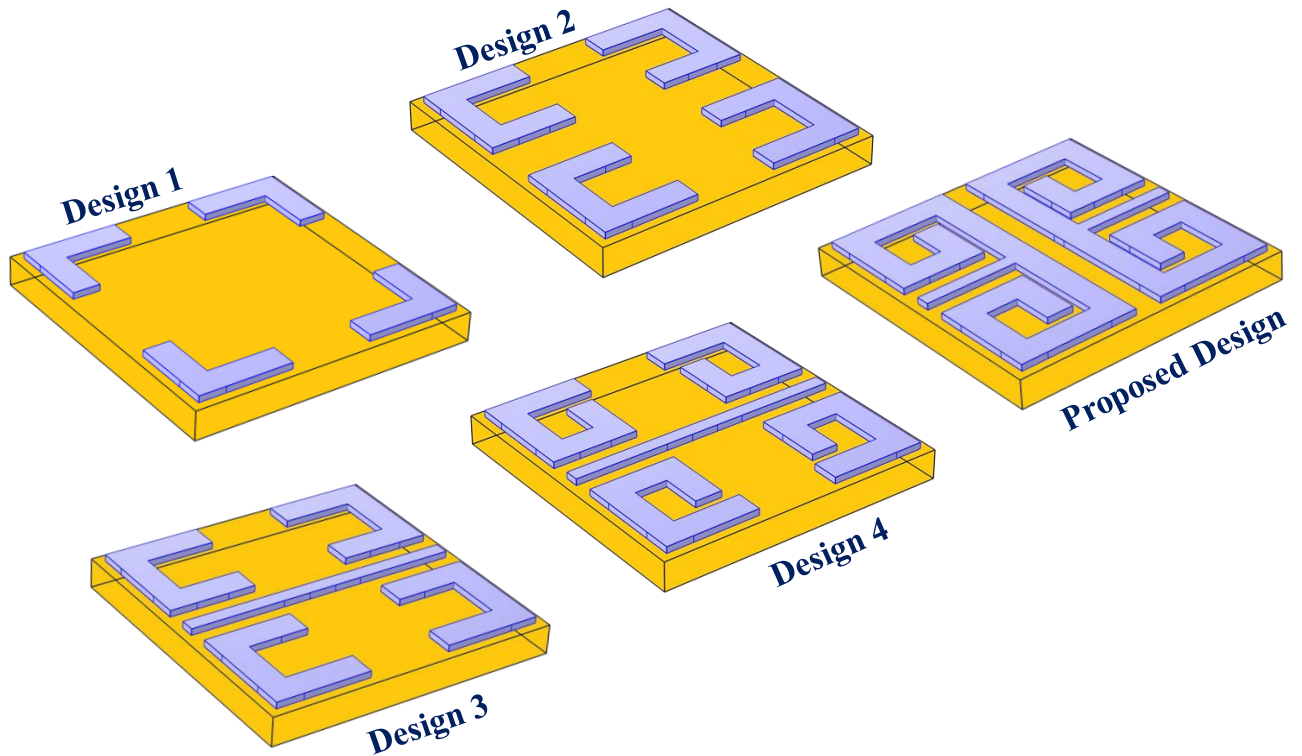
Figure 5.5 The methodological approach employed in creating the MTM structure.
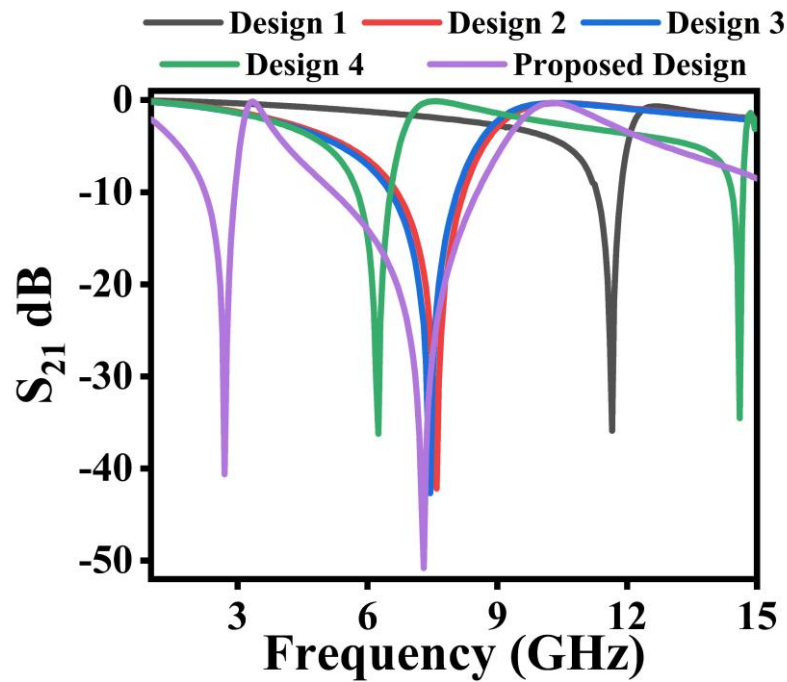
 Figure 5.6 The variation of scattering parameters S_{21} (transmission coefficient) concerning the frequency of the incident electromagnetic plane wave, observed across different MTM structures.

Design 4 enhances Design 3 by introducing four additional vertical metallic strips, resulting in resonance frequencies at 6.25 GHz and 14.6 GHz. However, this design yields narrow-band resonance frequencies despite the occurrence of dual-band resonance. Finally, in Design 5, two

vertical strips are connected at their ends in the center of Design 4, forming an MTM with a mirror image shape. This design reflects dual-band operating resonance frequencies at 2.7 GHz and 7.3 GHz in the S and C bands within the microwave region, as depicted in Figure 5.6. The resonance frequencies of the designed structure stem from the formation of a capacitor and inductor for the gap region and metallic strips, effectively creating an LC circuit resembling an LCR tank circuit [71]. The resonance frequency (f) can be calculated using the formula given in equation 2.1[72].

5.2.2 Electromagnetic Field distribution of the designed Metamaterial

The presence of induced current within the metallic components of MTM results in the generation of a scattering field when interacting with a plane wave. Maxwell's equations offer a comprehensive framework for understanding how the electric field (E), surface current (J), and magnetic field (B) interact within an MTM. When current flows through the conducting elements of an MTM, it generates a magnetic field. However, any alteration in this magnetic field can induce an electromotive force. Consequently, Maxwell's formulation of Ampere's and Faraday's laws yields a set of four differential equations that establish the relationships between electric and magnetic fields, elucidating these phenomena [119]. The behavior of electromagnetic waves within a medium is influenced by various factors such as permeability (μ), permittivity (ε), and conductivity (σ) of the medium. These material properties, in conjunction with the boundary conditions of the medium, play a crucial role in determining its electromagnetic characteristics.

Figure 5.7 (a) and (b) illustrate the magnetic field distribution corresponding to two resonance frequencies: 2.7 GHz and 7.3 GHz, respectively. According to Maxwell's equations, there is a correlation between the magnetic field and surface current density. In Figure 5.7 (a), high magnetic field intensities are observed on the inner side of the structure, particularly near the edges where a larger current density is present. Conversely, Figure 5.7 (b) shows a magnetic field with lower intensity, attributed to the lower current intensity at this frequency. However, the field intensity remains low in other regions of the MTM structure.
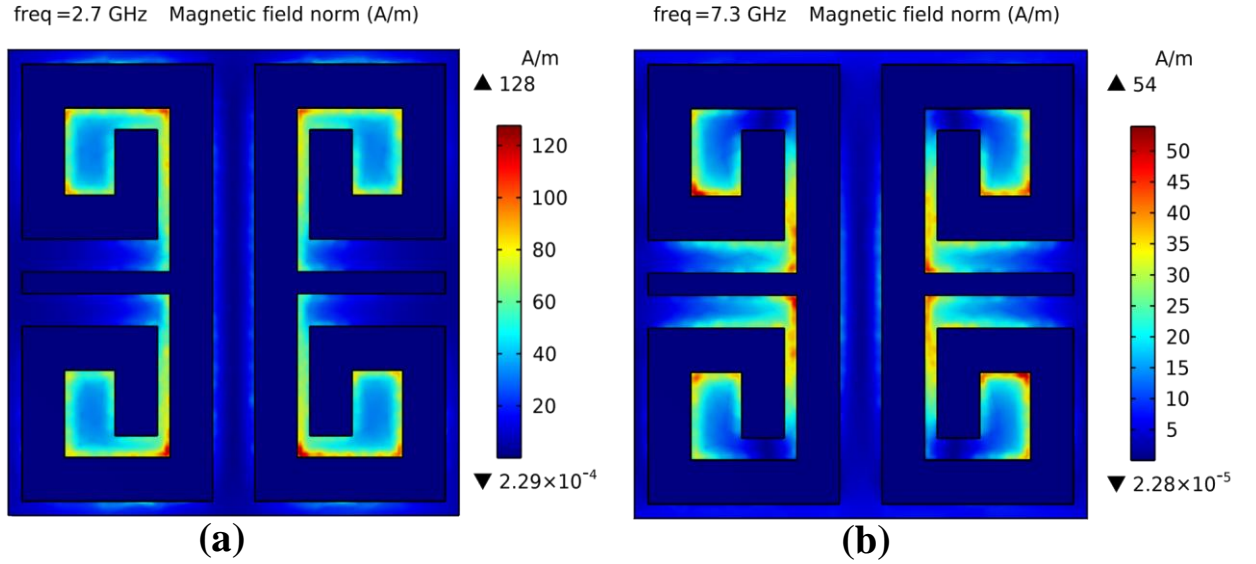
Figure 5.7 The Magnetic field distribution corresponding to resonance frequency at **(a)** 2.7 GHz and **(b)** at 7.3 GHz.

Figure 5.8 (a) and (b) depict the electric field distribution, highlighting the influence of changes in the magnetic field on the induced electric field. Areas with the most rapid rate of change in the magnetic field exhibit intense electric fields, as evident in the comparison between Figure 5.8 (a) and Figure 5.7 (a). The capacitive effect results in strong electric fields near the gap in the MTM structure. Consequently, at 2.7 GHz, the outer and middle horizontal edges display stronger electric fields compared to other areas. Conversely, in Figure 5.8 (b), at 7.3 GHz, a lower electric field intensity is observed due to reduced electric current and magnetic field intensity. Moreover, the electric field neutralizes when the magnetic field remains constant in the resonator. Both electromagnetic fields and currents are interconnected, playing pivotal roles in the resonances at the mentioned frequencies. In Figure 5.8 (c) and (d), the field distribution of the x-component of the Electric field (E_x) is presented, indicating the formation of electric quadrupole mode resonance at the metal-dielectric interface. The resonance of the proposed structure primarily stems from the excitation of Surface Plasmon Polaritons (SPP) due to electric quadrupole mode resonance. This resonance is illustrated by the field distribution, which also demonstrates the accumulation of positive and negative charges in the gap region of the resonator structure [58,120–122].
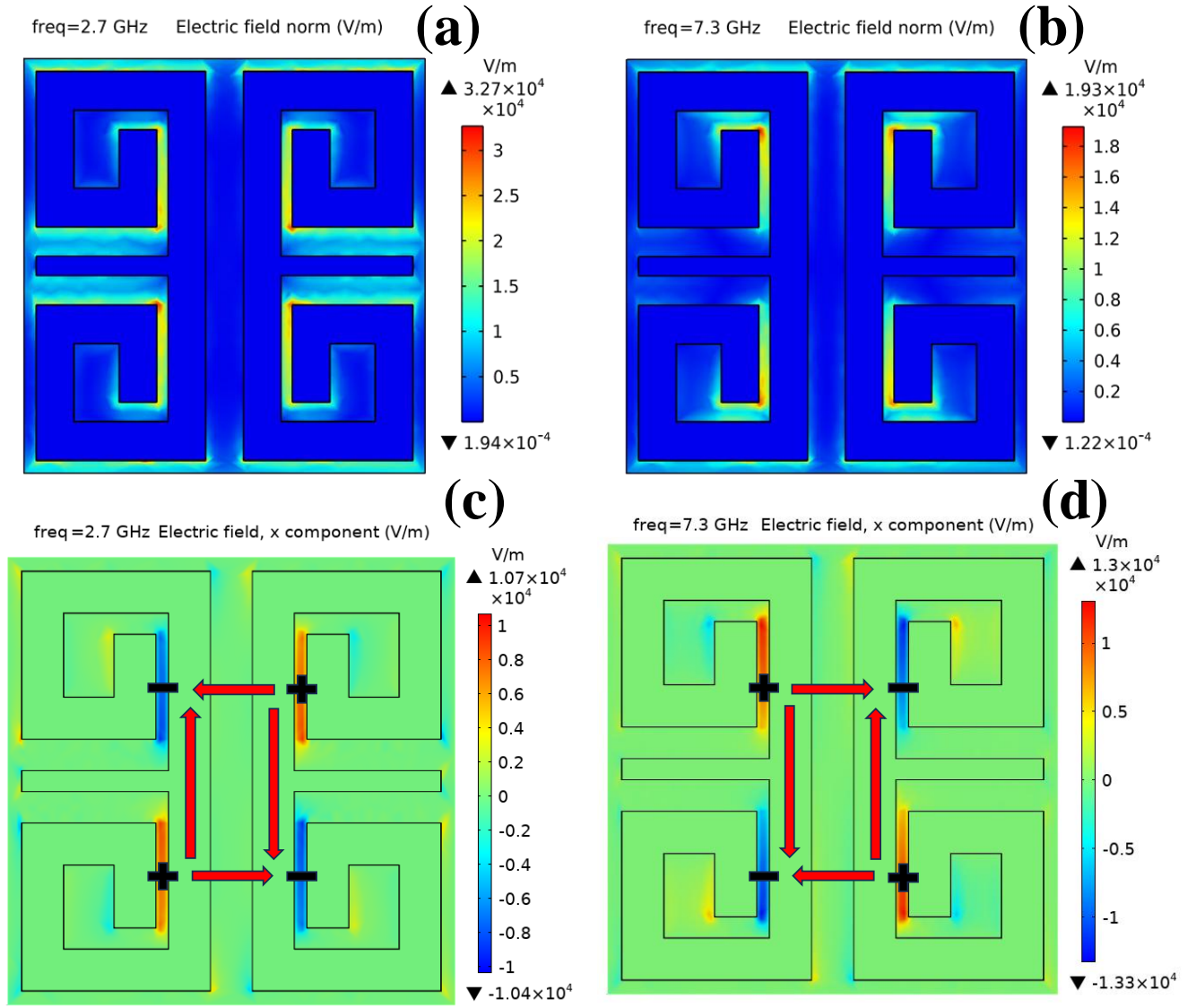
Figure 5.8 The Electric field distribution corresponding to resonance frequency at **(a)** 2.7 GHz and **(b)** at 7.3 GHz. Electric field x-component showing electric quadrupole mode resonance at **(c)** 2.7 GHz and **(d)** 7.3 GHz.
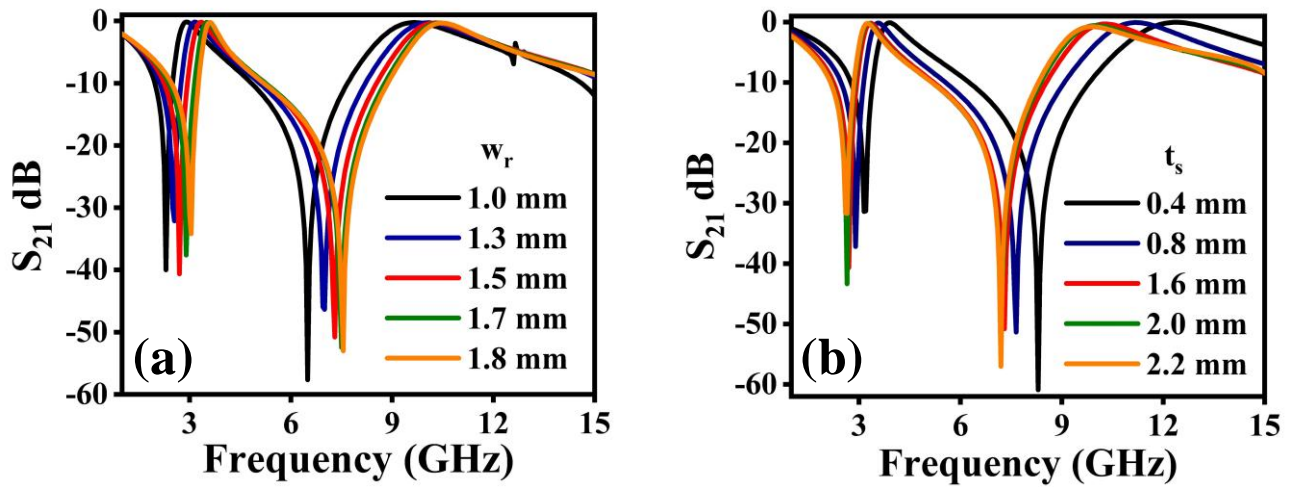
Figure 5.9 The response of scattering parameters (S_{21}) relating to **(a)** different resonator widths (w_r) and **(b)** different substrate thicknesses (t_s)

5.2.3 Effect of resonator width (w_r) on resonance frequency

Figure 5.9 (a) illustrates the relationship between the scattering parameter (S_{21}) and the width of the resonator (w_r). Modifying the width affects the inductance, thereby resulting in changes in the resonance frequency of the proposed MTM structure [69,117]. It's noteworthy that there is a significant blue shift in the S_{21} parameter as the w_r is increased from 1 mm to 1.8 mm, causing an increase in inductance, which indicates a rise in resonance frequency. This observed shift in resonance frequencies also imparts tunability characteristics to the designed MTM structure.

5.2.4 The impact of varying the thickness (t_s) of the FR-4 dielectric substrate

Figure 5.9 (b) demonstrates the impact of varying the substrate FR-4 thickness (t_s) from 0.4 to 2.2 mm on the scattering parameter (S_{21}). The substrate thickness has a relatively minor effect on the resonance frequency, particularly noticeable at lower values within the S-band. However, at higher values, especially in the C-band, the shift in resonance frequency becomes more pronounced with increasing thickness of the FR-4 substrate. This phenomenon occurs because the substrate acts as a dielectric medium, resulting in the creation of capacitance between the two waveguide ports. As the substrate thickness increases, the parallel capacitance also increases, leading to a decrease in the resonance frequency [69]. Figure 5.9 (b) illustrates that the MTM unit cell achieves the required resonance frequencies in both the S and C bands when the substrate thickness is set at 1.6 mm. Hence, this variation of w_r and t_s demonstrates the tunability characteristics of the designed structure with the shift in resonance frequency.

5.2.5 Effect of different dielectric substrate material

The investigation delves into the impact of changing the dielectric substrate material on the performance of MTMs. When Rogers' versions are utilized instead of the FR-4 substrate, the frequency response of S_{21} shifts towards higher frequencies. This shift highlights the substantial

influence of substrate choice on MTM performance, as depicted in Figure 5.10. Each Rogers' version displays dual resonance frequencies in the S- and X-bands with varying magnitudes, excluding the C-band. Conversely, the FR-4 substrate demonstrates dual resonances at 2.7 GHz and 7.3 GHz in the S and C bands, with magnitudes of -40.6 dB and -50.7 dB, respectively. The discussion emphasizes the significance of the FR-4 dielectric material as a suitable substrate for the proposed MTM structure. These findings are concisely summarized in Table 5.4.
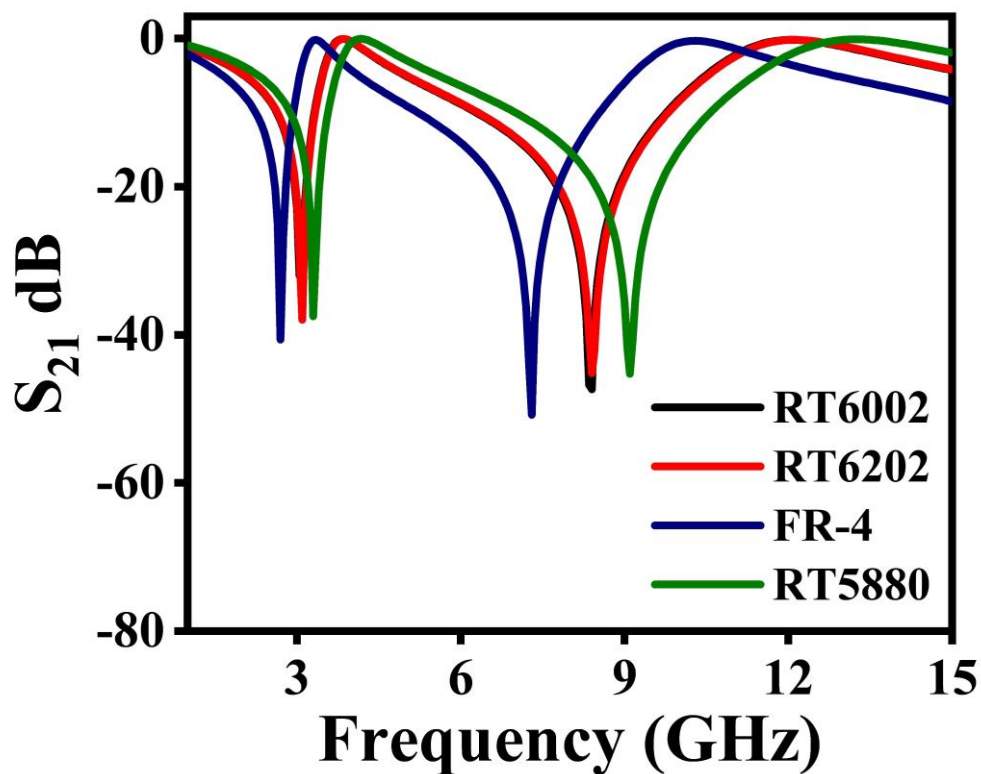
Figure 5.10 The variation of scattering parameters (S_{21}) with different materials as substrates

Table 5.4 Various properties and S21 parameters result of different substrate materials.

S. No.	Substrate	Electric Permittivity	Tangent Loss	Resonance Frequency of S_{21} (GHz)	Frequency Band	Magnitude of S_{21} (db)
1.	Roger's RT6002	2.94	0.0012	3.1 and 8.4	S and X	-31.9 and -47.3
2.	Roger's RT6202	2.90	0.0015	3.1 and 8.4	S and X	-37.9 and -45.1
3.	Roger's RT5880	2.20	0.0009	3.3 and 9.1	S and X	-37.4 and -45.2
4.	FR-4	4.30	0.025	2.7 and 7.3	S and C	-40.6 and -50.7

5.2.6 MTM as refractive index sensor

In the subsequent section, the investigation focuses on examining the variation of the transmission coefficient (S_{21}) concerning different refractive index (RI) values to assess RI sensitivity. The analysis of RI sensing properties entails modifying the surrounding environment of the MTM to match changes in its refractive index, thereby causing a shift in the resonance frequency of the proposed MTM, as depicted in Figure 5.11 (b). Sensitivity (S_R) plays a pivotal role as a key metric for evaluating sensing performance and is defined as follows [113]:

$$S_R = \frac{\Delta f}{\Delta n} \qquad\qquad 5.1$$
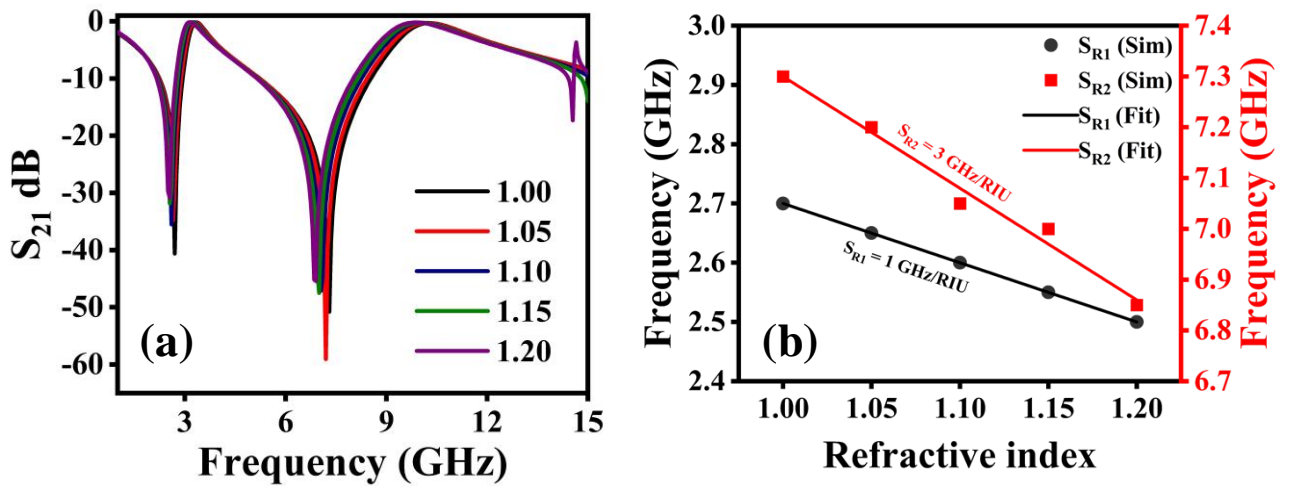
Figure 5.11 (a) Transmission coefficient (S_{21}) spectra of the proposed MTM sensor using different RI values of the surrounding environment. **(b)** The variation of simulated resonance frequency (square and circle symbols) and linear fitting (solid line) with different RI values of the surrounding environment.

The transmission coefficient spectra demonstrate a red shift as the refractive index of the surrounding environment varies from 1.00 to 1.20, as depicted in Figure 5.11 (a). Figure 5.11 (b) showcases the relationship between the shift in resonance frequency (Δf) and the changes in refractive index (Δn) of the surrounding environment. Furthermore, the resonance frequency of the proposed MTM exhibits a linear decrease with the increase in the refractive index of the surrounding environment. It is further elucidated that the sensitivities S_{R1} and S_{R2}, corresponding to the first and second resonance peaks in the S and C bands, are approximately 1 GHz/RIU and 3 GHz/RIU, respectively. These sensitivities surpass those of previously reported MTM sensors, as documented in Table 5.5. Hence,

it can be inferred that the proposed MTM sensor demonstrates high refractive index sensitivity in the GHz band.

Table 5.5 Comparison of sensitivity of the proposed MTM structure with the previous literature work.

Reference	Designed structure	Frequency band	Sensitivity
[123]	SRR	Single band (C band)	$S_R = 1.69\ GHz/RIU$
[113]	Frequency selective surface (FSS)	Single band (X band)	$S_R = 1.31\ GHz/RIU$
[114]	Periodical circle rings resonator	Single band (C band)	$S_R = 0.3537\ GHz/RIU$
[115]	Microwave resonator	Dual band (C and X bands)	$S_{R_1} = 1.116\ GHz/RIU$ $S_{R_2} = 2.357\ GHz/RIU$
[124]	corona-shaped metamaterial resonator	Single band (S band)	$S_R = 0.1825\ GHz/RIU$
THIS WORK	**Metamaterial Structure**	**Dual band (S and C bands)**	$\boldsymbol{S_{R_1} = 1\ GHz/RIU}$ $\boldsymbol{S_{R_2} = 3\ GHz/RIU}$

5.3 SUMMARY

This chapter introduces a novel design, fabrication, and simulation of a MTM structure capable of dual-band operation with wide bandwidth in the C band and its application in refractive index sensing. The experimental measurements are compared to the simulated results and found to be well-aligned. The study further explores the effective medium parameters of the designed MTM structure within the frequency range of 1-15 GHz. Analysis of the proposed mirror-shaped metamaterial reveals effective negative and NZI and effective negative and ENZ for dual-band operations. Electromagnetic field distributions are plotted at resonance frequencies. Leveraging the suggested MTM as a refractive index sensor exhibits significant sensitivity potential, specifically 1 GHz/RIU and 3 GHz/RIU. This research introduces a promising alternative approach for developing advanced multi-function sensors with exceptional sensing capabilities, suitable for applications in medical diagnostics, detection, and biochemical sensing.

CHAPTER- 6

CHAPTER 6: WIDE BANDWIDTH METAMATERIAL FOR WIRELESS APPLICATION

6.1 INTRODUCTION

In the previous chapter, a novel metamaterial structure was designed and fabricated in microwave region for refractive index sensing application with quad band plasmon resonance. This chapter focuses on designing a similar metamaterial structure, with modified dimensions, to expand its use in enhance wireless communications within the microwave band, achieving a broad bandwidth. The exploration of MTM research into GHz and THz frequencies has revealed unique properties such as negative μ, negative ε, and negative η, leading to a diverse range of applications in microwave and optical domains. These applications include reconfigurable antenna [125], satellite [126], invisibility cloaking [127], filters [128], and superlenses [129], etc. MTMs have become increasingly utilized across various frequency bands due to their specific applications. For example, the microwave spectrum encompasses bands like L, S, C, X, and Ku, each with its distinct applications such as RADAR, Wi-Fi, satellite communication, etc.

Improvements in EMR govern the compactness and miniaturization of MTMs, a crucial aspect of MTM research. Various MTM structures have been proposed to enhance EMR and functionality within specific frequency bands [130–133]. However, previous designs have often been limited to single or narrow band operations and have exhibited modest EMR values. Therefore, there is a pressing need for advanced MTM structures catering to triple-band operations with wide bandwidth in the C-band and higher EMR values.

In this chapter, a novel MTM structure tailored for triple-band operation with wide bandwidth in the C-band, catering to wireless applications has been introduced. The study involves investigating the scattering parameters of the MTM unit cell using simulation software and optimizing the structure through parametric analysis. By varying parameters such as resonator width (w_r), gap width (r),

substrate thickness (t_s), and effects of dielectric materials and the influence of different metal conductors, the MTM structure achieves triple-band operation with improved EMR values. Electromagnetic field analysis and surface current distribution provide insights into the MTM phenomena. Notably, the designed MTM structure achieves a high EMR value of up to 13.37, affirming its compactness. It is anticipated that the findings of this research, including the design process, compact size, multi-band resonance, wide bandwidth in the C-band, and high EMR, will significantly contribute to enhancing the efficiency and compactness of wireless communication devices and components in the future.

6.2 DESIGN AND SIMULATION GEOMETRY OF AN MTM STRUCTURE

(a)   **(b)**
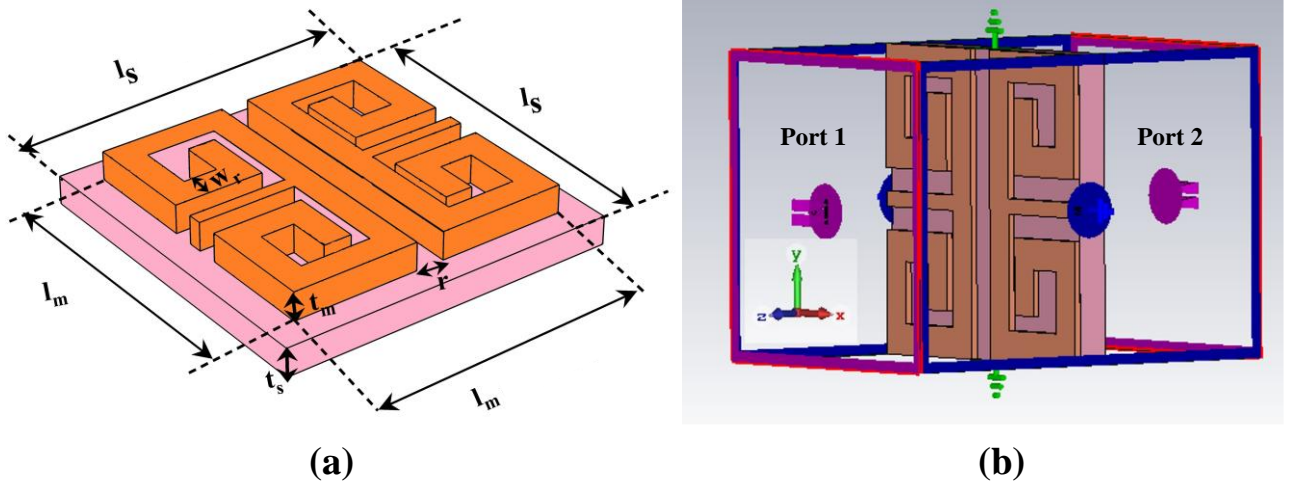
Figure 6.1 (a) Designed MTM unit cell structure with geometrical parameters and **(b)** simulation setup for reflection coefficient (S_{11}) and transmission coefficient (S_{21}) measurement.

The proposed MTM unit cell is formed on an FR-4 epoxy resin fiber substrate with dimensions of 1.6 cm × 1.6 cm × 0.16 cm. The research operates within a frequency range of 0.1-16 GHz. The FR-4 dielectric material has a permittivity of 4.3 and a dielectric loss tangent (δ) of 0.025 [69,107]. Copper (Cu) is used to construct the resonating patch on the FR-4 substrate, with a thickness (t_m) of 0.035 cm and a conductivity (σ) of 5.99×10^7 S/m [69]. The schematic depiction of the MTM unit cell is provided in Figure 6.1 where Figure 6.1 (a) illustrates the perspective view of the MTM unit

cell, and Figure 6.1 (b) shows the setup including input and output ports for measuring the scattering parameters of the MTM.

The design and simulation analysis of the proposed MTM structure are conducted using the frequency-domain solver of COMSOL Multiphysics. PMC and PEC boundary conditions are enforced for the MTM unit cell along the x-axis and y-axis. Two waveguide ports are introduced from both the front and back sides of the MTM along the positive and negative z-axis, respectively, with the electric field component oriented along the y-axis, as depicted in Figure 6.1 (b).

6.3 OPTIMIZATION OF THE PROPOSED MTM UNIT CELL

6.3.1 Design Methodology
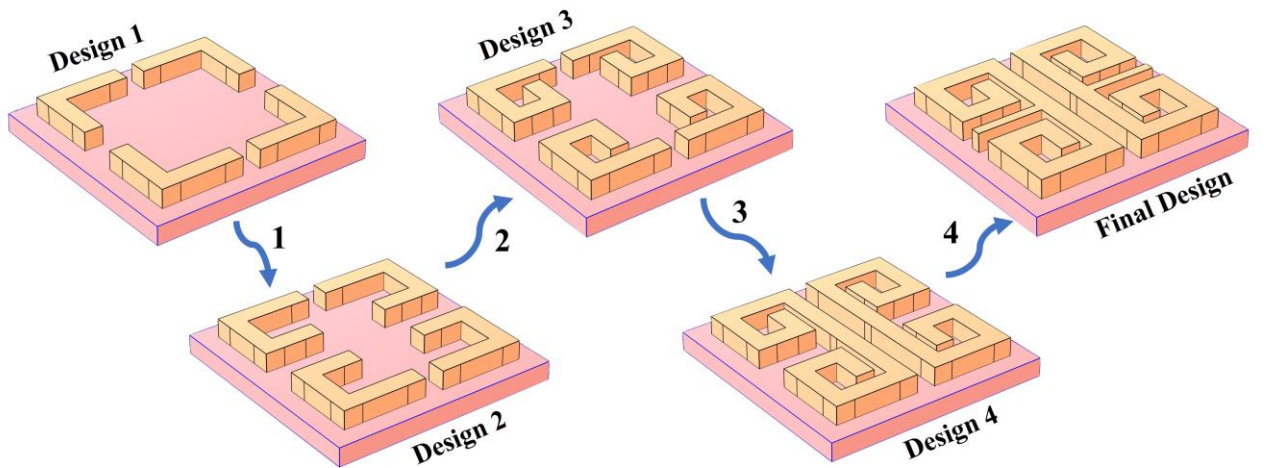
Figure 6.2 Design methodology of the proposed MTM structure

The design optimization process for the proposed MTM structure involves five sequential steps, outlined in Figure 6.2. Design 1 is achieved by integrating four outer L-shaped metallic strips positioned at the corners of the substrate. This configuration resonates at 8.5 GHz, as depicted in Figure 6.3 (b). Design 2 involves connecting four horizontal metallic wires along the middle edge, resulting in a resonance frequency of 5.8 GHz. In Design 3, four additional vertical metallic strips are added to Design 2, leading to two resonance frequencies (approximately 5 GHz and 14.8 GHz) within the desired microwave operating range. Design 4 is obtained by adding two more vertical metallic strips to the upper end of Design 3, resonating at 5 GHz and 14.7 GHz. Finally, Design 5

incorporates two horizontal strips in the middle of Design 4, resulting in a quad 'e'-shaped proposed MTM structure exhibiting triple-band resonance frequencies at 1.4 GHz, 5.0 GHz, and 14.8 GHz in the microwave region, as illustrated in Figure 6.3 (b).
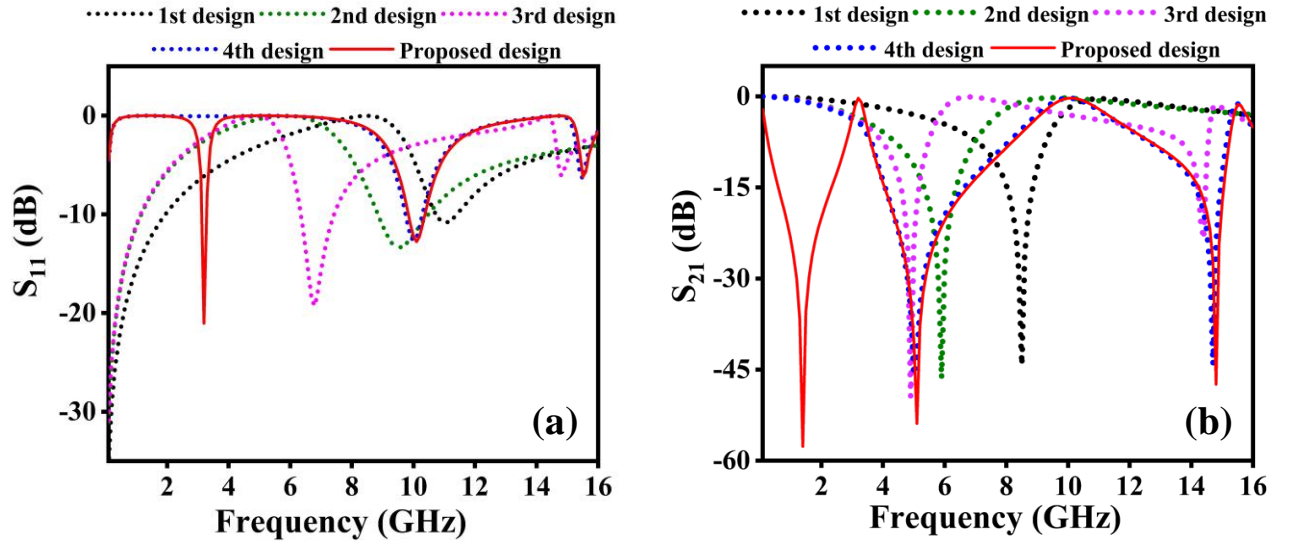
Figure 6.3 Response of scattering parameters **(a)** S_{11} (reflection coefficient) and **(b)** S_{21} (transmission coeficient) w.r.t incident electromagnetic plane wave frequency on different MTM structure.

6.3.2 Effect of middle gap width (r) and resonator width (w_r) on resonance frequency

Variations in the middle gap between the two symmetrical mirror shapes have a notable impact on the resonance frequency of the proposed MTM structure. In this study, the middle gap (r) was adjusted in increments of 0.01 cm, as depicted in Figure 6.4 (a)-(b). This gap influences the capacitance value, which in turn affects the resonance frequency [69,107,134]. As the gap 'r' decreases from 0.159 to 0.149 cm, the capacitance value increases, leading to a decrease in resonance frequency in both bands, resulting in a blue shift. Further reduction of the middle gap to 0.139 cm decreases the resonance frequency due to increased capacitance between the gaps. At r = 0.139 cm, three resonance frequencies were observed in the scattering parameter S_{21} plot, as illustrated in Figure 6.4 (b). The impact of resonator width (w_r) variation on scattering parameters is also investigated and presented in Figure 6.4 (c)-(d). Alterations in width affect the inductance value, thereby influencing the resonance frequency of the proposed MTM structure [69,134]. A noticeable red shift is observed in both S_{11} and S_{21} parameters with a step size of 0.02 cm as the resonator width (w_r) changes. As the width increases from 0.119 to 0.139 cm, the inductance value rises, shifting the

resonance frequency higher. Similarly, further widening from 0.139 to 0.159 cm increases the resonance frequency due to a corresponding increase in inductance value. For the proposed MTM structure, middle gap width (r) and resonator width (w_r) values of 0.139 cm and 0.159 cm, respectively, are chosen based on the appropriate resonance frequency band of the S_{21} parameter for Wi-Fi applications.
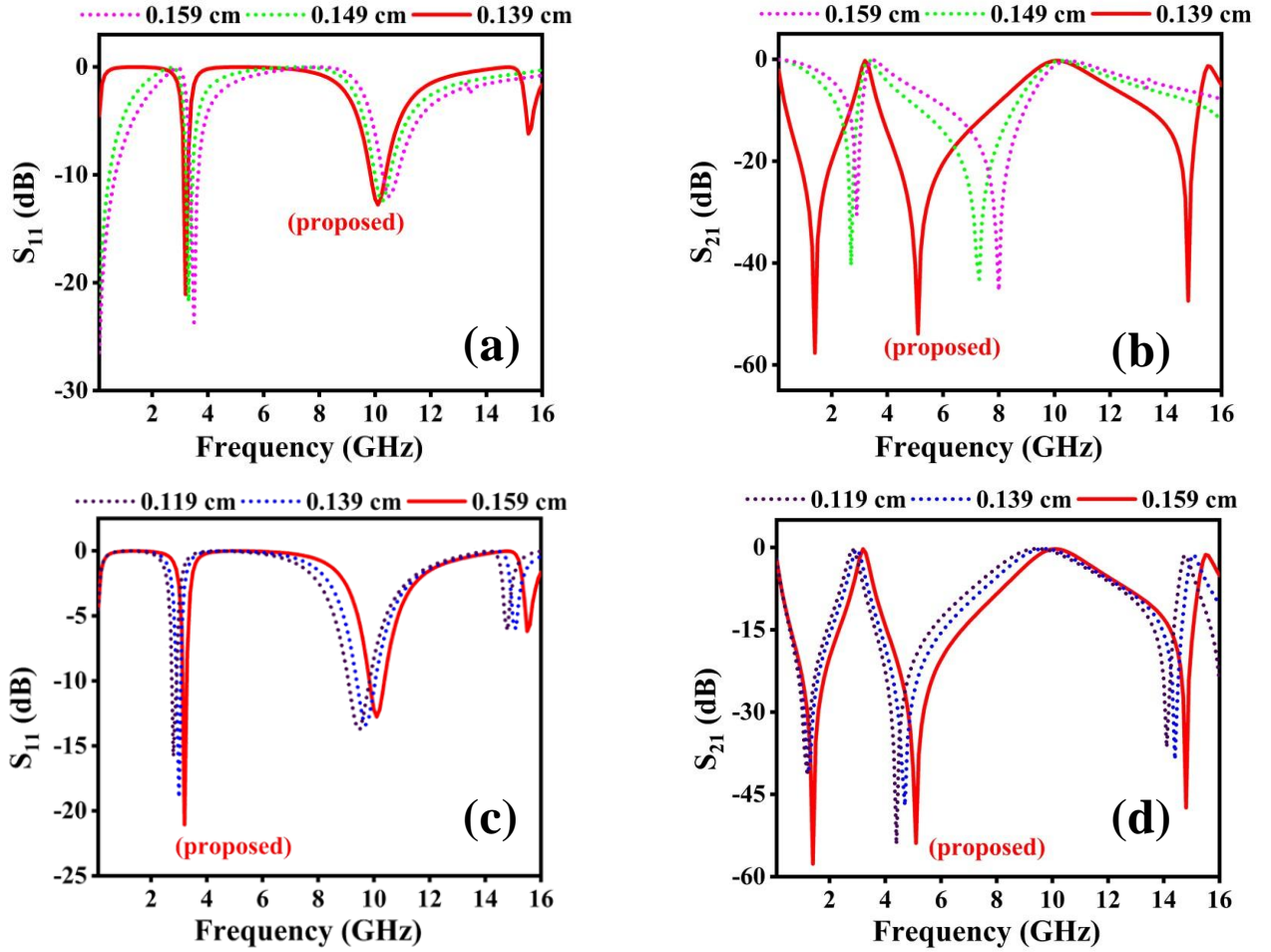
Figure 6.4 Scattering parameters response **(a)** S_{11} & **(b)** S_{21} with the different middle gap width (r) and **(c)** S_{11} & **(d)** S_{21} with the different resonator widths (w_r)

6.3.3 Effect of thickness (t_s) of FR-4 substrate

The impact of varying substrate FR-4 thickness (t_s) from 0.06 to 0.36 cm on scattering parameters is examined, as depicted in Figure 6.5 (a). While substrate thickness has a limited effect on resonance frequency, it becomes more noticeable at higher frequency bands (C and Ku bands) compared to lower frequency bands (L band). This effect is due to the substrate acting as a dielectric medium, creating capacitance between the two waveguide ports. As t_s increases, parallel capacitance also

increases, leading to a decrease in resonance frequency [69]. A substrate thickness of 0.16 cm is found to provide the necessary resonance frequencies in L, C, and Ku bands for satellite and Wi-Fi applications, as illustrated in Figure 6.5 (a).
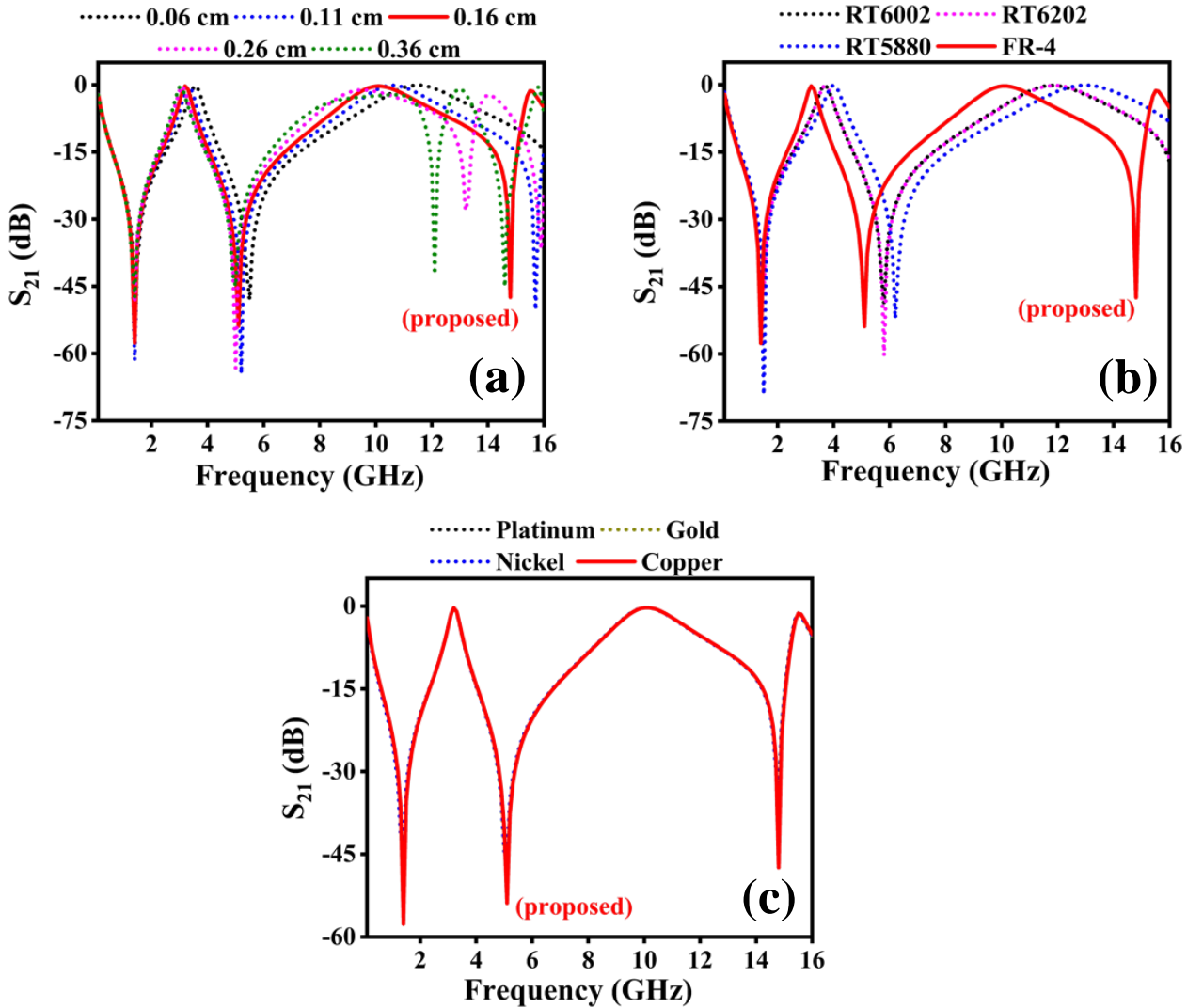
Figure 6.5 Variation of transmission coefficient (S_{21}) with the change in **(a)** substrate thickness (t_s), **(b)** different dielectric material and **(c)** different types of a metallic conductors of the designed MTM structure.

6.3.4 Effect of different dielectric substrate material

The study also examines the effect of using different dielectric substrate materials on MTM performance. Figure 6.5 (b) illustrates that the frequency response of S_{21} shifts towards higher frequencies when using Rogers' versions instead of the FR-4 substrate, indicating the dependency of MTM performance on substrate selection. Three versions of Rogers' materials (RT 6002, RT 6202, and RT 5880) along with FR-4 are considered as different dielectric substrate materials. While all Rogers versions exhibit dual resonance frequencies in L and C bands with varying magnitudes, the

FR-4 substrate reveals triple resonances at 1.4 GHz, 5.0 GHz, and 14.8 GHz in L, C, and Ku bands, respectively, with magnitudes of -57.0 dB, -53.8 dB, and -47.4 dB. As a 5 GHz resonance frequency is crucial for Wi-Fi applications, it is achieved with the MTM using an FR-4 substrate. Therefore, the choice of FR-4 dielectric material as a substrate for the proposed MTM structure is justified based on these observations. The summarized findings are presented in Table 6.1.

Table 6.1 Various properties and S_{21} parameters result of different substrate materials.

Sr. No.	Substrate	Electric Permittivity	Tangent Loss	Resonance Frequency of S_{21} (GHz)	Frequency Band	Magnitude of S_{21} (dB)
1.	Roger's RT6002	2.94	0.0012	1.5, 5.8	L, C	-45.0, -48.8
2.	Roger's RT6202	2.90	0.0015	1.5, 5.8	L, C	-45.59, -60.34
3.	Roger's RT5880	2.20	0.0009	1.5, 6.2	L, C	-69.07, -52.04
4.	FR-4	4.30	0.025	1.4, 5.0, 14.8	L, C, Ku	-57.0, -53.8, -47.4

6.3.5 Effect of different metal conductors on resonance frequency

In Figure 6.5 (c), the impact of different metal conductors including copper (Cu), nickel (Ni), gold (Au), and platinum (Pt) on the resonance frequency is illustrated. Despite all metals exhibiting the same triple resonance frequencies, copper stands out with a higher magnitude of the S_{21} parameter, lower resistivity, and more cost-effectiveness compared to other metals. These characteristics make copper a favorable choice for the resonating patch in the proposed MTM structure. Table 6.2 outlines the geometric parameters of the optimized MTM unit cell.

Table 6.2 Dimension of proposed MTM Unit cell

Parameters	Values (cm)	Description
l_s	1.600	length of substrate
l_m	1.599	length of the material
r	0.139	middle gap
w_r	0.159	width of resonator
t_s	0.160	thickness of substrate
t_m	0.035	thickness of metamaterial

6.4   RESULT AND DISCUSSION

6.4.1   Scattering parameters of optimized MTM unit cell
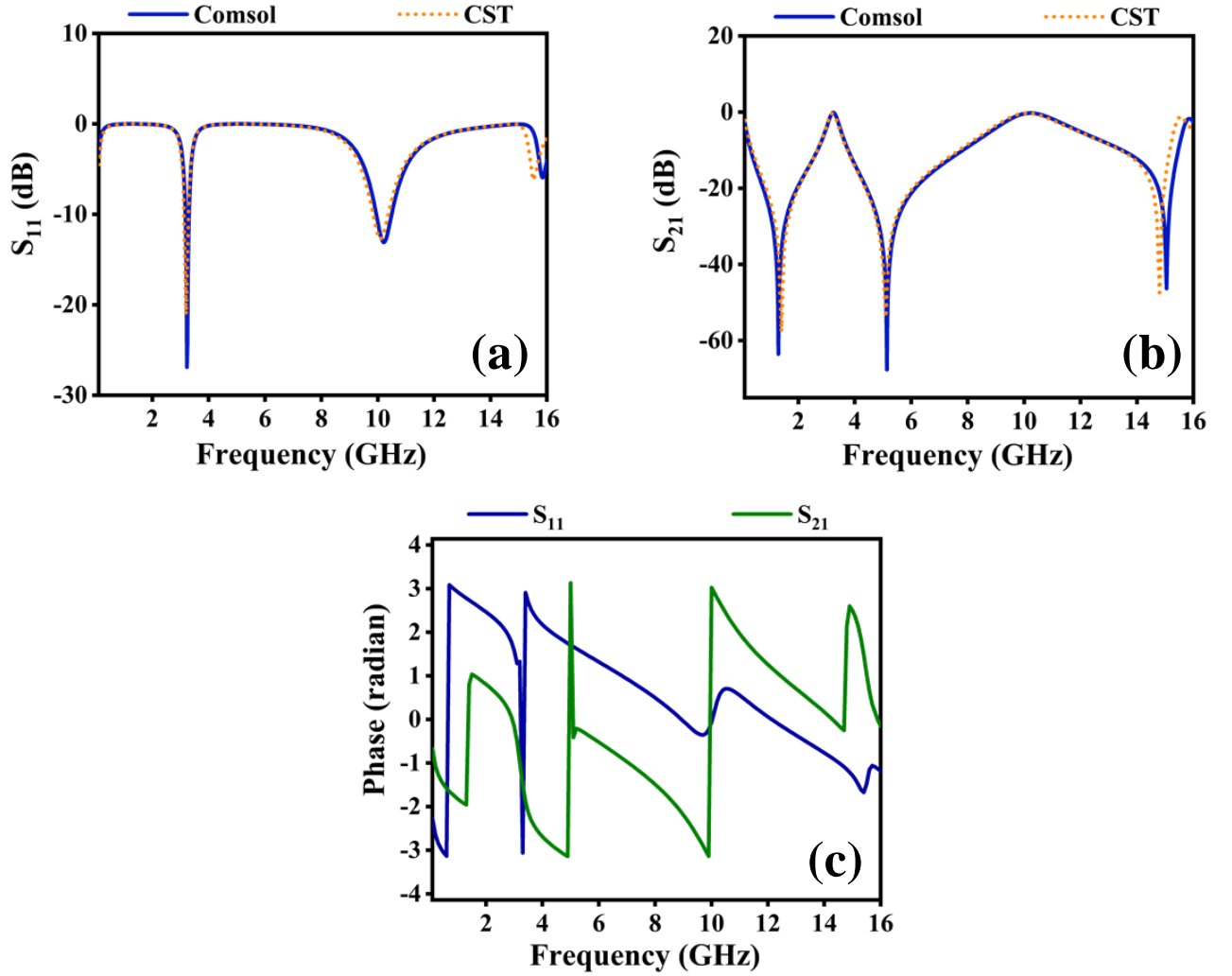
Figure 6.6 (a) Reflection coefficient (S_{11}), **(b)** transmission coefficient (S_{21}) comparison from two simulation software COMSOL and CST Microwave Studio, and **(c)** phase plot of scattering parameters with the incidence wave frequency of the unit cell of the structure with the COMSOL.

The scattering parameters (S_{11} and S_{21}) of the optimized MTM unit cell were assessed through simulations conducted using FEM-based COMSOL Multiphysics and CST Microwave Studio tools, as depicted in Figure 6.6 (a) and (b). Additionally, the phase plot of scattering parameters is presented in Figure 6.6 (c). According to Figure 6.6 (b), the S_{21} parameter of the proposed MTM unit cell exhibits triple resonance frequencies at 1.4, 5.0, and 14.8 GHz with magnitudes of -57.0, -53.8, and -47.4 dB, respectively, as observed using the COMSOL simulator. Conversely, applying the CST simulator yields similar resonance frequencies with magnitudes of -57.0, -53.9, and -47.7 dB,

respectively, as shown in Figure 6.6 (b). This consistency in scattering parameter values from both microwave simulation software validates the correctness of the designed structure and confirms the results of the proposed MTM structure.

These resonance frequency findings fall within the microwave region, specifically the L-band, C-band, and Ku-band, which span 1-2 GHz, 4-6 GHz, and 14-16 GHz, respectively. The phase plot of output scattering parameters (S_{11} and S_{21}) exhibits variation from $-\pi$ to $+\pi$ values (-3.14 to +3.14), indicating a total phase change of 2π, as illustrated in Figure 6.6 (c). The bandwidth of S_{21}, with magnitudes less than -17 dB, is observed as 1.49 GHz (0.70-2.19 GHz), 2.22 GHz (4.20-6.42 GHz), and 0.58 GHz (14.41-14.99 GHz) using the COMSOL simulator, while the CST simulator yields 1.54 GHz (0.70-2.25 GHz), 2.27 GHz (4.16-6.44 GHz), and 0.61 GHz (14.38-15.00 GHz). Similarly, the reflection coefficient (S_{11}) outcomes reveal triple resonance frequencies at 3.2, 10.2, and 15.8 GHz with magnitudes of -21.06, -13.08, and -5.87 dB, respectively, using the COMSOL simulator. Correspondingly, the CST simulator demonstrates similar resonance frequencies with magnitudes of -21.06, -12.76, and -6.18 dB, respectively, as shown in Figure 6.6 (a).

Each resonance frequency of S_{11} aligns with the resonance frequency of S_{21}, with S_{11} frequencies following those of S_{21}, as depicted in Figure 6.6 (a) and (b) from both the COMSOL and CST simulations. These findings affirm that the proposed MTM unit cell's bandwidth is consistent across both simulators. In wireless communications, bandwidth is a crucial factor. For satellite and Wi-Fi applications, the proposed MTM design offers sufficient bandwidth [69]. Notably, the proposed MTM unit cell's bandwidth for the C-band exceeds previously published data, as shown in Table 6.3.

Figure 6.7 (a) and (b) reveal that the effective permeability ($\mu_{eff.}$) is negative at the resonance frequency of 1.4 GHz, whereas the effective permittivity ($\varepsilon_{eff.}$) is negative at the resonance frequency of 14.8 GHz for the proposed MTM structure. Negative values of effective refractive index ($\eta_{eff.}$) are observed at resonance frequencies of 1.4, 5.0, and 14.8 GHz, which correspond to the L, C, and Ku bands, as depicted in Figure 6.7 (c). Throughout the frequency range, the normalized impedance exhibits positive and real values; however, at resonance frequencies (1.4, 5.0, and

14.8 GHz), it approaches zero, with values of $0.045 \times 10^{-3}, 0.118 \times 10^{-3},$ and 0.615×10^{-3}, respectively, as shown in Figure 6.7 (d). These relatively small values of normalized impedance at resonance frequencies indicate the passive behavior of the proposed MTM unit cell.
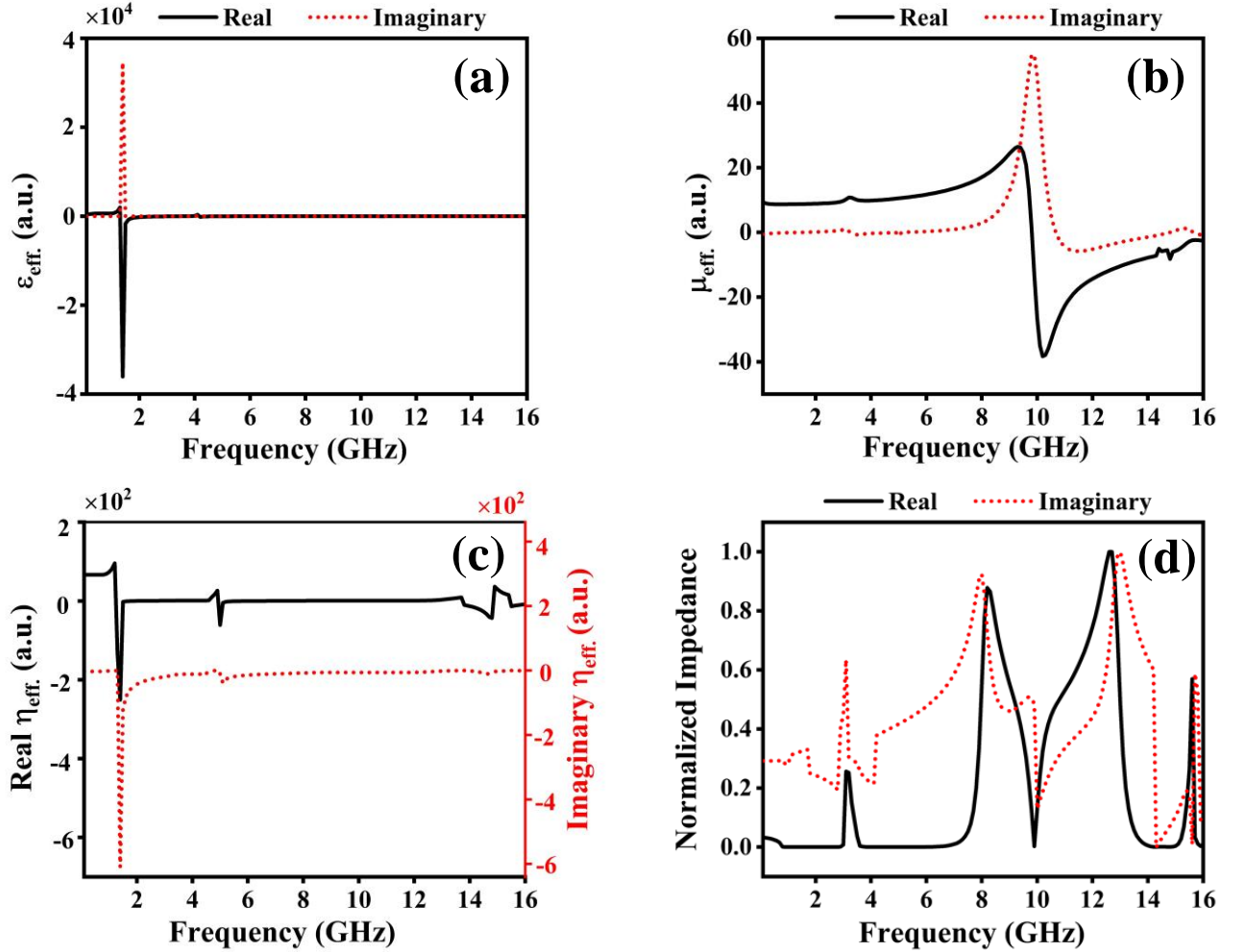
Figure 6.7 Variation of **(a)** effective permeability ($\mu_{eff.}$), **(b)** effective permittivity ($\varepsilon_{eff.}$), **(c)** effective refractive index ($\eta_{eff.}$) and **(d)** normalized impedance (Z) with the frequency of the designed MTM unit cell

6.4.2 Metamaterial application and comparison study

The triple-band resonance frequencies offered by the proposed MTM unit cell at 1.4, 5.0, and 14.8 GHz cover a wide range of applications including radar, satellite, and Wi-Fi. Wi-Fi networks typically operate in both the 2.4 and 5 GHz frequency bands, with the latter being faster and less congested. With a bandwidth of 2.22 GHz at the 5 GHz frequency band, the proposed MTM structure is well-suited for Wi-Fi networks. Additionally, the resonance frequencies at 1.4 GHz (L band) and 14.8 GHz (K band) can be utilized in satellite applications, weather radar systems, and terrestrial microwave communications due to their respective wide bandwidths of 1.49 GHz and 0.58 GHz.

Moreover, the MTM structure offers versatility across microwave devices in the L, C, and Ku bands, making it suitable for radar and satellite applications, as well as for devices such as antennas, bandpass filters, power dividers, and couplers.

Table 6.3 Comparison of different Bandwidth of proposed work with the already published work.

References	Dimension (physical and electrical)	Resonance Frequencies (GHz)	Frequency band	Effective Bandwidth (GHz)
[135]	9×9 mm^2 (0.087λ×0.087λ)	2.896, 8.11, 9.76, 12.48, 13.49	S, X, Ku	0.3, 0.54, 0.59, 0.24, 0.35
[117]	10×10 mm^2 (0.14λ×0.14λ)	4.20, 10.14, 13.15, 17.1	C, X, Ku	0.72, 1.55, 0.17, 0.24
[116]	8×8 mm^2 (0.070λ×0.070λ)	2.61, 6.32, 9.29	S, C, X	0.11, 0.79, 0.15
[107]	8×8 mm^2 (0.06λ×0.06λ)	2.48, 4.28, 9.36, 13.7	C, S, X, Ku	0.19, 0.4, 1.3, 0.6
[136]	8×8 mm^2 (0.076λ×0.076λ)	2.86, 5.0, 8.30	S, C, X	0.11, 0.41, 0.37
[69]	10×10 mm^2 (0.17λ×0.17λ)	5.0, 6.88, 8.429	C, X	1.67, 0.52, 0.98
Present work	16×16 mm^2 (0.07λ×0.07λ)	1.4, 5.0, 14.8	L, C, Ku	1.49, **2.22**, 0.58

The performance of Wi-Fi and satellite antennas is significantly enhanced by this MTM structure. Comparison of the proposed MTM's performance with recently published works in Table 6.3 considers factors such as effective bandwidth at all resonance frequencies, the number of resonance frequencies covering bands, and physical and electrical unit cell parameters. Effective bandwidth is crucial for improved data transmission, with bandwidth determined where the value of S_{21} is less than -17 dB. Compared to other works listed in Table 6.3, the proposed MTM structure offers a greater bandwidth of 2.22 GHz for the C band. Therefore, the design of the proposed MTM unit cell surpasses all other designs provided in the comparison table for satellite and Wi-Fi applications, owing to its triple-band resonance with broader bandwidth in the C-band.

6.4.3 Analysis of Electromagnetic Fields and Surface current distribution

The MTM surface current distribution is depicted in Figure 6.8 (a)-(c). At 1.4 GHz, Figure 6.8 (a) illustrates a clockwise current flow in the right half and an anticlockwise current flow in the left half

of the proposed MTM structure. The current distribution appears uneven, with relatively high intensity observed in the inner vertical edges compared to the rest of the structure. At 5.0 GHz, shown in Figure 6.8 (b), there is a drastic decrease in current, particularly at the outer vertical edges of the metamaterial, while the remaining portion shows negligible current distribution. However, at the frequency of 14.8 GHz, depicted in Figure 6.8 (c), the surface current intensity, indicated by the color bar, increases compared to the 5.0 GHz frequency, with maximum current observed along the horizontal edges.
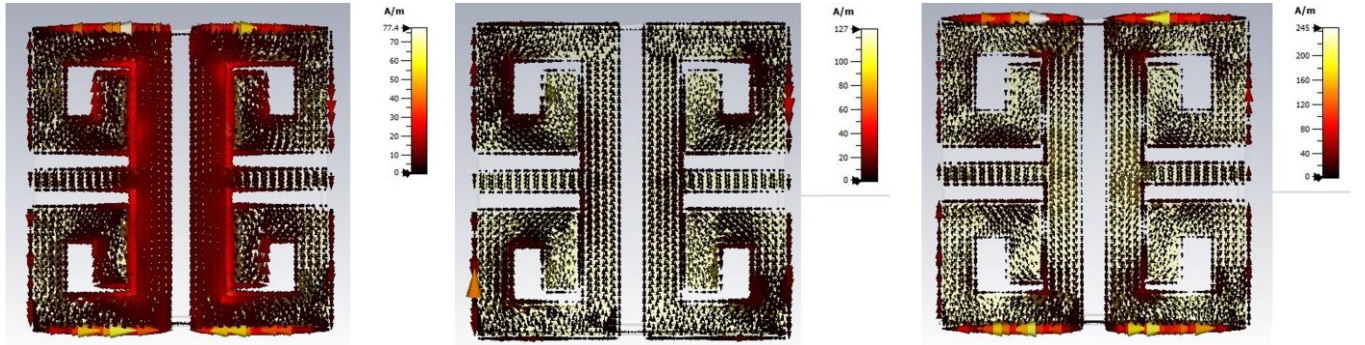
Figure 6.8 Surface current distribution at **(a)** 1.4 GHz, **(b)** 5.0 GHz, and **(c)** 14.8 GHz, respectively, of proposed MTM structure

The magnetic field distribution for the three resonance frequencies is shown in Figure 6.9 (a)-(c). Magnetic field and surface current density are correlated, as shown in equation (1.4). In Figure 6.9 (a), high magnetic field intensities are shown in those regions where a larger current density is observed; this satisfies Maxwell's equation represented by equation (1.4). Figure 6.9 (b) shows a low-intensity magnetic field owing to the low current intensity at this frequency. In contrast, Figure 6.9 (c), the outer horizontal edges exhibit significant magnetic field intensity due to knowledgeable current distribution. However, the field intensity is low in other parts of the MTM structure.
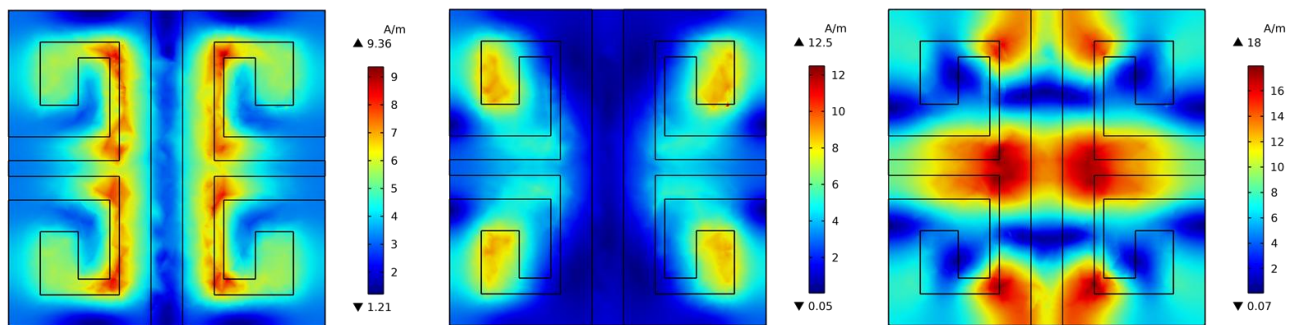
Figure 6.9 Magnetic field distribution at **(a)** 1.4 GHz, **(b)** 5.0 GHz, and **(c)** 14.8 GHz, respectively, of proposed MTM structure.
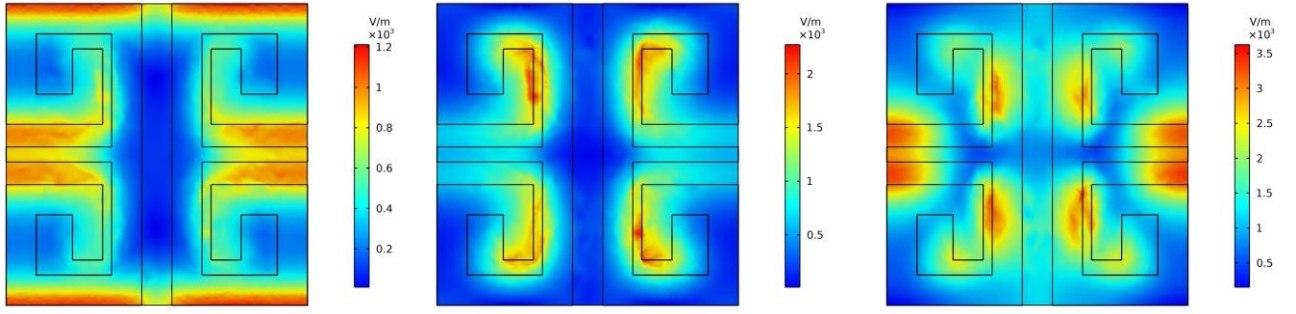
Figure 6.10 Electric field distribution at **(a)** 1.4 GHz, **(b)** 5.0 GHz, and **(c)** 14.8 GHz, respectively of proposed MTM structure.

Figure 6.10 (a)-(c) illustrates the electric field distribution. According to equation (1.3), variations in the magnetic field influence the induced electric field. Regions with the highest rate of change in the magnetic field exhibit intense electric fields, as evidenced by the comparison between Figure 6.10 (a) and Figure 6.9 (a). The capacitive effect leads to a strong electric field near the gap in the MTM structure. Consequently, at 1.4 GHz, the outer and middle horizontal edges display a stronger electric field compared to the rest of the structure. Conversely, in Figure 6.10 (b) at 5.0 GHz, a low electric field intensity is observed due to the reduced electric current resulting in lower magnetic field intensity. At 14.8 GHz, an intense field is evident at the middle horizontal edges and inner vertical edges, where the rate of magnetic field variation is high, as shown in Figure 6.10 (c). Additionally, the electric field becomes neutralized when the magnetic field remains constant in the resonator. The interconnected nature of electromagnetic fields and currents highlights their essential roles in the resonances at the specified frequencies.

In the proposed structure, the unit cell size is observed to be 1.6 cm, which is comparatively smaller than the operating wavelength for all three frequency bands. This observation confirms that the proposed structure satisfies the EMT condition, thereby exhibiting metamaterial characteristics.

The EMR is calculated using the formula given in equation (3.1). The EMR of the proposed MTM unit cell is compared with previously reported metamaterial designs, as presented in Table 6.4. These prior designs often suffer from limitations such as low EMR and functionality restricted to single or double microwave bands. In contrast, the proposed MTM unit cell demonstrates relatively high EMR, compact dimensions, and coverage of all three frequency bands (L, C, and Ku) used in satellite

and multi-band applications. The calculated EMR value for the designed metamaterial is 13.37 for the unit cell at the 1.4 GHz operating resonance frequency. This indicates an improvement in the compactness of the structure due to the relatively high EMR value.

Table 6.4 A comparison of the EMR of various metamaterial design

References	The shape of a unit cell	Dimension (cm^2)	Substrate	Bands	No. of Resonant frequency	EMR
[137]	Diamond shape	2.0 × 2.5	FR-4	-	-	1.2
[138]	Wedge- shaped	0.53 × 0.43	Taconic CER-10	-	-	6.9
[139]	Two rectangular U-shaped	2.0 × 2.5	Glass	-	-	1.99
[87]	Split H- shaped	2.0 × 2.0	FR-4	S, C, X, Ku	4	4.32
[140]	Modified SRR & CLS unit cell	0.5 × 0.32	FR-4	-	-	6.38
[141]	DBEM (Dual-band electric meta-atom)	0.75 × 0.75	Rogers RT	Dual bands	2	7.14
[131]	Double C- shaped	1.2 × 1.2	FR-4	S, C, X	3	7.44
[85]	CSRR	0.5 × 0.5	FR-4	C	2	8
[133]	Inverse double C- type	0.9 × 0.9	FR-4	S, C, X, K	5	12.34
Present Work	Proposed metamaterial	1.6 × 1.6	FR-4	L, C, Ku	3	13.37

6.5   SUMMARY

A MTM structure was designed for triple-band operation with wide bandwidth specifically targeting the C-band. Utilizing FEM-based COMSOL Multiphysics high-frequency electromagnetic simulator in the frequency domain, the design, simulation, and extraction of the MTM's S-parameters were conducted, with validation achieved through the CST Microwave Studio. Effective medium parameters of the proposed MTM structure were explored across the frequency range spanning 0.1 to 16 GHz. Investigation of the proposed Quad 'e' mirror-shaped metamaterial revealed a notably

effective negative refractive index suitable for multi-band operations. Further analysis employing surface current distribution and electromagnetic field characterization, including electric and magnetic field distributions, facilitated a comprehensive examination of the MTM phenomenon.

The proposed Quad 'e' mirror-shaped metamaterial demonstrates potential for enhancing emerging satellite communications and radar applications, attributable to its utilization of low-cost FR-4 substrate, multi-band resonance capabilities, high EMR, and wideband characteristics. With an EMR of 13.37, affirming the compactness of the structure, this metamaterial holds promise for applications across the microwave region, covering all three frequency bands. The aforementioned attributes and outcomes of the proposed MTM structure position it as a promising candidate for various applications, including electromagnetic cloaking, filter design, sensor and detector layouts, antennas, and Wi-Fi applications, offering enhanced features and performance.

CHAPTER- 7

CHAPTER 7: FAR-INFRARED METAMATERIAL PERFECT ABSORBER WITH SENSING APPLICATIONS

7.1 INTRODUCTION

The previous chapter discussed a designed of metamaterial structure for triple-band operation with wide bandwidth specifically targeting the C-band. In this chapter, the focus shifts to the design of a far-infrared metamaterial functioning as a perfect absorber, suitable for use as an IR sensor.

Metamaterial absorbers (MAs) in the microwave regime were initially proposed by Landy et al. in 2008 [142]. Since then, the field has progressed significantly, with numerous MAs featuring various microstructures being reported. This research has expanded the scope of metamaterial perfect absorbers (MPAs) across different frequency ranges, including visible light [143], infrared [144], and terahertz frequencies [58,145]. A significant research area within this field is the development of far-wavelength infrared (FWIR) MPAs, which are crucial for photothermal applications such as IR imaging [146] and sensing [147]. Continuous research efforts have accelerated the development of MPAs [148–150], resulting in their evolution from narrowband to broadband, polarization-sensitive to polarization-insensitive, and single-frequency to multi-frequency designs. MPAs now cover the entire spectral range, including microwave [151], terahertz [152], visible [153] and infrared frequencies [65,154]. To enhance efficiency and broaden the absorption bandwidth of FWIR MPAs, various strategies have been employed. Common methods for achieving broadband absorption include metal-insulator multilayer stacks [155]. Additionally, MPAs with coplanar multi-sized resonators have proven effective for broadband absorption. By utilizing multi-sized crosses [156], rings [157], multiple surface plasmon resonances (SPRs) with adjacent wavelengths can be excited, resulting in broadband absorption.

In recent years, numerous designs for metasurface perfect absorbers have been developed, employing a variety of materials. A notable example is a polarization-independent metasurface broadband

perfect absorber, which achieved a peak absorbance of 95% [158]. Additionally, a metasurface broadband solar absorber has been developed, offering absorbance exceeding 90% [159]. Narrowband metasurface perfect absorbers have shown effectiveness in detecting changes in the refractive index of the surrounding medium, prompting significant interest in innovative metasurface absorber designs for biomedical applications.

In this chapter, we propose an MPA designed for the far-infrared (IR) C-band. This MPA features a split-ring resonator (SRR) with an I-shaped copper top layer, a silicon dielectric base layer, and a copper bottom layer. The design achieved an absorption rate of 99.47% at a wavelength of $\lambda_r = 9.40$ μm, demonstrating a perfect absorption effect. The impact of altering the angle of incidence and structural characteristics on the absorption was also examined. Additionally, the refractive index of the surrounding environment was varied to assess the structure's sensing performance. Results indicated that the sensitivity could reach as high as 1600 nm/RIU. Furthermore, the device exhibited sensitivity to both transverse electric (TE) and transverse magnetic (TM) polarizations.

7.2   STRUCTURE DESIGN AND UNIT CELL MODEL
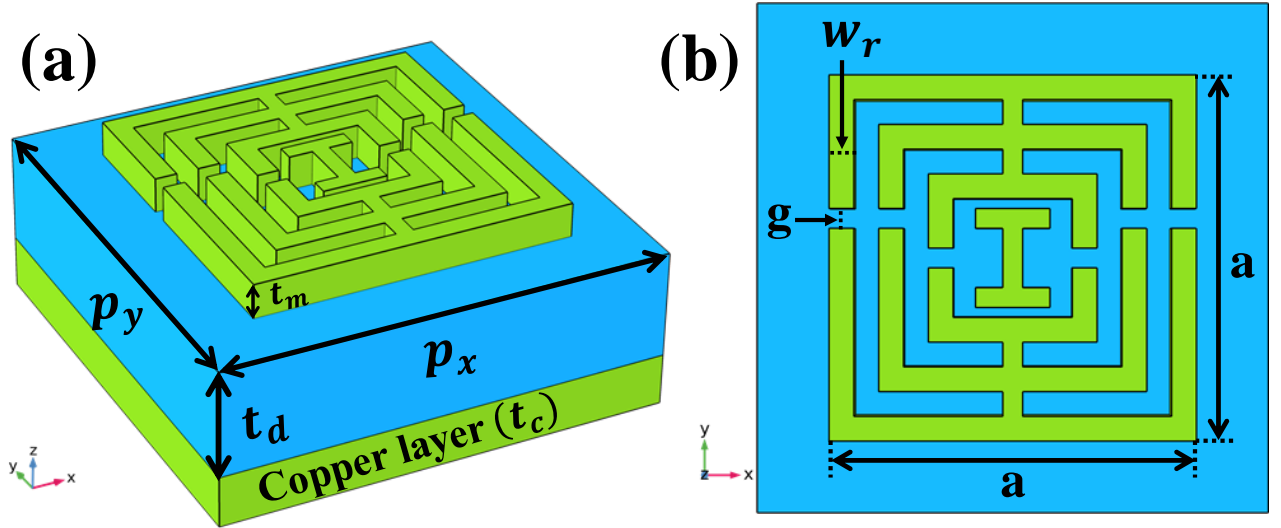
Figure 7.1 (a) 3D Side view and **(b)** top view of a metamaterial unit cell

Figure 7.1 illustrates a schematic diagram of the top and 3-D side view of a single metamaterial absorber (MA) unit cell. The unit cell comprises three unequal split ring resonators, each containing two split gaps (denoted by the letter "g"), and an I-shaped patch at the center. The absorber is

constructed with an upper copper resonant patch (depicted in green in Figure 7.1), a middle silicon

dielectric layer (shown in blue in Figure 7.1), and a bottom ground layer made of 0.1µm-thick copper

(denoted as t_c). The reflection coefficient (S$_{11}$) of the designed structure is calculated using a finite

element method (FEM) solver within COMSOL Multiphysics. Two periodic ports are employed for

wave propagation in both the positive and negative z-directions. The structure is analyzed under the

influence of transverse electric (TE) and transverse magnetic (TM) electromagnetic waves, incident

at an angle θ to the z-direction. For the TE wave, the electric field is oriented in the y-direction,

whereas for the TM wave, the magnetic field is aligned along the y-direction. The geometrical

parameters of the structure are detailed in Table 7.1. Periodic boundary conditions are applied in both

the x and y directions.

Table 7.1 Dimension of the unit cell

Parameters	Value (µm)	Description
p_x	2.60	period in x-axis
p_y	2.60	period in y-axis
t_d	0.27	thickness of dielectric layer
t_m	0.10	thickness of resonator patch
w_r	0.12	width of resonator
a	1.85	length and breadth of resonator
g	0.10	split gap between resonator

The bottom copper layer functions as a perfect mirror, with its thickness (t_c) defined by the skin

depth formula. The skin depth, Δ, is calculated as follows [160]:

$$\Delta = \sqrt{\frac{2}{\omega\mu\sigma}} = \sqrt{\frac{\lambda}{\pi c\mu\sigma}} \qquad 7.1$$

In this equation (7.1), Δ represents the penetration depth, λ is the operating wavelength, ω is the

angular frequency, and μ and σ denote the permeability and conductivity, respectively. The reflective

layer is designed to be much thicker than the calculated skin depth, ensuring that electromagnetic

waves are effectively blocked from penetrating the absorber.

7.3   RESULTS AND DISCUSSION

The absorption through the metamaterial structure is defined by $A = 1 - R - T$, where A is the absorption coefficient, R is the reflection coefficient, and T is the transmission coefficient. The transmission coefficient (T) is nearly zero because the metal ground plane at the bottom of the structure is thicker than the penetration depth of infrared light. This simplifies the absorption coefficient to $A = 1 - R$. The absorbance for both TE and TM polarization at normal incidence is shown in Figure 7.2. Simulation results demonstrate that the absorber's properties are polarization-sensitive, with absorption exceeding 99% for TE polarization and nearly 40% for TM polarization in the 6-13 µm range of the C band in the far infrared region.
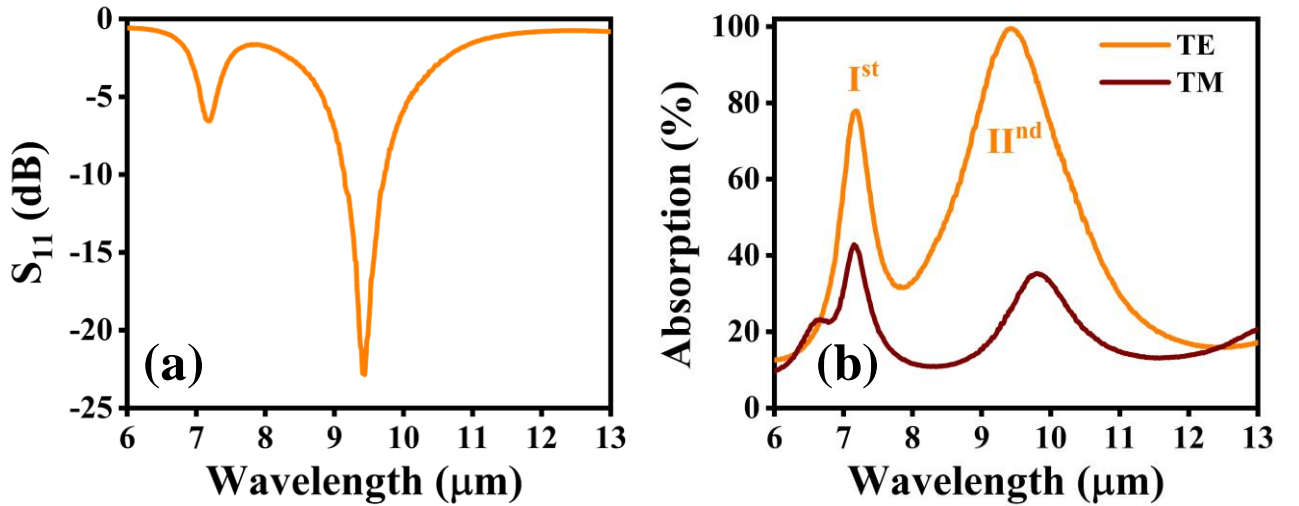
Figure 7.2 (a) Reflection coefficient (S_{11}) response and **(b)** Absorption variation response showing resonance wavelengths of the designed MA unit cell.

Figure 7.2 (a) and (b) illustrate that the designed metamaterial unit cell resonates at two specific wavelengths, 7.18 µm and 9.40 µm, as indicated by the reflection coefficient (S_{11}) shown in Figure 7.2 (a). Figure 7.2 (b) highlights two absorption peaks, labelled I^{st} and IInd, with absorption rates of 77.92% and 99.47% respectively, in the Far Infrared (IR-C) band. Metamaterials, functioning as effective media, can be described by their complex effective electric permittivity ($\varepsilon_{eff.} = \varepsilon_1 + i\varepsilon_2$) and magnetic permeability ($\mu_{eff.} = \mu_1 + i\mu_2$). To design a resonant metamaterial absorber (MA), the goal is to match the impedance of the absorber with that of free space, thus minimizing reflection. This impedance (Z) is calculated using the S-parameter retrieval method [160,161]:

$$Z = Z_o = \sqrt{\frac{\mu_{eff.}}{\varepsilon_{eff.}}} \qquad 7.2$$

When Z_r is derived from transmission line theory, the absorption is defined as [162]:

$$Z_{eff.} = \frac{Z}{Z_o} \qquad 7.3$$

$$A = 1 - R = 1 - \left|\frac{Z - Z_o}{Z + Z_o}\right|^2 = 1 - \left|\frac{Z_{eff.} - 1}{Z_{eff.} + 1}\right|^2 \qquad 7.4$$

$$Z_{eff.} = \pm\sqrt{\frac{(1 + S_{11})^2 - S_{21}^2}{(1 - S_{11})^2 - S_{21}^2}} \qquad 7.5$$
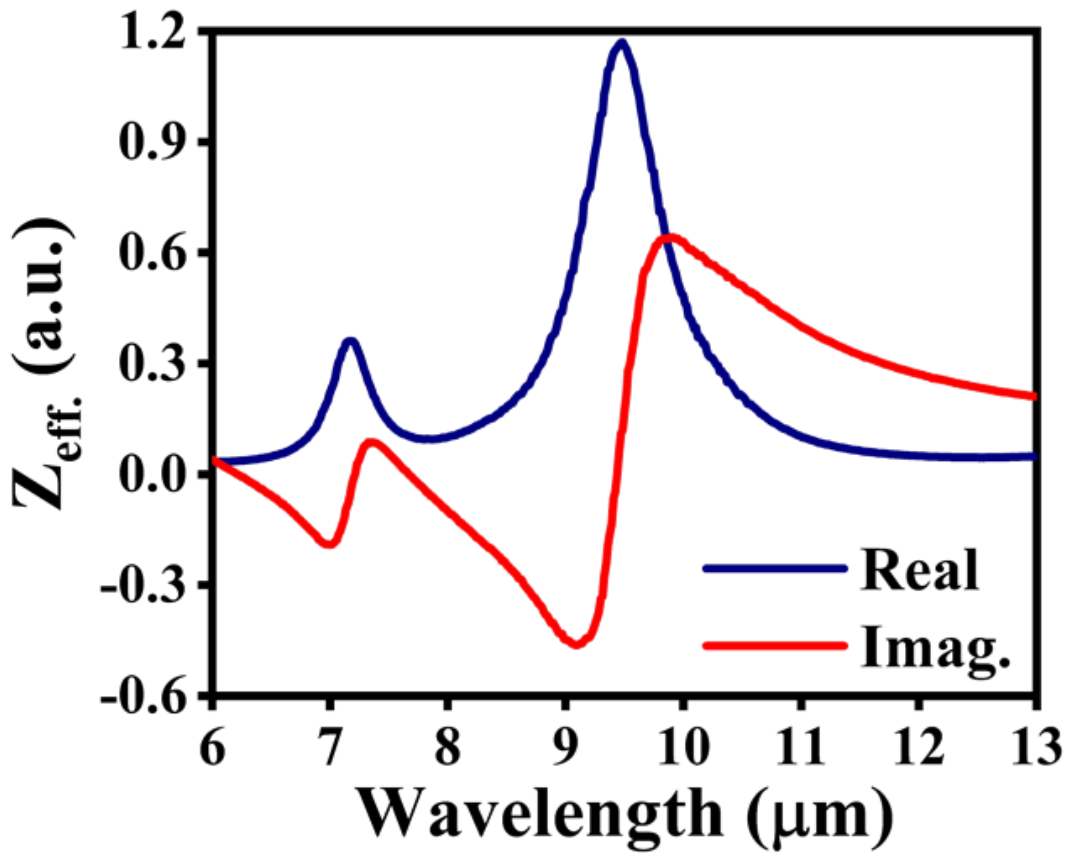
Figure 7.3 The effective impedance of the metamaterial unit cell showing perfect absorption at 9.40 µm

For a TE configuration, the effective impedance is derived from the reflection and transmission coefficients of the designed metamaterial unit cell, as depicted in Figure 7.3. According to the above equations (7.3-7.5), the real part of $Z_{eff.}$ is nearly one, and the imaginary part is close to zero at the second resonance wavelength, indicating an impedance match with free space [163]. This impedance matching condition leads to nearly perfect absorption at the resonance wavelength of 9.40 µm.

.
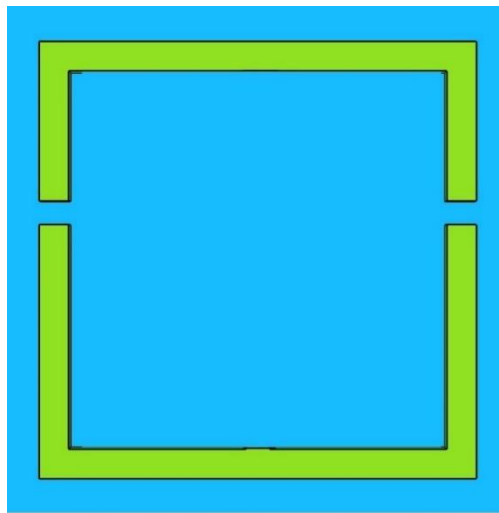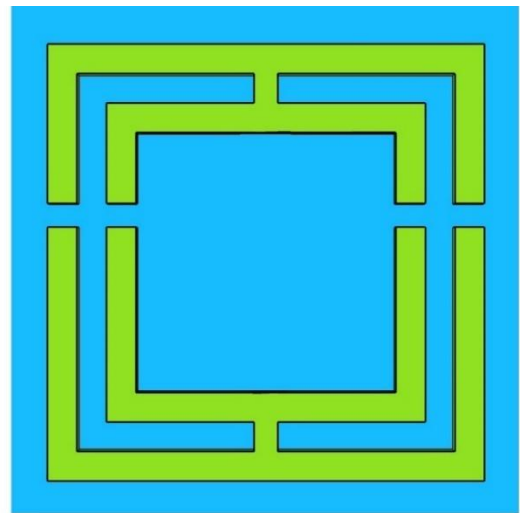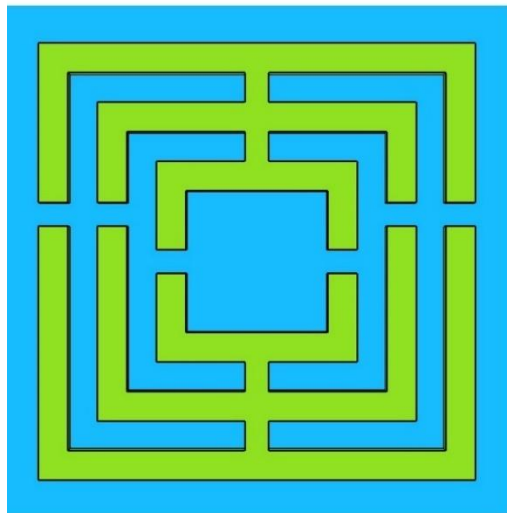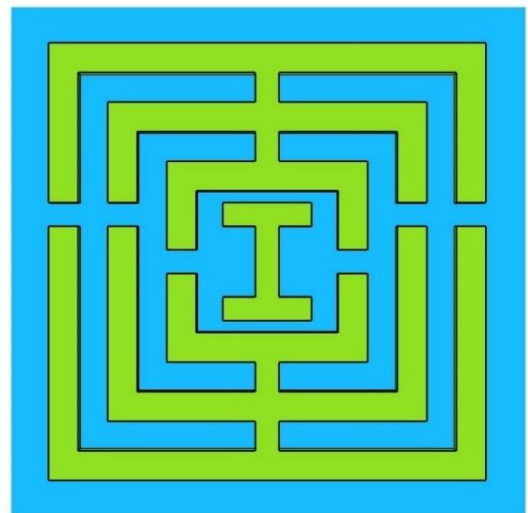
Figure 7.4 The step-by-step evolution from Design I to proposed design of metamaterial unit cell to achieve perfect absorption.

Four-unit cell layout structures were designed, and their absorption responses were analyzed as shown in Figure 7.4. Design 1 uses a single split ring resonator (SRR) with two split gaps of 0.1 µm and a thickness of 0.12 µm. This design exhibits an absorption response at a resonant wavelength of 10.02 µm, achieving an absorption of 95.6%. In Design 2, a SRR with the same thickness and two split gaps is placed inside the first ring resonator, with both rings interconnected from the vertical side. This shifts the absorption response to a resonant wavelength of 9.60 µm, with an absorption percentage of 98.7%. Design 3 adds another SRR, smaller in size, inside Design 2 with the same two

split gaps. This design shows an absorption response at a resonance wavelength of 9.20 µm, but it cannot achieve more than 99% absorption. The final design features a solid I-shape with a length and width of 0.37 µm and 0.1 µm, respectively. This design demonstrates maximum absorption responses of 77.92% and 99.47% at two resonance wavelengths, 7.18 µm and 9.40 µm, respectively, as shown in Figure 7.5.
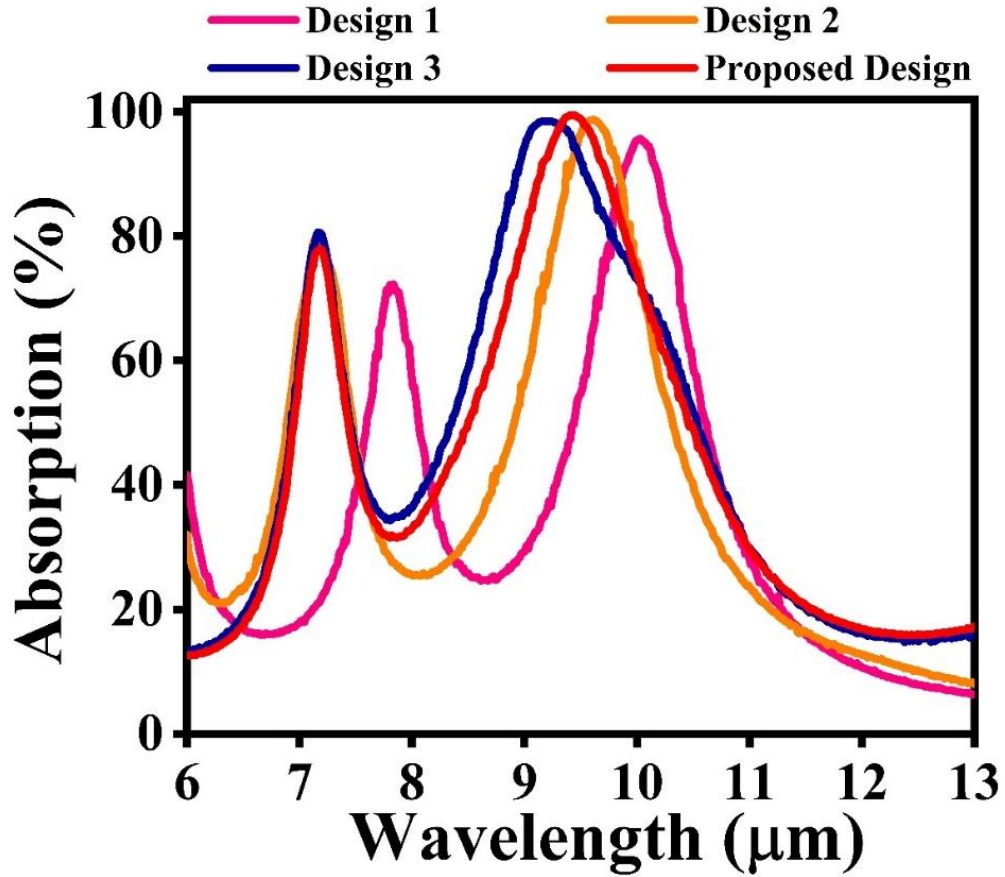
Figure 7.5 The response of different designs in terms of absorption corresponding to different designs steps.

7.3.1 Electric Field Profile

To provide a clear understanding of the absorption mechanism, we examine the distribution of the z component of the electric field in the TE configuration at the resonant wavelength of $\lambda = 9.40$ µm on the I-shaped split-ring resonator (SRR). The side view of the designed structure, depicted in Fig. 10, reveals crucial insights into the field distribution. As illustrated in Figure 7.6 (a), the electric field is predominantly concentrated in the gap regions (g), where the field intensity reaches 2.97×10^8 V/m. Furthermore, Figure 7.6 (b) demonstrates that the z component of the E-field is significantly concentrated at the metal-dielectric interface. This concentration at the interface is

indicative of the generation of Surface Plasmon Resonance (SPR), a phenomenon that amplifies the local electromagnetic fields at specific resonant wavelengths. The presence of SPR at the metal-dielectric interface thus plays a pivotal role in enhancing the absorption efficiency of the metamaterial at the designated resonant wavelength [164,165].
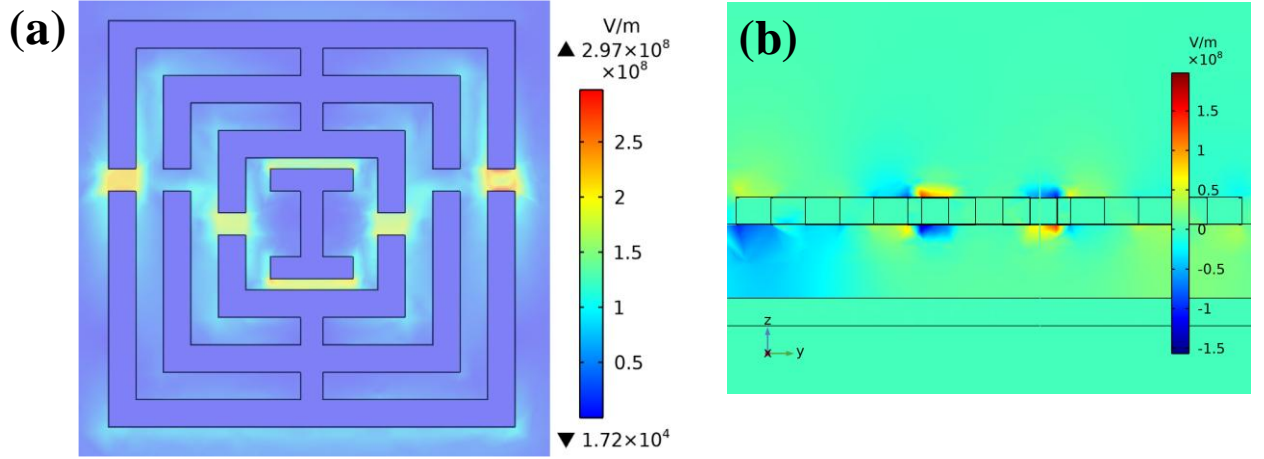
Figure 7.6 The electric field distribution from **(a)** top view and **(b)** YZ direction of the electric field distribution of the proposed absorber at λ_r equals to 9.40 μm.

7.3.2 Refractive index (RI) sensing application
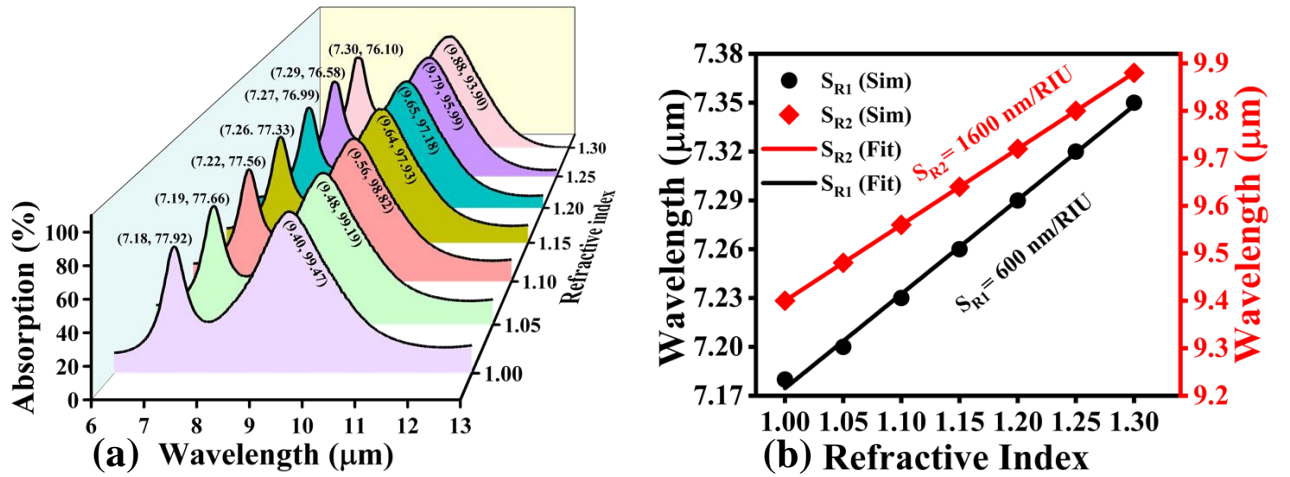
Figure 7.7 (a) Absorption spectra of the proposed MA sensor using different RI values of the surrounding environment. **(b)** The variation of simulated resonance wavelength (square and circle symbols) and linear fitting (solid line) with different RI values of the surrounding environment.

The following section examines the change in absorption with respect to various refractive index values to evaluate RI sensitivity. The study of RI sensing properties involves altering the surrounding environment of the metamaterial to correspond with changes in its RI, which in turn causes a shift in

the λ_r of the proposed MA, as shown in Figure 7.7 (b). Sensitivity (S_R) serve as a crucial benchmark for evaluating sensing performance and is defined by equation (5.1).

The absorption spectra exhibit a red shift as the refractive index of the surrounding environment changes from 1.00 to 1.30, as shown in Figure 7.7 (a). Figure 7.7 (b) illustrates the correlation between the shift in λ_r ($\Delta\lambda$) and the variations in RI (Δn) of the surrounding environment. Additionally, the resonance wavelength of the proposed MA shows a linear increase with the rise in the refractive index of the surrounding environment. The sensitivities, S_{R1} and S_{R2}, corresponding to the first and second resonance peaks in the far infrared C band (IR-C), are approximately 600 nm/RIU and 1600 nm/RIU, respectively. These sensitivities surpass those of previously reported MA sensors, as noted in Table 7.2. Therefore, it can be concluded that the suggested MA sensor has a high refractive index sensitivity in the IR-C band.

Table 7.2 Comparison of sensitivity of the proposed MA structure with the previous literature work.

Reference	Designed structure	Sensitivity
[166]	Cut out	$S_R = 928.9 \; nm/RIU$
[167]	Slot strip	$S_R = 700 \; nm/RIU$
[168]	Nano slit	$S_R = 190 \; nm/RIU$
[169]	Vertical Split ring structure	$S_R = 1194 \; nm/RIU$
[170]	Silicon meta-atoms	$S_R = 460 \; nm/RIU$
[171]	Trapezoidal silver array	$S_R = 228 \; nm/RIU$
[172]	Asymmetric metasurface	$S_R = 418 \; nm/RIU$
This work	**SRR with I-shaped**	$\mathbf{S_{R_1} = 600 \; nm/RIU}$ $\mathbf{S_{R_2} = 1600 \; nm/RIU}$

7.4   SUMMARY

We proposed a MPA specifically designed for the far-infrared C-band. The MPA structure includes a SRR with an I-shaped copper top layer, a silicon dielectric base layer, and a copper bottom layer (t_c). Using the FEM within COMSOL Multiphysics software, we analyzed the absorption characteristics of this structure in the far-IR band. The absorption rate achieved was an impressive 99.47% at a wavelength of $\lambda_r = 9.40$ μm, indicating perfect absorption and impedance matching with free space at this resonance. We also investigated how different structural parameters and incidence angle affected absorption efficiency. Furthermore, by varying the refractive index of the surrounding environment, the sensing performance (S_R) of the structure was assessed, and it was discovered that the S_R may reach up to 1600 nm/RIU. The device also demonstrated sensitivity to both TE and TM polarizations. Overall, our metamaterial perfect absorber shows significant potential for applications in imaging, sensing, and biomedical diagnostics.

CHAPTER- 8

CHAPTER 8: CONCLUDING REMARKS AND FUTURE RESEARCH SCOPE

In this concluding chapter, the research conducted in this thesis is summarized, and future directions are outlined. The thesis encompasses the exploration and evaluation of various metasurface and metamaterial designs aimed at applications such as perfect reflectors, wide bandwidth communication (including Wi-Fi and satellite), and refractive index sensors.

One significant contribution involves the development and analysis of an eye-shaped CC-SRR metasurface structure on an FR-4 dielectric substrate, demonstrating characteristics like effective negative refractive index (ENG) and near-zero refractive index (NZI) within the frequency range of 1-15 GHz. Experimental measurements closely match simulated results, indicating minimal frequency deviations and suggesting the structure's suitability for microwave components in different frequency bands.

Another notable achievement is the design of a nearly perfect reflector with a tunable metamaterial (MTM) structure for optical communication, particularly at a resonance wavelength of 1550 nm. Parametric studies on substrate materials and thicknesses result in effective negative refractive index properties, making it suitable for long-distance optical transmission.

A novel all-dielectric metasurface made of SOI material serves as a perfect reflector in the visible region, with resonances analyzed using COMSOL Multiphysics. Tunability is achieved by adjusting various parameters and showcasing consistent responses in scattering parameters regardless of the structure's orientation.

Additionally, a dual-band operation MTM structure with refractive index sensing capability is analyzed, demonstrating effective negative and near-zero refractive index for dual-band operations, making it applicable as a refractive index sensor with notable sensitivity.

A triple-band operation MTM structure with wide bandwidth in the C-band is designed, offering an effective negative refractive index for multi-band operations, particularly suitable for satellite communications and radar applications.

Lastly, a far-infrared metamaterial perfect absorber with sensing applications has been designed and results demonstrate that the designed structure achieves nearly perfect absorption of transverse electric (TE) polarization at a resonance wavelength.

Looking forward, potential areas for further exploration includes:

Exploration of Novel Materials: Future studies could focus on utilizing advanced materials, such as 2D materials (e.g., graphene, hexagonal boron nitride) or metamaterials with tunable properties (e.g., phase-change materials), to achieve better performance in terms of tunability and refractive index manipulation.

High-Frequency Designs: Expanding the range of operating frequencies, particularly beyond the GHz and into the THz range, could provide valuable insights for applications in terahertz communications, imaging, and sensing.

Wideband Metamaterials: Investigating new geometries and materials that allow for wider bandwidth in both microwave and optical frequency ranges could increase the versatility of these structures.

Biocompatible and Flexible Materials: The development of metasurfaces using flexible, lightweight, and biocompatible materials could enable applications in wearable electronics, medical devices, and bio-sensing.

Higher Efficiency Reflectors: Future work could focus on improving the efficiency and minimizing losses in perfect reflectors, especially for optical communication and beyond visible frequencies.

Polarization Control: Research could explore controlling polarization states (linear, circular, etc.) more effectively in metamaterial absorbers and reflectors, making them more adaptable for practical applications in radar and remote sensing.

Further future research scope also includes:

➢ Enhancing gain and directivity of metamaterial-based antennas.

➢ Designing dielectric metamaterial absorbers for sensing applications.

➢ Exploring new designs for ENZ/MNZ/EMNZ-based metamaterials and their applications at the nanoscale, such as optical couplers, optical switches, and polarizers.

REFERENCES

[1]   J.C. Maxwell, A dynamical theory of the electromagnetic field, Phil. Trans. R. Soc. Lond. 155 (1865) 459–512.

[2]   J.D. Jackson, R.F. Fox, Classical Electrodynamics, 3rd ed ., Am. J. Phys. 67 (1999) 841–842. https://doi.org/10.1119/1.19136.

[3]   M.C.K. Wiltshire, Radio frequency (RF) metamaterials, Phys. Status Solidi. 244 (2007) 1227–1236. https://doi.org/10.1002/pssb.200674511.

[4]   A. Alù, N. Engheta, Optical nanotransmission lines: synthesis of planar left-handed metamerials in the infrared and visible regimes, J. Opt. Soc. Am. B. 23 (2006) 571. https://doi.org/10.1364/JOSAB.23.000571.

[5]   On the rotation of plane of polarisation of electric wave by a twisted structure, Proc. R. Soc. London. 63 (1898) 146–152. https://doi.org/10.1098/rspl.1898.0019.

[6]   W.E. Kock, Metallic Delay Lenses, Bell Syst. Tech. J. 27 (1948) 58–82. https://doi.org/10.1002/j.1538-7305.1948.tb01331.x.

[7]   W. Rotman, Plasma simulation by artificial dielectrics and parallel-plate media, IRE Trans. Antennas Propag. 10 (1962) 82–95. https://doi.org/10.1109/TAP.1962.1137809.

[8]   D. Dutton, Progress in Dielectrics., J. Am. Chem. Soc. 82 (1960) 5261–5262. https://doi.org/10.1021/ja01504a080.

[9]   J.B. Pendry, A.J. Holden, D.J. Robbins, W.J. Stewart, Magnetism from conductors and enhanced nonlinear phenomena, IEEE Trans. Microw. Theory Tech. 47 (1999) 2075–2084. https://doi.org/10.1109/22.798002.

[10]   D.R. Smith, W.J. Padilla, D.C. Vier, S.C. Nemat-Nasser, S. Schultz, Composite Medium with Simultaneously Negative Permeability and Permittivity, Phys. Rev. Lett. 84 (2000) 4184–4187. https://doi.org/10.1103/PhysRevLett.84.4184.

[11]   V.G. Veselago, The electrodynamics of substances with simultaneously negative values of epsilon and μ, Sov. Phys. Uspekhi. 10 (1968) 509–514. https://doi.org/10.1070/PU1968v010n04ABEH003699.

[12]   V.G. Veselago, E.E. Narimanov, The left hand of brightness: past, present and future of negative index materials, Nat. Mater. 5 (2006) 759–762. https://doi.org/10.1038/nmat1746.

[13]   H. Lamb, On Group - Velocity, Proc. London Math. Soc. s2-1 (1904) 473–479. https://doi.org/10.1112/plms/s2-1.1.473.

[14]   H.C. POCKLINGTON, Growth of a Wave-group when the Group-velocity is Negative, Nature. 71 (1905) 607–608. https://doi.org/10.1038/071607b0.

[15]   F. Capolino, Theory and Phenomena of Metamaterials, CRC Press, 2017. https://doi.org/10.1201/9781420054262.

[16]   J.B. Pendry, D.R. Smith, Reversing Light With Negative Refraction, Phys. Today. 57 (2004) 37–43. https://doi.org/10.1063/1.1784272.

[17]   L.D. Landau, E.M. Lifshitz, Electrodynamics of Contunuous Media -Volume 8 of Theoretical Physics, (1984) 1–474.

[18]   R. Merlin, Metamaterials and the Landau–Lifshitz permeability argument: Large permittivity begets high-frequency magnetism, Proc. Natl. Acad. Sci. 106 (2009) 1693–1698. https://doi.org/10.1073/pnas.0808478106.

[19]   G.W. Milton, The Theory of Composites, Theory Compos. (2022). https://doi.org/10.1137/1.9781611977486.

[20]   and M.P.-M. Taflove, Allen, Susan C. Hagness, Computational electrodynamics: the finite-difference time-domain method, Academia Press, 2005.

[21]   M.N.O. Sadiku, Numerical Techniques in Electromagnetics, CRC Press, 2000. https://doi.org/10.1201/9781420058277.

[22]   J.-M. Jin, The finite element method in electromagnetics, 3rd ed., John Wiley & Sons, 2015.

[23]   K. Aydin, K. Guven, N. Katsarakis, C.M. Soukoulis, E. Ozbay, Effect of disorder on magnetic resonance band gap of split-ring resonator structures, Opt. Express. 12 (2004) 5896. https://doi.org/10.1364/OPEX.12.005896.

[24]   W.N. Hardy, L.A. Whitehead, Split-ring resonator for use in magnetic resonance from 200–2000 MHz, Rev. Sci. Instrum. 52 (1981) 213–216. https://doi.org/10.1063/1.1136574.

[25]   D.R. Smith, J.B. Pendry, M.C.K. Wiltshire, Metamaterials and Negative Refractive Index, Science (80-.). 305 (2004) 788–792. https://doi.org/10.1126/science.1096796.

[26]   W. Cai, V. Shalaev, Optical Metamaterials, Springer New York, New York, NY, 2010. https://doi.org/10.1007/978-1-4419-1151-3.

[27]   S.A. Ramakrishna, Physics of negative refractive index materials, Reports Prog. Phys. 68 (2005) 449–521. https://doi.org/10.1088/0034-4885/68/2/R06.

[28]   R.A. Shelby, D.R. Smith, S. Schultz, Experimental Verification of a Negative Index of Refraction, Science (80-.). 292 (2001) 77–79. https://doi.org/10.1126/science.1058847.

[29]   Nader Engheta, R.W. Ziolkowski, A positive future for double-negative metamaterials, IEEE Trans. Microw. Theory Tech. 53 (2005) 1535–1556. https://doi.org/10.1109/TMTT.2005.845188.

[30]   N. Shankhwar, R.K. Sinha, Applications of Zero-Index Metamaterials, in: Zero Index Metamaterials, Springer Singapore, Singapore, 2021: pp. 57–82. https://doi.org/10.1007/978-981-16-0189-7_3.

[31]   B. Wang, T. Koschny, C.M. Soukoulis, Wide-angle and polarization-independent chiral metamaterial absorber, Phys. Rev. B. 80 (2009) 033108. https://doi.org/10.1103/PhysRevB.80.033108.

[32]   C.M. Bingham, H. Tao, X. Liu, R.D. Averitt, X. Zhang, W.J. Padilla, Planar wallpaper group metamaterials for novel terahertz applications, Opt. Express. 16 (2008) 18565. https://doi.org/10.1364/OE.16.018565.

[33]   X. Liu, T. Tyler, T. Starr, A.F. Starr, N.M. Jokerst, W.J. Padilla, Taming the Blackbody with Infrared Metamaterials as Selective Thermal Emitters, Phys. Rev. Lett. 107 (2011) 045901. https://doi.org/10.1103/PhysRevLett.107.045901.

[34]   N. Liu, M. Mesch, T. Weiss, M. Hentschel, H. Giessen, Infrared Perfect Absorber and Its Application As Plasmonic Sensor, Nano Lett. 10 (2010) 2342–2348. https://doi.org/10.1021/nl9041033.

[35]   C. Enkrich, F. Pérez-Willard, D. Gerthsen, J.F. Zhou, T. Koschny, C.M. Soukoulis, M. Wegener, S. Linden, Focused-Ion-Beam Nanofabrication of Near-Infrared Magnetic Metamaterials, Adv. Mater. 17 (2005) 2547–2549. https://doi.org/10.1002/adma.200500804.

[36]   C. Wu, B. Neuner, G. Shvets, J. John, A. Milder, B. Zollars, S. Savoy, Large-area wide-angle spectrally selective plasmonic absorber, Phys. Rev. B. 84 (2011) 075102. https://doi.org/10.1103/PhysRevB.84.075102.

[37]   J. Zhao, B. Frank, S. Burger, H. Giessen, Large-Area High-Quality Plasmonic Oligomers Fabricated by Angle-Controlled Colloidal Nanolithography, ACS Nano. 5 (2011) 9009–9016. https://doi.org/10.1021/nn203177s.

[38]   Ansys HFSS, (n.d.). http://www.ansys.com.

[39]   CST Microwave Studio, (n.d.). https://www.cst.com.

[40]   COMSOL Multiphysics, (n.d.). http://www.comsol.com.

[41]   Y. Huang, J. Li, W. Yang, Modeling Backward Wave Propagation in Metamaterials by the Finite Element Time-Domain Method, SIAM J. Sci. Comput. 35 (2013) B248–B274. https://doi.org/10.1137/120869869.

[42]   P.P. (Peter P. Silvester, T. Itoh, G. Pelosi, Finite element software for microwave engineering, Wiley, New York, 1996.

[43]   E.J. Rothwell, J.L. Frasch, S.M. Ellison, P. Chahal, R.O. Ouedraogo, Analysis of the Nicolson-Ross-Weir method for characterizing the electromagnetic properties of engineered materials, Prog. Electromagn. Res. 157 (2016) 31–47. https://doi.org/10.2528/PIER16071706.

[44]   S.S. Islam, M.R.I. Faruque, M.T. Islam, A new direct retrieval method of refractive index for the metamaterial, Curr. Sci. 109 (2015) 337–342. https://doi.org/10.18520/cs/v109/i2/337-342.

[45]   X. Chen, T.M. Grzegorczyk, B.I. Wu, J. Pacheco, J.A. Kong, Robust method to retrieve the constitutive effective parameters of metamaterials, Phys. Rev. E - Stat. Physics, Plasmas, Fluids, Relat. Interdiscip. Top. 70 (2004) 7. https://doi.org/10.1103/PhysRevE.70.016608.

[46]   R.W. Ziolkowski, E. Heyman, Wave propagation in media having negative permittivity and permeability, Phys. Rev. E - Stat. Physics, Plasmas, Fluids, Relat. Interdiscip. Top. 64 (2001) 15. https://doi.org/10.1103/PhysRevE.64.056625.

[47]   C. Sabah, Tunable metamaterial design composed of triangular split ring resonator and wire strip for s- and c- microwave bands, Prog. Electromagn. Res. B. 22 (2010) 341–357. https://doi.org/10.2528/PIERB10051705.

[48]   R.W. Ziolkowski, Design, fabrication, and testing of double negative metamaterials, IEEE Trans. Antennas Propag. 51 (2003) 1516–1529. https://doi.org/10.1109/TAP.2003.813622.

[49]   R. Liu, C. Ji, Z. Zhao, T. Zhou, Metamaterials: Reshape and Rethink, Engineering. 1 (2015) 179–184. https://doi.org/10.15302/J-ENG-2015036.

[50]   T.J. Cui, W.X. Tang, X.M. Yang, Z.L. Mei, W.X. Jiang, Metamaterials, CRC Press, Boca Raton: Taylor & Francis, 2016. | "A CRC title.," 2017. https://doi.org/10.1201/9781315373614.

[51]   R.W. ZIOLKOWSKI, Metamaterial-Based Antennas: Research and Developments, IEICE Trans. Electron. E89-C (2006) 1267–1275. https://doi.org/10.1093/ietele/e89-c.9.1267.

[52] T. Koschny, P. Markoš, D.R. Smith, C.M. Soukoulis, Resonant and antiresonant frequency dependence of the effective parameters of metamaterials, Phys. Rev. E. 68 (2003) 065602. https://doi.org/10.1103/PhysRevE.68.065602.

[53] M.J. Hossain, M.R.I. Faruque, S.S. Islam, M.T. Islam, Subwavelength operating metamaterial for multiband applications, Microw. Opt. Technol. Lett. 58 (2016) 3004–3008. https://doi.org/10.1002/mop.30202.

[54] H. Jeong, T.T. Nguyen, S. Lim, Subwavelength Metamaterial Unit Cell for Low-Frequency Electromagnetic Absorber Applications, Sci. Rep. 8 (2018) 16774. https://doi.org/10.1038/s41598-018-35267-w.

[55] K. Kishor, M.N. Baitha, R.K. Sinha, B. Lahiri, Tunable negative refractive index metamaterial from V-shaped SRR structure: fabrication and characterization, J. Opt. Soc. Am. B. 31 (2014) 1410. https://doi.org/10.1364/josab.31.001410.

[56] D. Schurig, J.J. Mock, B.J. Justice, S.A. Cummer, J.B. Pendry, A.F. Starr, D.R. Smith, Metamaterial Electromagnetic Cloak at Microwave Frequencies, Science (80-.). 314 (2006) 977–980. https://doi.org/10.1126/science.1133628.

[57] H.O. Yilmaz, F. Yaman, Metamaterial Antenna Designs for a 5.8-GHz Doppler Radar, IEEE Trans. Instrum. Meas. 69 (2020) 1775–1782. https://doi.org/10.1109/TIM.2019.2914131.

[58] P. Agarwal, K. Kishor, R.K. Sinha, Ultrasensitive dual-band terahertz metasurface sensor based on all InSb resonator, Opt. Commun. 522 (2022) 128667. https://doi.org/10.1016/J.OPTCOM.2022.128667.

[59] H. Saghaei, P. Elyasi, B.J. Shastri, Sinusoidal and rectangular Bragg grating filters: Design, fabrication, and comparative analysis, J. Appl. Phys. 132 (2022) 064501. https://doi.org/10.1063/5.0098923.

[60] H. Saghaei, Dispersion-engineered microstructured optical fiber for mid-infrared supercontinuum generation, Appl. Opt. 57 (2018) 5591. https://doi.org/10.1364/AO.57.005591.

[61] H. Saghaei, P. Elyasi, R. Karimzadeh, Design, fabrication, and characterization of Mach–Zehnder interferometers, Photonics Nanostructures - Fundam. Appl. 37 (2019) 100733. https://doi.org/10.1016/j.photonics.2019.100733.

[62] Ankit, K. Kishor, R.K. Sinha, Design and analysis of wavelength tunable metamaterial reflector, Results Opt. 10 (2023) 100366. https://doi.org/10.1016/j.rio.2023.100366.

[63] E. Karakaya, F. Bagci, S. Can, A.E. Yilmaz, B. Akaoglu, Four-band electromagnetic energy harvesting with a dual-layer metamaterial structure, Int. J. RF Microw. Comput. Eng. 29 (2019) e21644. https://doi.org/10.1002/mmce.21644.

[64] H. Zhu, Y. Zhang, L. Ye, Y. Li, Z. Dang, R. Xu, B. Yan, A High Q -factor Metamaterial Absorber and Its Refractive Index Sensing Characteristics, IEEE Trans. Microw. Theory Tech. 70 (2022) 5383–5391. https://doi.org/10.1109/TMTT.2022.3218041.

[65] F. Tavakoli, F.B. Zarrabi, H. Saghaei, Modeling and analysis of high-sensitivity refractive index sensors based on plasmonic absorbers with Fano response in the near-infrared spectral region, Appl. Opt. 58 (2019) 5404. https://doi.org/10.1364/AO.58.005404.

[66] N. Benmostefa, M. Meliani, H. Ouslimani, Metamaterial Tunable Filter Design, J. Electromagn. Anal. Appl. 05 (2013) 250–254. https://doi.org/10.4236/jemaa.2013.56040.

[67] I.C. Hunter, J.D. Rhodes, M.Y. Sandhu, R. V. Snyder, M. Meng, Multimode Propagation in 2-D Filters and Metamaterials, IEEE Trans. Microw. Theory Tech. 64 (2016) 4204–4210. https://doi.org/10.1109/TMTT.2016.2613046.

[68] S. Haxha, F. AbdelMalek, F. Ouerghi, M.D.B. Charlton, A. Aggoun, X. Fang, Metamaterial Superlenses Operating at Visible Wavelength for Imaging Applications, Sci. Rep. 8 (2018) 16119. https://doi.org/10.1038/s41598-018-33572-y.

[69] M. Bellal Hossain, M. Rashed Iqbal Faruque, A.S. Alshammari, M. Tariqul Islam, Wide bandwidth enriched symmetric hexagonal split ring resonator based triple band negative permittivity metamaterial for satellite and Wi-Fi applications, Results Phys. 37 (2022) 105511. https://doi.org/10.1016/j.rinp.2022.105511.

[70] M.B. Hossain, M.R.I. Faruque, M.T. Islam, Double elliptical resonator based quadruple band metamaterial absorber for EMI shielding applications in microwave regime, Alexandria Eng. J. 69 (2023) 193–206. https://doi.org/10.1016/j.aej.2023.01.035.

[71] Y. Guo, J. Zhou, Dual-band-enhanced Transmission through a Subwavelength Aperture by Coupled Metamaterial Resonators, Sci. Rep. 5 (2015) 8144. https://doi.org/10.1038/srep08144.

[72] M. Moniruzzaman, M.T. Islam, N. Misran, M. Samsuzzaman, T. Alam, M.E.H. Chowdhury, Inductively tuned modified split ring resonator based quad band epsilon negative (ENG) with near zero index (NZI) metamaterial for multiband antenna performance enhancement, Sci. Rep. 11 (2021) 11950. https://doi.org/10.1038/s41598-021-91432-8.

[73] I.B. Vendik, O.G. Vendik, Metamaterials and their application in microwaves: A review, Tech. Phys. 58 (2013) 1–24. https://doi.org/10.1134/S1063784213010234.

[74] W. Xu, L. Xie, Y. Ying, Mechanisms and applications of terahertz metamaterial sensing: A review, Nanoscale. 9 (2017) 13864–13878. https://doi.org/10.1039/c7nr03824k.

[75] S. Xiao, V.P. Drachev, A. V. Kildishev, X. Ni, U.K. Chettiar, H.-K. Yuan, V.M. Shalaev, Loss-free and active optical negative-index metamaterials, Nature. 466 (2010) 735–738. https://doi.org/10.1038/nature09278.

[76] S. O'Brien, J.B. Pendry, Photonic band-gap effects and magnetic activity in dielectric composites, J. Phys. Condens. Matter. 14 (2002) 4035–4044. https://doi.org/10.1088/0953-8984/14/15/317.

[77] Q. Zhao, J. Zhou, F. Zhang, D. Lippens, Mie resonance-based dielectric metamaterials, Mater. Today. 12 (2009) 60–69. https://doi.org/10.1016/S1369-7021(09)70318-9.

[78] B. Slovick, Z.G. Yu, M. Berding, S. Krishnamurthy, Perfect dielectric-metamaterial reflector, Phys. Rev. B. 88 (2013) 165116. https://doi.org/10.1103/PhysRevB.88.165116.

[79] D.R. Smith, D.C. Vier, T. Koschny, C.M. Soukoulis, Electromagnetic parameter retrieval from inhomogeneous metamaterials, Phys. Rev. E. 71 (2005) 036617. https://doi.org/10.1103/PhysRevE.71.036617.

[80] M. Shur, Physics of semiconductor devices, Prentice Hall, Englewood Cliffs, NJ, 1990.

[81] I.H. Malitson, Interspecimen Comparison of the Refractive Index of Fused Silica, J. Opt. Soc. Am. 55 (1965) 1205. https://doi.org/10.1364/JOSA.55.001205.

[82] P. Moitra, B.A. Slovick, W. Li, I.I. Kravchencko, D.P. Briggs, S. Krishnamurthy, J. Valentine, Large-Scale All-Dielectric Metamaterial Perfect Reflectors, ACS Photonics. 2 (2015) 692–698. https://doi.org/10.1021/acsphotonics.5b00148.

[83] P. Moitra, B.A. Slovick, Z. Gang Yu, S. Krishnamurthy, J. Valentine, Experimental demonstration of a broadband all-dielectric metamaterial perfect reflector, Appl. Phys. Lett. 104 (2014). https://doi.org/10.1063/1.4873521.

[84] C. Chen, Z. Wang, Z. Zheng, Y. Liu, W. Huang, L. Chen, Large-area, low-cost near-infrared meta-surface reflector based on a pixelated two-dimensional silicon disk array, Opt. Express. 28 (2020) 38355. https://doi.org/10.1364/oe.412521.

[85] A.F. Almutairi, M.S. Islam, M. Samsuzzaman, M.T. Islam, N. Misran, M.T. Islam, A complementary split ring resonator based metamaterial with effective medium ratio for C-band microwave applications, Results Phys. 15 (2019) 102675. https://doi.org/10.1016/j.rinp.2019.102675.

[86] B.A. Slovick, Z.G. Yu, S. Krishnamurthy, Generalized effective-medium theory for metamaterials, Phys. Rev. B. 89 (2014) 155118. https://doi.org/10.1103/PhysRevB.89.155118.

[87] S.S. Islam, M.R.I. Faruque, M.T. Islam, A new double negative metamaterial for multi-band microwave applications, Appl. Phys. A. 116 (2014) 723–733. https://doi.org/10.1007/s00339-014-8549-2.

[88] C.M. Watts, X. Liu, W.J. Padilla, Metamaterial Electromagnetic Wave Absorbers, Adv. Mater. 24 (2012) OP98–OP120. https://doi.org/10.1002/adma.201200674.

[89] J.B. Pendry, Negative Refraction Makes a Perfect Lens, Phys. Rev. Lett. 85 (2000) 3966–3969. https://doi.org/10.1103/PhysRevLett.85.3966.

[90] Y. Huang, L. Yang, J. Li, Y. Wang, G. Wen, Polarization conversion of metasurface for the application of wide band low-profile circular polarization slot antenna, Appl. Phys. Lett. 109 (2016) 054101. https://doi.org/10.1063/1.4960198.

[91] J.B. Pendry, A.J. Holden, W.J. Stewart, I. Youngs, Extremely Low Frequency Plasmons in Metallic Mesostructures, Phys. Rev. Lett. 76 (1996) 4773–4776. https://doi.org/10.1103/PhysRevLett.76.4773.

[92] Haixia Ma and Xuenan Wang, Wide-angle broadband near-perfect all-dielectric metamaterial reflector, Opt. Eng. 57 (2018) 1. https://doi.org/10.1117/1.OE.57.1.017102.

[93] S. Jahani, Z. Jacob, All-dielectric metamaterials, Nat. Nanotechnol. 11 (2016) 23–36. https://doi.org/10.1038/nnano.2015.304.

[94] Q. Zhao, J. Zhou, F. Zhang, D. Lippens, Mie resonance-based dielectric metamaterials, Mater. Today. 12 (2009) 60–69. https://doi.org/10.1016/S1369-7021(09)70318-9.

[95] A.I. Kuznetsov, A.E. Miroshnichenko, Y.H. Fu, J. Zhang, B. Luk'yanchuk, Magnetic light, Sci. Rep. 2 (2012) 492. https://doi.org/10.1038/srep00492.

[96] A.I. Kuznetsov, A.E. Miroshnichenko, M.L. Brongersma, Y.S. Kivshar, B. Luk'yanchuk, Optically resonant dielectric nanostructures, Science (80-.). 354 (2016). https://doi.org/10.1126/science.aag2472.

[97] M. Decker, I. Staude, M. Falkner, J. Dominguez, D.N. Neshev, I. Brener, T. Pertsch, Y.S. Kivshar, High-Efficiency Dielectric Huygens' Surfaces, Adv. Opt. Mater. 3 (2015) 813–820. https://doi.org/10.1002/adom.201400584.

[98]   I. Staude, A.E. Miroshnichenko, M. Decker, N.T. Fofang, S. Liu, E. Gonzales, J. Dominguez, T.S. Luk, D.N. Neshev, I. Brener, Y. Kivshar, Tailoring Directional Scattering through Magnetic and Electric Resonances in Subwavelength Silicon Nanodisks, ACS Nano. 7 (2013) 7824–7832. https://doi.org/10.1021/nn402736f.

[99]   B. Wang, G.P. Wang, Plasmon Bragg reflectors and nanocavities on flat metallic surfaces, Appl. Phys. Lett. 87 (2005) 013107. https://doi.org/10.1063/1.1954880.

[100]   L. Hvozdara, A. Lugstein, N. Finger, S. Gianordoli, W. Schrenk, K. Unterrainer, E. Bertagnolli, G. Strasser, E. Gornik, Quantum cascade lasers with monolithic air–semiconductor Bragg reflectors, Appl. Phys. Lett. 77 (2000) 1241–1243. https://doi.org/10.1063/1.1289910.

[101]   B.S. Kawasaki, K.O. Hill, D.C. Johnson, Y. Fujii, Narrow-band Bragg reflectors in optical fibers, Opt. Lett. 3 (1978) 66. https://doi.org/10.1364/OL.3.000066.

[102]   D. Shin, J. Kim, C. Kim, K. Bae, S. Baek, G. Kang, Y. Urzhumov, D.R. Smith, K. Kim, Scalable variable-index elasto-optic metamaterials for macroscopic optical components and devices, Nat. Commun. 8 (2017) 16090. https://doi.org/10.1038/ncomms16090.

[103]   Y. Kim, S. Baek, P. Gupta, C. Kim, K. Chang, S.-P. Ryu, H. Kang, W.S. Kim, J. Myoung, W. Park, K. Kim, Air-like plasmonics with ultralow-refractive-index silica aerogels, Sci. Rep. 9 (2019) 2265. https://doi.org/10.1038/s41598-019-38859-2.

[104]   K. Kanamori, M. Aizawa, K. Nakanishi, T. Hanada, New Transparent Methylsilsesquioxane Aerogels and Xerogels with Improved Mechanical Properties, Adv. Mater. 19 (2007) 1589–1593. https://doi.org/10.1002/adma.200602457.

[105]   A.R. Buzykaev, A.F. Danilyuk, S.F. Ganzhur, E.A. Kravchenko, A.P. Onuchin, Measurement of optical parameters of aerogel, Nucl. Instruments Methods Phys. Res. Sect. A Accel. Spectrometers, Detect. Assoc. Equip. 433 (1999) 396–400. https://doi.org/10.1016/S0168-9002(99)00325-3.

[106]   Q. zhang, C. Liu, G. Gan, X. Cui, Visible perfect reflectors realized with all-dielectric metasurface, Opt. Commun. 402 (2017) 226–230. https://doi.org/10.1016/j.optcom.2017.05.053.

[107]   M.T. Islam, M. Moniruzzaman, T. Alam, M. Samsuzzaman, Q.A. Razouqi, A.F. Almutairi, Realization of frequency hopping characteristics of an epsilon negative metamaterial with high effective medium ratio for multiband microwave applications, Sci. Rep. 11 (2021) 16898. https://doi.org/10.1038/s41598-021-96228-4.

[108]   N. Krishna V, K.G. Padmasine, A review on microwave band pass filters: Materials and design optimization techniques for wireless communication systems, Mater. Sci. Semicond. Process. 154 (2023) 107181. https://doi.org/10.1016/j.mssp.2022.107181.

[109]   V. Kumar, D.K. Gupta, Microwave components and devices for RADAR systems, in: Radar Remote Sens., Elsevier, 2022: pp. 29–48. https://doi.org/10.1016/B978-0-12-823457-0.00012-4.

[110]   D.K. Gupta, S. Prashar, S. Singh, P.K. Srivastava, R. Prasad, Introduction to RADAR remote sensing, in: Radar Remote Sens., Elsevier, 2022: pp. 3–27. https://doi.org/10.1016/B978-0-12-823457-0.00018-5.

[111]   D. Shin, Y. Urzhumov, Y. Jung, G. Kang, S. Baek, M. Choi, H. Park, K. Kim, D.R. Smith, Broadband electromagnetic cloaking with smart metamaterials, Nat. Commun. 3 (2012) 1213. https://doi.org/10.1038/ncomms2219.

[112] J.B. Pendry, D. Schurig, D.R. Smith, Controlling Electromagnetic Fields, Science (80-.). 312 (2006) 1780–1782. https://doi.org/10.1126/science.1125907.

[113] W. Zhang, J.Y. Li, J. Xie, R. Xu, High Sensitivity Refractive Index Sensor Based on Frequency Selective Surfaces Absorber, IEEE Sensors Lett. 2 (2018) 107–115. https://doi.org/10.1109/LSENS.2018.2862389.

[114] W. Zhang, J.-Y. Li, J. Xie, High sensitivity refractive index sensor based on metamaterial absorber, Prog. Electromagn. Res. M. 71 (2018) 107–115. https://doi.org/10.2528/PIERM18042903.

[115] S. Hu, D. Liu, Dual-band microwave resonators based on cross hollow structures for refractive index sensing, Phys. Scr. 95 (2020) 085504. https://doi.org/10.1088/1402-4896/ab9bdd.

[116] M. Rashedul Islam, M. Tariqul Islam, M. Moniruzzaman, M. Samsuzzaman, B. Bais, H. Arshad, G. Muhammad, Square enclosed circle split ring resonator enabled epsilon negative (ENG) near zero index (NZI) metamaterial for gain enhancement of multiband satellite and radar antenna applications, Results Phys. 19 (2020) 103556. https://doi.org/10.1016/j.rinp.2020.103556.

[117] M. Moniruzzaman, M.T. Islam, I. Hossain, M.S. Soliman, M. Samsuzzaman, S.H.A. Almalki, Symmetric resonator based tunable epsilon negative near zero index metamaterial with high effective medium ratio for multiband wireless applications, Sci. Rep. 11 (2021) 21842. https://doi.org/10.1038/s41598-021-01266-7.

[118] I. Hossain, M. Tariqul Islam, N. Binti Mohd Sahar, A. Mohamed Moubark, M.S. Soliman, M. Samsuzzaman, Tunable Cross-Coupled metallic elements loaded epsilon negative and Near-Zero index characteristics based metamaterial, J. Magn. Magn. Mater. 565 (2023) 170226. https://doi.org/10.1016/j.jmmm.2022.170226.

[119] M. M. Bait-Suwailam, Electromagnetic Field Interaction with Metamaterials, in: Electromagn. Fields Waves, IntechOpen, 2019. https://doi.org/10.5772/intechopen.84170.

[120] Z. Wang, R. Zhang, J. Guo, Quadrupole mode plasmon resonance enabled subwavelength metal-dielectric grating optical reflection filters, Opt. Express. 26 (2018) 496. https://doi.org/10.1364/OE.26.000496.

[121] H. Liu, K. Wang, J. Gao, M. Liu, H. Zhang, Y. Zhang, Dirac semimetal and an all dielectric based tunable ultrasensitive terahertz sensor with multiple bound states in the continuum, Opt. Express. 30 (2022) 46471. https://doi.org/10.1364/OE.478457.

[122] M. Aftab, M.S. Mansha, T. Iqbal, M. Farooq, Surface Plasmon Excitation: Theory, Configurations, and Applications, Plasmonics. (2023). https://doi.org/10.1007/s11468-023-02095-2.

[123] Y. Tian, S. Hu, X. Huang, Z. Yu, H. Lin, H. Yang, Low-loss planar metamaterials electromagnetically induced transparency for sensitive refractive index sensing, J. Phys. D. Appl. Phys. 50 (2017) 405105. https://doi.org/10.1088/1361-6463/aa865b.

[124] N. Dadouche, Z. Mezache, J. Tao, E. Ali, M. Alsharef, A. Alwabli, A. Jaffar, A. Alzahrani, A. Berazguia, Design and Fabrication of a Novel Corona-Shaped Metamaterial Biosensor for Cancer Cell Detection, Micromachines. 14 (2023) 2114. https://doi.org/10.3390/mi14112114.

[125] J. Zhang, S. Yan, G.A.E. Vandenbosch, Metamaterial-inspired dual-band frequency-reconfigurable antenna with pattern diversity, Electron. Lett. 55 (2019) 573–574. https://doi.org/10.1049/el.2019.0329.

[126] C.-X. Mao, S. Gao, Y. Wang, Q.-X. Chu, X.-X. Yang, Dual-Band Circularly Polarized Shared-Aperture Array for C -/ X -Band Satellite Communications, IEEE Trans. Antennas Propag. 65 (2017) 5171–5178. https://doi.org/10.1109/TAP.2017.2740981.

[127] T. Ergin, N. Stenger, P. Brenner, J.B. Pendry, M. Wegener, Three-Dimensional Invisibility Cloak at Optical Wavelengths, Science (80-.). 328 (2010) 337–339. https://doi.org/10.1126/science.1186351.

[128] X. Hengbo, Design, simulation, and measurement of a multiband tunable metamaterial filter, Opt. Mater. (Amst). 127 (2022) 112253. https://doi.org/10.1016/J.OPTMAT.2022.112253.

[129] J. Lv, M. Zhou, Q. Gu, X. Jiang, Y. Ying, G. Si, Metamaterial Lensing Devices, Molecules. 24 (2019) 2460. https://doi.org/10.3390/molecules24132460.

[130] A.R. Azeez, T.A. Elwi, Z.A. Abed AL-Hussain, Design and analysis of a novel concentric rings based crossed lines single negative metamaterial structure, Eng. Sci. Technol. an Int. J. 20 (2017) 1140–1146. https://doi.org/10.1016/J.JESTCH.2016.11.010.

[131] M.R.I. Faruque, M.J. Hossain, S.S. Islam, M.F. Bin Jamlos, M.T. Islam, Design and analysis of a new double C-shaped miniaturized metamaterial for multiband applications, Appl. Phys. A Mater. Sci. Process. 123 (2017) 1–8. https://doi.org/10.1007/s00339-016-0727-y.

[132] M. Moniruzzaman, M.T. Islam, G. Muhammad, M.S.J. Singh, M. Samsuzzaman, Quad band metamaterial absorber based on asymmetric circular split ring resonator for multiband microwave applications, Results Phys. 19 (2020) 103467. https://doi.org/10.1016/j.rinp.2020.103467.

[133] A. Mohammad Siddiky, M. Rashed Iqbal Faruque, M. Tariqul Islam, S. Abdullah, M. Uddin Khandaker, Inverse double-C shaped square split ring resonator based metamaterial with multi-resonant frequencies for satellite band applications, Results Phys. 19 (2020). https://doi.org/10.1016/j.rinp.2020.103454.

[134] M.S.U. Afsar, M.R.I. Faruque, M.B. Hossain, A.M. Siddiky, M.U. Khandaker, A. Alqahtani, D.A. Bradley, A New Octagonal Close Ring Resonator Based Dumbbell-Shaped Tuning Fork Perfect Metamaterial Absorber for C-and Ku-Band Applications, Micromachines. 13 (2022). https://doi.org/10.3390/mi13020162.

[135] M.B. Hossain, M.R.I. Faruque, S.S. Islam, M.T. Islam, Modified double dumbbell-shaped split-ring resonator-based negative permittivity metamaterial for satellite communications with high effective medium ratio, Sci. Rep. 11 (2021) 19331. https://doi.org/10.1038/s41598-021-98703-4.

[136] M.R. Islam, M.T. Islam, M.S. Soliman, M.H. Baharuddin, K. Mat, A.M. Moubark, S.H.A. Almalki, Metamaterial based on an inverse double V loaded complementary square split ring resonator for radar and Wi-Fi applications, Sci. Rep. 11 (2021) 21782. https://doi.org/10.1038/s41598-021-01275-6.

[137] F. Urbani, Experimental analysis of novel single-sided left-handed metamaterial, IEEE Antennas Wirel. Propag. Lett. 9 (2010) 720–723. https://doi.org/10.1109/LAWP.2010.2058837.

[138] T.D. Karamanos, A.I. Dimitriadis, N. V. Kantartzis, Compact double-negative metamaterials based on electric and magnetic resonators, IEEE Antennas Wirel. Propag. Lett. 11 (2012) 480–483. https://doi.org/10.1109/LAWP.2012.2197170.

[139] A. Mallik, S. Kundu, M.O. Goni, Design of a novel two-rectangular U-shaped double negative metamaterial, in: 2013 Int. Conf. Informatics, Electron. Vis., IEEE, 2013: pp. 1–6. https://doi.org/10.1109/ICIEV.2013.6572646.

[140] M.M. Islam, M.T. Islam, M. Samsuzzaman, M.R.I. Faruque, N. Misran, M.F. Mansor, A miniaturized antenna with negative index metamaterial based on modified SRR and CLS unit cell for UWB microwave imaging applications, Materials (Basel). 8 (2015) 392–407. https://doi.org/10.3390/ma8020392.

[141] A. Sarkhel, D. Mitra, S. Paul, S.R.B. Chaudhuri, A compact meta-atom for dual band negative permittivity metamaterial, Microw. Opt. Technol. Lett. 57 (2015) 1152–1156. https://doi.org/10.1002/mop.29041.

[142] N.I. Landy, S. Sajuyigbe, J.J. Mock, D.R. Smith, W.J. Padilla, Perfect Metamaterial Absorber, Phys. Rev. Lett. 100 (2008) 207402. https://doi.org/10.1103/PhysRevLett.100.207402.

[143] J. Jiang, Y. Cao, X. Zhou, H. Xu, K. Ning, X. Xiao, Y. Lu, C. Ding, Y. Chen, J. Dong, Colloidal self-assembly based ultrathin metasurface for perfect absorption across the entire visible spectrum, Nanophotonics. 12 (2023) 1581–1590. https://doi.org/10.1515/nanoph-2022-0686.

[144] C.-H. Fann, J. Zhang, M. ElKabbash, W.R. Donaldson, E. Michael Campbell, C. Guo, Broadband infrared plasmonic metamaterial absorber with multipronged absorption mechanisms, Opt. Express. 27 (2019) 27917. https://doi.org/10.1364/OE.27.027917.

[145] H. Ozpinar, S. Aksimsek, Fractal interwoven resonator based penta-band metamaterial absorbers for THz sensing and imaging, Sci. Rep. 12 (2022) 19758. https://doi.org/10.1038/s41598-022-23390-8.

[146] W. Ma, Y. Wen, X. Yu, Y. Feng, Y. Zhao, Performance enhancement of uncooled infrared focal plane array by integrating metamaterial absorber, Appl. Phys. Lett. 106 (2015). https://doi.org/10.1063/1.4915487.

[147] Y. Hui, J.S. Gomez-Diaz, Z. Qian, A. Alù, M. Rinaldi, Plasmonic piezoelectric nanomechanical resonator for spectrally selective infrared sensing, Nat. Commun. 7 (2016) 11249. https://doi.org/10.1038/ncomms11249.

[148] Y. Li, W. Gao, L. Guo, Z. Chen, C. Li, H. Zhang, J. Jiao, B. An, Tunable ultra-broadband terahertz perfect absorber based on vanadium oxide metamaterial, Opt. Express. 29 (2021) 41222. https://doi.org/10.1364/OE.444761.

[149] M. Wu, X. Zhao, J. Zhang, J. Schalch, G. Duan, K. Cremin, R.D. Averitt, X. Zhang, A three-dimensional all-metal terahertz metamaterial perfect absorber, Appl. Phys. Lett. 111 (2017). https://doi.org/10.1063/1.4996897.

[150] X. Xu, R. Xu, Y.-S. Lin, A voltage-controllable VO2 based metamaterial perfect absorber for CO2 gas sensing application, Nanoscale. 14 (2022) 2722–2728. https://doi.org/10.1039/D1NR07746E.

[151] Y.J. Kim, Y.J. Yoo, J.S. Hwang, Y.P. Lee, Ultra-broadband microwave metamaterial absorber based on resistive sheets, J. Opt. 19 (2017) 015103. https://doi.org/10.1088/2040-8986/19/1/015103.

[152] S. Huang, Z. Xie, W. Chen, J. Lei, F. Wang, K. Liu, L. Li, Metasurface with multi-sized structure for multi-band coherent perfect absorption, Opt. Express. 26 (2018) 7066. https://doi.org/10.1364/OE.26.007066.

[153] X. Jia, X. Wang, Design of a polarization-independent, wide-angle, broadband visible absorber, J. Mod. Opt. 65 (2018) 129–135. https://doi.org/10.1080/09500340.2017.1380240.

[154] B. Wu, Z. Liu, G. Du, Q. Chen, X. Liu, G. Fu, G. Liu, Polarization and angle insensitive ultra-broadband mid-infrared perfect absorber, Phys. Lett. A. 384 (2020) 126288. https://doi.org/10.1016/j.physleta.2020.126288.

[155] J. Zhao, Y. Wang, Y. Zhu, W. Zhang, Y. Yu, Lithography-free flexible perfect broadband absorber in visible light based on an all-dielectric multilayer structure, Opt. Lett. 45 (2020) 5464. https://doi.org/10.1364/OL.404423.

[156] Z. Li, L. Stan, D.A. Czaplewski, X. Yang, J. Gao, Wavelength-selective mid-infrared metamaterial absorbers with multiple tungsten cross resonators, Opt. Express. 26 (2018) 5616. https://doi.org/10.1364/OE.26.005616.

[157] Z. Qin, X. Shi, F. Yang, E. Hou, D. Meng, C. Sun, R. Dai, S. Zhang, H. Liu, H. Xu, Z. Liang, Multi-mode plasmonic resonance broadband LWIR metamaterial absorber based on lossy metal ring, Opt. Express. 30 (2022) 473. https://doi.org/10.1364/OE.446655.

[158] Y. Huang, L. Liu, M. Pu, X. Li, X. Ma, X. Luo, A refractory metamaterial absorber for ultra-broadband, omnidirectional and polarization-independent absorption in the UV-NIR spectrum, Nanoscale. 10 (2018) 8298–8303. https://doi.org/10.1039/C8NR01728J.

[159] A.K. Azad, W.J.M. Kort-Kamp, M. Sykora, N.R. Weisse-Bernstein, T.S. Luk, A.J. Taylor, D.A.R. Dalvit, H.-T. Chen, Metasurface Broadband Solar Absorber, Sci. Rep. 6 (2016) 20347. https://doi.org/10.1038/srep20347.

[160] L. He, Y. Yi, J. Zhang, X. Xu, B. Tang, G. Li, L. Zeng, J. Chen, T. Sun, Z. Yi, A four-narrowband terahertz tunable absorber with perfect absorption and high sensitivity, Mater. Res. Bull. 170 (2024) 112572. https://doi.org/10.1016/j.materresbull.2023.112572.

[161] D.R. Smith, D.C. Vier, T. Koschny, C.M. Soukoulis, Electromagnetic parameter retrieval from inhomogeneous metamaterials, Phys. Rev. E - Stat. Nonlinear, Soft Matter Phys. 71 (2005) 1–11. https://doi.org/10.1103/PhysRevE.71.036617.

[162] Y. Zhu, B. Tang, C. Jiang, Tunable ultra-broadband anisotropic absorbers based on multi-layer black phosphorus ribbons, Appl. Phys. Express. 12 (2019) 032009. https://doi.org/10.7567/1882-0786/aaffe6.

[163] Y. Bai, L. Zhao, D. Ju, Y. Jiang, L. Liu, Wide-angle, polarization-independent and dual-band infrared perfect absorber based on L-shaped metamaterial, Opt. Express. 23 (2015) 8670. https://doi.org/10.1364/OE.23.008670.

[164] Y.I. Abdulkarim, A. Mohanty, O.P. Acharya, B. Appasani, M.S. Khan, S.K. Mohapatra, F.F. Muhammadsharif, J. Dong, A Review on Metamaterial Absorbers: Microwave to Optical, Front. Phys. 10 (2022). https://doi.org/10.3389/fphy.2022.893791.

[165] D. Wu, L. Lei, M. Xie, P. Xu, S. Xu, High-Performance Metamaterial Light Absorption from Visible to Near-Infrared Assisted by Anti-Reflection Coating, Photonics. 10 (2023) 998. https://doi.org/10.3390/photonics10090998.

[166] X.J. He, L. Wang, J.M. Wang, X.H. Tian, J.X. Jiang, Z.X. Geng, Electromagnetically induced transparency in planar complementary metamaterial for refractive index sensing applications, J. Phys. D. Appl. Phys. 46 (2013). https://doi.org/10.1088/0022-3727/46/36/365302.

[167] M. Wan, S. Yuan, K. Dai, Y. Song, F. Zhou, Electromagnetically induced transparency in a planar complementary metamaterial and its sensing performance, Optik (Stuttg). 126 (2015) 541–544. https://doi.org/10.1016/j.ijleo.2015.01.006.

[168] X. Lu, L. Zhang, T. Zhang, Nanoslit-microcavity-based narrow band absorber for sensing applications, Opt. Express. 23 (2015) 20715. https://doi.org/10.1364/oe.23.020715.

[169] Y. Cheng, H. Luo, F. Chen, R. Gong, Triple narrow-band plasmonic perfect absorber for refractive index sensing applications of optical frequency, OSA Contin. 2 (2019) 2113. https://doi.org/10.1364/osac.2.002113.

[170] S.N. Khonina, M.A. Butt, N.L. Kazanskiy, Numerical investigation of metasurface narrowband perfect absorber and a plasmonic sensor for a near-infrared wavelength range, J. Opt. (United Kingdom). 23 (2021). https://doi.org/10.1088/2040-8986/abf890.

[171] J. Wang, H. Feng, J. Zhang, Z. Zhang, C. Liu, D. Fang, L. Ran, Y. Gao, Polarization-insensitive metamaterial perfect absorber in near-infrared band based on trapezoidal silver array, Laser Phys. 33 (2023). https://doi.org/10.1088/1555-6611/ace70f.

[172] P. Sun, Q. Zhao, Y. Li, S. Liu, C. Su, J. Jiang, M. Yun, Y. Zhao, J. Wang, Dual high-Q resonance sensing for refractive index and temperature based on all-dielectric asymmetric metasurface, Opt. Commun. 554 (2024) 130134. https://doi.org/10.1016/j.optcom.2023.130134.

Contents lists available at ScienceDirect

Results in Optics

journal homepage: www.sciencedirect.com/journal/results-in-optics

Design and analysis of wavelength tunable metamaterial reflector

Ankit [a], Kamal Kishor [a], Ravindra Kumar Sinha [a, b, *]

[a] *TIFAC-Center of Relevance and Excellence in Fiber Optics and Optical Communication, Department of Applied Physics, Delhi Technological University, Bawana Road, Delhi 110042, India*
[b] *Gautam Buddha University, Greater Noida, Gautam Budh Nagar, Uttar Pradesh 201312, India*

ABSTRACT

This paper reports the design and performance characteristics of perfect reflector tunable metamaterial (MTM). The reported MTM parameters are optimized to achieve nearly 100 % reflection at resonance wavelength (λ_r) 1550 nm. The propagation characteristic of the proposed MTM structure was obtained by the finite element method (FEM). The electromagnetic parameters such as effective permittivity (ε_{eff}), effective permeability (μ_{eff}), and effective refractive index (η_{eff}) are calculated using Nicolson-Ross-Weir (NRW) method and analysed for the 1400–1700 nm wavelength range. It has been observed that the proposed MTM structure exhibits μ-negative (MNG) metamaterial characteristics as well as a negative effective refractive index at λ_r. Further, it has also been shown that by varying the number of arrays of unit cells and using a mirror image of the unit cell, the operating wavelength can be easily tuned as required for different applications. The overall perfect reflectance and the tunable performance of the proposed MTM has a potential applications in the design and development of compact photonic devices such as optical resonators and antennas.

1. Introduction

Metamaterial (MTM) is an area of tremendous scientific and technological importance with optical properties that are very different from ordinary materials (Islam et al., 2021; Liu and Zhang, 2011). These properties include negative refractive index (Smith et al., 2004), improved optical reflection, transmission (Fan et al., 2005), and absorption (Landy et al., 2008), etc. The materials can be classified as single negative, double negative, and double positive based on their effective permittivity (ε_{eff}) and effective permeability (μ_{eff}) parameters. The single negative (SNG) metamaterial can be further classified into two types, i.e., ε-negative (ENG) and μ-negative (MNG) metamaterial, in which either the effective permittivity or effective permeability is negative. Recently, many metamaterial unit cell structures, such as H-shaped, modified H-shaped, I-shaped, oval-shaped, dumbbell-shaped etc, have been proposed (Askari et al., 2018; Hossain et al., 2018; Kishor et al., 2015; Idrus et al., 2022; Hossain et al., 2021). For instance, tunable negative refractive index metamaterial (Kishor et al., 2014), biosensing (Alizadeh et al., 2022), terahertz absorber (Nourbakhsh et al., 2020), antenna (Bai et al., 2020), refractive index and temperature sensor (Agarwal et al., 2022) and invisibility cloaking (Paul et al., 2012)

are the applications of these MTM structures.

Over the last two decades, metamaterials have realized various fascinating electromagnetic properties, covering a vast operating frequency from GHz (Vendik and Vendik, 2013) and THz (Xu et al., 2017) to infrared and visible regions. The core of the early research at GHz and THz used the electric-dipole resonance in metallic wires and the magnetic-dipole resonance in the split-ring resonator (SRR) to achieve negative permittivity and negative permeability, respectively (Smith et al., 2000). Due to the loss associated with resonant metallic structures, it has often been difficult to apply these metamaterial design concepts to geometry with submicron or nanoscale in the infrared and optical frequency ranges (Xiao et al., 2010). Another approach to produce electric or magnetic resonances with less loss is based on the interaction of electromagnetic waves with dielectric particles with a wide range of potential photonic devices such as perfect reflectors (O'Brien and Pendry, 2002; Zhao et al., 2009). Instead of using metallic mirrors, Bragg reflectors can also achieve high reflectivity. The main drawback of Bragg reflectors is that they require large number of layers to obtain the necessary reflectivity; therefore, the deposition of various dielectric materials is a time-consuming procedure that raises the cost of the product (Slovick et al., 2013). The benefit of MTM over metallic mirrors

Design, fabrication, and characterization of epsilon negative and near-zero index metasurface

Ankit[1] · Kamal Kishor[1] · Ravindra Kumar Sinha[1,2]

Abstract

This paper delves into the intricacies of designing, fabricating, and characterizing a metasurface exhibiting epsilon-negative (ENG) and near-zero index (NZI) properties. Specifically, it focuses on an eye-shaped coupled circular split ring resonator (CC-SRR) metasurface, crafted from copper on an epoxy resin fiber (FR-4) dielectric substrate material. The design is further optimized to induce resonance frequencies at approximately 7.5, 8.8, and 13.4 GHz within the C, X, and Ku bands, respectively. Utilizing the COMSOL Multiphysics and CST Microwave Studio simulation tools, the structural design is developed to ascertain its electromagnetic properties across the 1–15 GHz frequency spectrum. Experimental measurements of the transmission characteristics of the fabricated metasurface align closely with the simulated results. The electromagnetic field distributions of the proposed metasurface structure are scrutinized, revealing tunable characteristics contingent upon variations in the thickness (t_s) of the dielectric substrate material and the copper resonator thickness (t_m). Additionally, a theoretical model employing an equivalent circuit, featuring various inductor (L) and capacitor (C) components, is presented to compare against simulated results for the targeted resonance frequencies.

Keywords Coupled circular split ring resonator (CC-SRR) · Dielectric · Epsilon negative (ENG) · Finite element method (FEM) · Metasurface · Near-zero index (NZI)

1 Introduction

Metasurfaces have indeed earned significant attention from experts worldwide due to their unique properties and potential applications, particularly in the microwave frequency spectrum. These are artificial structures designed to exhibit properties not found in naturally occurring materials [1]. They are two-dimensional artificial structures created by arranging subwavelength unit cells in a specific pattern to achieve the desired electromagnetic properties. The unit cell configuration of the metasurface typically involves a periodic array of metal-dielectric or metal-dielectric-metal structures on a host substrate [2]. The metal components,

often in the form of split-ring resonators (SRR) or wire structures, provide the desired electromagnetic response, while the dielectric materials help control and manipulate the propagation of electromagnetic waves. In 1968, Russian physicist Victor Veselago first proposed the theoretical concept of Double negative (DNG) metamaterial or Left-handed metamaterial (LHM), which is a hypothetical "ε-negative and μ-negative" metamaterial [3]. In 1996, Pendry et al. introduced thin metal wire-based structures to realize negative permittivity [4]. In 1999, Pendry et al. [5] also introduced SRR metamaterial unit cells which could provide negative permeability and were easy to construct. Depending on the values of the effective permittivity and effective permeability parameters of the designed metasurface structure, it can be categorized as single-negative (SNG), DNG, and double-positive materials. The SNG materials show either negative permeability or negative permittivity, whereas double-negative (DNG) materials show both negative characteristics [6]. Another type of metamaterial category is near-zero index (NZI) metamaterials which represent a fascinating class of engineered materials that exhibit an effective refractive index close to zero. Unlike conventional materials,

✉ Ravindra Kumar Sinha
  dr_rk_sinha@yahoo.com

[1] TIFAC-Center of Relevance and Excellence in Fiber Optics and Optical Communication, Department of Applied Physics, Delhi Technological University, Delhi 110042, India

[2] Gautam Buddha University, Gautam Budh Nagar, Greater Noida, UP 201312, India

Springer

SOI Based metasurface for broadband perfect reflection in visible spectrum

Ankit[1], Kamal Kishor[1] and Ravindra Kumar Sinha[1,2,*]

[1] TIFAC-Center of Relevance and Excellence in Fiber Optics and Optical Communication, Department of Applied Physics, Delhi Technological University, Delhi 110042, India
[2] Gautam Buddha University, Greater Noida, Gautam Budh Nagar UP-201312, India

E-mail: dr_rk_sinha@yahoo.com

CrossMark

Abstract
We propose modeling and design of a low-loss all-dielectric metasurface (DM), comprised of Silicon on Insulator (SiO_2) substrate to demonstrate a perfect reflector in the visible spectrum. The proposed metasurface unit cell consists of V and W shapes arranged in a mirror image configuration, with nanometre-sized gaps (g) between them. A narrow peak with a nearly 100% reflectance and a broad perfect reflection spectrum is observed within the visible region (400–700 nm) of the electromagnetic spectrum. The effective electromagnetic parameters were also analyzed for electric and magnetic dipole resonance. The electric and magnetic field distributions at the resonant wavelength were also analyzed for the proposed structure. By altering the gap region 'g', the thickness of the dielectric Silica layer (t_s), and the Si resonator (t_m), the proposed structure exhibits tunable characteristics. We have successfully illustrated the consistent position of the scattering parameter's response, regardless of the structure's rotation, concluding the homogeneity of the designed structure across the entire visible spectrum. The all-DM exhibits a unique combination of features, including a distinct and wide reflectance spectrum as well as a tuned and enhanced electric field which makes it an ideal platform for the applications in filters, color printing, low-loss slow-light devices, and nonlinear optics.

Keywords: dielectric, electric field, electric dipole (ED), magnetic dipole (MD), metasurface, silicon on insulator (SOI)

1. Introduction

Metasurfaces have indeed earned significant attention in recent years because of their unique ability to manipulate electromagnetic waves. They are constructed from subwavelength structures known as meta-atoms or meta-molecules, which are carefully engineered to exhibit desired electromagnetic properties [1]. Metasurfaces offer a wide range of applications due to their ability to exhibit properties such as negative permeability and permittivity [2, 3], tunable negative refractive index [4], and other fascinating characteristics such as perfect lenses [5], antennas [6], temperature and refractive index sensor [7] and perfect reflectors [8] etc. In many

cases, some metallic resonators, e.g. Metallic split-ring resonators (MSRR) [9] and metallic cut-wire arrays [10], are indeed widely used in the design of metamaterials. Split-ring resonators produce magnetic dipole (MD) resonances, while cut-wire arrays generate electric dipole (ED) resonances. These structures have proven to be effective in manipulating electromagnetic waves at gigahertz, terahertz, and n-IR wavelengths. The high absorption loss in metal-based metamaterials poses a challenge for their use in photonics applications, where low energy dissipation is crucial for efficient light manipulation and transmission. In such applications, it becomes necessary to explore alternative materials or strategies to overcome this limitation. One approach is to explore alternative materials that exhibit lower losses in the desired spectral range. For instance, dielectric materials can be employed instead of metals to reduce energy dissipation [11]. Dielectric resonators

* Author to whom any correspondence should be addressed.

1

Quadrupole mode plasmon resonance enabled dual-band metamaterial for refractive index sensing application

Ankit,[1] Monu Nath Baitha,[2] Kamal Kishor,[1] and Ravindra Kumar Sinha[1,3,a]

AFFILIATIONS

[1]TIFAC—Center of Relevance and Excellence in Fiber Optics and Optical Communication, Department of Applied Physics, Delhi Technological University, Delhi 110042, India
[2]School of Mechanical Engineering, Yonsei University, 50 Yonsei-ro, Seodaemun-gu, Seoul 03722, Republic of Korea
[3]Gautam Buddha University, Gautam Budh Nagar, Greater Noida, UP 201312, India

[a]Author to whom correspondence should be addressed: dr_rk_sinha@yahoo.com

ABSTRACT

In this paper, design and fabrication of a dual-band near-zero index metamaterial (MTM) structure using copper on an epoxy resin fiber (FR-4) dielectric substrate is reported for refractive index sensing applications. The primary objective is to achieve dual-band operation spanning a 1–15 GHz frequency range, with a specific focus on achieving a broad bandwidth in the C-band. The resonance of the MTM structure was ascribed to the coupling of plane electromagnetic waves with surface plasmon polaritons on the structure, resulting in a quadrupole plasmon resonance mode. Furthermore, transmission characteristics of the fabricated MTM structure were experimentally measured and found to align closely with the simulated results obtained through the finite element method in COMSOL Multiphysics. The designed MTM structure demonstrates negative and near-zero permittivity at resonance frequencies, enabling left-handed and near-zero index behavior in dual microwave frequency bands. Under room temperature conditions, the MTM sensor exhibited sensitivities of 1 GHz/RIU and 3 GHz/RIU at resonance frequencies of 2.7 and 7.3 GHz, respectively. Consequently, the MTM structure exhibits significant potential for diverse applications, serving as a valuable component in sensors, detectors, and optoelectronic devices operating in the GHz region.

I. INTRODUCTION

The S (2–4 GHz) band and the C (4–8 GHz) band hold significant importance across a spectrum of applications due to the unique electromagnetic characteristics of these frequency ranges. Modern optoelectronic devices developed for these bands are essential for various purposes, including wireless communications,[1] radar navigation,[2] remote sensing,[3] etc. However, effective utilization of the S and C bands often encounters challenges, primarily associated with the limitations of conventional materials and components in achieving the desired performance levels. These limitations can impede progress in the above-mentioned application and beyond. Metamaterials (MTMs) represent a groundbreaking solution that has revolutionized the world of electromagnetic engineering. These artificially engineered materials are engineered to manipulate electromagnetic waves in unconventional ways that were previously thought impossible.[4–6] One of the most remarkable feats achieved by metamaterials is the creation of a negative refractive index, allowing waves to bend in unconventional directions.[7] However, the evolution of metamaterials extends beyond this milestone, delving into the realm of zero-index materials—a cutting-edge development within the field. The zero-index metamaterials (ZIMs), a subset of metamaterials, present unique advantages that render them highly valuable for applications such as electromagnetic cloaking, tunneling, and beam splitting.[8] With a refractive index of zero, these materials exhibit remarkable properties that can significantly enhance the performance and efficiency of devices across various frequency ranges. These capabilities open new avenues for manipulating and controlling electromagnetic waves, promising a new range of advantages and applications that go beyond the capabilities of conventional materials.

applied optics

Design and analysis of a far-infrared metamaterial perfect absorber with sensing applications

ANKIT,[1] ⬤ KAMAL KISHOR,[1] ⬤ AND RAVINDRA KUMAR SINHA[1,2,*] ⬤

[1]*TIFAC-Center of Relevance and Excellence in Fiber Optics and Optical Communication, Department of Applied Physics, Delhi Technological University, Delhi-110042, India*
[2]*Gautam Buddha University, Gautam Budh Nagar, Greater Noida, UP-201312, India*
*dr_rk_sinha@yahoo.com

In this paper, we present an analysis and design of a metamaterial as the perfect absorber and refractive index sensor in the far-infrared (IR) region, utilizing the finite element method (FEM). The structure consists of a metal resonator on a silicon dielectric with a bottom copper layer beneath the dielectric. Our results demonstrate that the designed structure achieves nearly perfect absorption of transverse electric (TE) polarization at a resonance wavelength of $\lambda_r = 9.40\ \mu m$. This occurs because of the perfect impedance matching condition, which achieves a 99.47% absorption efficiency. This condition is also sensitive to the angle of incidence and causes minimal reflection at the resonating wavelength of λ_r. This characteristic makes the designed metamaterial structure suitable for use as a sensor. The structure enables maximum electric field confinement in the gap region (g) of the split ring resonator (SRR) at the metal-dielectric interface. The resonance wavelength can be effectively tuned and optimized by varying the gap size (g), dielectric material, dielectric thickness (t_d), copper layer thickness (t_c), and incident angle of the metamaterial absorber (MA). The absorption peak shows a highly sensitive response to changes in the refractive index of the surrounding medium, with a sensitivity of 1600 nm/RIU. This absorber, with its excellent absorption in the far-IR spectrum, holds promising potential for applications in energy harvesting and IR sensing.

1. INTRODUCTION

Metamaterials are artificial subwavelength electromagnetic materials with unique properties that are not found in natural materials [1]. Their electromagnetic responses are primarily determined by the materials and microstructures of their resonant units. By designing these resonant unit structures, metamaterials enable free control of electromagnetic waves, overcoming the modulation limitations of natural materials at the atomic or molecular level. These distinctive properties make metamaterials suitable for a variety of applications, including electromagnetic cloaking [2], tunable negative refractive indices [3], metalenses [4], perfect reflectors [5,6], communication [7,8], sensors [9], and refractive index sensing applications with quadrupole mode plasmon resonance [10]. One specific application of metamaterials is as perfect absorbers, achieving nearly complete absorption over specific frequency bands. Metamaterial perfect absorbers (MPAs) have gained significant interest recently. Based on absorption bandwidths, MAs can be categorized into broadband and narrowband absorbers. MAs are classified as either broadband or narrowband absorbers based on their absorption bandwidths. While narrowband absorbers are frequently employed for sensing and coherent heat radiation

[11,12], broadband absorbers are perfect for solar cells [13]. Better coherence and higher sensitivity are often provided by narrower absorption bandwidths.

Metamaterial absorbers (MAs) in the microwave regime were first proposed in 2008 by Landy *et al*. [14]. Since then, this field has advanced significantly. Numerous MAs with various microstructures have been reported, advancing the research on metamaterial perfect absorbers (MPAs) across different frequency ranges, including visible light [15], infrared [16], and terahertz frequencies [17,18]. A crucial area of research is far-wavelength infrared (FWIR) MPAs, which are vital for photothermal applications, especially in IR imaging [19] and sensing [20]. The development of metamaterial perfect absorbers has been rapid, thanks to continuous research efforts [21–23]. These absorbers have undergone design evolution from narrowband to broadband, polarization-sensitive to polarization-insensitive, and single-frequency to multi-frequency. Furthermore, they now cover the entire spectral range, including microwave [24], terahertz [25], visible [26], and infrared frequencies [27,28]. Efforts to enhance the efficiency and broaden the absorption bandwidth of FWIR MPAs

Physica Scripta

PAPER

Design of wide bandwidth metamaterial for biosensor and wireless application

Ankit[1] , Kamal Kishor[1] and Ravindra Kumar Sinha[1,2]

[1] TIFAC-Center of Relevance and Excellence in Fiber Optics and Optical Communication, Department of Applied Physics, Delhi Technological University, Delhi-110042, India
[2] Gautam Buddha University, Greater Noida, Gautam Budh Nagar, UP-201312, India

E-mail: dr_rk_sinha@yahoo.com

Abstract

We present a new design and study of metamaterial (MTM) structure for wide bandwidth for biosensor and wireless applications. The geometrical parameters were analyzed and optimized for a triple-band operation in the frequency range of 0.1–16 GHz. The propagation characteristics were obtained using Finite element method. The proposed MTM provides negative permittivity at 1.4 GHz and negative permeability in the 9–16 GHz region. The proposed design exhibits left-handed characteristics in L, C, and Ku microwave region's frequency band. The electric field (E), magnetic field (H), and surface current distribution of the proposed MTM unit cell have been studied at three different resonance frequencies. The proposed MTM design has a wide bandwidth of 2.2 GHz in C-band and a high effective medium ratio (EMR) of 13.37. The performance of the sensor is evaluated for different biomedical samples in the refractive index range of 1.00 to 1.39. The results indicate that the proposed biosensor has a high sensitivity in triple band of microwave region. The present research work can be highly suitable for Wi-Fi and satellite applications due to its overall performance, including wide bandwidth in the C-band, high EMR, and triple band operation.

1. Introduction

Metamaterial (MTM) are defined as artificial composite materials with unique electromagnetic properties not found in nature and are made by arranging small metallic resonators periodically [1]. Recent advancements in metamaterials have opened up new avenues for applications in photonics and electromagnetic device engineering, including the development of toroidal metaphotonics and metadevices, which exhibit unique electromagnetic properties and functionalities [2]. Victor Veselago [3] first portrayed materials with negative permittivity (ε) and permeability (μ) in 1968; however, these characteristics were largely ignored until 1999. In 2000, Smith *et al* proposed metallic split-ring resonators (SRRs) with unit cell dimensions lesser than the operating wavelength [4]. They developed a composite structure in which permittivity and permeability both are negative, represented as Left-handed metamaterials (LHM). The characteristics of effective permittivity (ε_{eff}) and effective permeability (μ_{eff}) allow the materials to be categorised as single negative (SNG), double negative (DNG) [5], or double positive. Both ε-negative (ENG) and μ-negative (MNG) metamaterials are SNG metamaterials in which one of the two properties- ε_{eff} or μ_{eff} -is negative [6]. The spread of metamaterial research to GHz and THz and which revealed MTM's unique characteristics such as negative permittivity (ε), negative permeability (μ), and negative refractive index (n), has led to a wide range of applications in microwave and optical regimes such as perfect reflector [7, 8], reconfigurable antenna [9], metalens [10], satellite [11], dual band sensors [12], invisibility cloaking [13], refractive index sensors [14–16], filters [17], perfect absorbers [18] and superlenses [19], circular dichroism [20] etc MTMs have recently originated with utilization in various frequency bands, as every frequency band has a diverse range of applications. For instance, in the microwave region, the L-band covers frequencies between 1–2 GHz with the usage in RADAR and satellite broadcasting applications, the S-band covers frequencies between 2–4 GHz, the C-band covers frequencies between 4–8 GHz

125

DELHI TECHNOLOGICAL UNIVERSITY

(Formerly Delhi College of Engineeering)

Shahbad Daulatpur, Main Bawana Road, Delhi-42

PLAGIARISM VERIFICATION

Title of the Thesis   "**Metamaterial based Optical Devices: Design and Analysis**"   .

Total Pages   **150**   Name of the Scholar   **Ankit**   .

Supervisor (s)

(1)   **Prof. Ravindra Kumar Sinha**   .

(2)   **Dr. Kamal Kishor**   .

Department of   **Applied Physics**   .

This is to report that the above thesis was scanned for similarity detection. Process and outcome is given below:

Software used: **Turnitin**   Similarity Index: **3%**   , Total Word Count: **24363**

Date: 24 April 2025

Candidate's Signature   **Signature of Supervisor(s)**

Mr. Ankit

Ward No. 15, Navjeevan Hospital,
Dwarka Colony Near ICS Coaching Centre
Gohana, Distt. Sonipat (HRY), India - 131301
📞 +91-9215331128 · ✉ ankitphdap@gmail.com

www.linkedin.com/in/ankit-73b482258

https://scholar.google.com/citations?user=-IPUSTcAAAAJ&hl=en

https://www.researchgate.net/profile/Ankit-14/stats

Education

Program	Institution	Division	Year
Ph.D. **(Applied Physics)**	**Delhi Technological University, Delhi**	—	**2025**
M.Sc. **(Physics)**	**Hindu College Sonipat, Haryana**	**First**	**2018**
B.Sc. **(Physics, Chemistry, Mathematics)**	**NRS College Rohtak, Haryana**	**First**	**2016**

Publications

1. **Ankit**, K. Kishor, R.K. Sinha, Design and analysis of wavelength tunable metamaterial reflector, **Results Opt.** 10 (2023) 100366.
2. **Ankit**, K. Kishor, R.K. Sinha, Design, fabrication, and characterization of epsilon negative and near-zero index metasurface, **Appl. Phys. A.** 130 (2024) 98 (I.F.= 2.7).
3. **Ankit**, K. Kishor, R.K. Sinha, SOI Based metasurface for broadband perfect reflection in visible spectrum, **J. Opt.** 26 (2024) 045101 (I.F.= 2.1).
4. **Ankit**, M.N. Baitha, K. Kishor, R.K. Sinha, Quadrupole mode plasmon resonance enabled dual-band metamaterial for refractive index sensing application, **J. Appl. Phys.** 136 (2024) 023104 (I.F. = 2.7)
5. **Ankit**, K. Kishor, R.K. Sinha, Design of wide bandwidth metamaterial for biosensor and wireless application, **Phys. Scr.** 100 (2025) 035503 (I.F. = 2.6)
6. **Ankit**, K. Kishor, R.K. Sinha, Design and analysis of Far-Infrared Metamaterial Perfect Absorber with sensing applications, **Appl. Opt.** 63, 8994-9001 (2024) (I.F. = 1.7)

7. **Ankit**, K. Kishor, and R. K. Sinha, "ENZ metamaterial for X-band in the microwave regime," in Frontiers in Optics + Laser Science 2022 (FIO, LS), Technical Digest Series (Optica Publishing Group, 2022), paper JTu4B.60.

8. **Ankit .,** Kamal Kishor, Ravindra Kumar Sinha, "Design and analysis of multiband metamaterial in microwave regime," Proc. SPIE 12568, Metamaterials XIV, 125680V (6 June 2023).

Workshops/Seminars/Conferences attended/participated

1. High-End workshop (Karyashala) on "Recent Advances in Microwave & Millimeter-Wave Communication Technologies" sponsored by SERB organized by the Department of Electrical Engineering, IIT Indore from November 21- November 27, 2022.

2. A technical talk on "Stronger Glass Products and an Overview of IYoG (International Year of Glass)" organized by Department of Applied Physics, DTU in association with The All-India Glass Manufacturers' Federation (AIGMF) on 30th November 2022.

3. One Day National Seminar on "Implementation of NEP-2020 in special reference to innovation & entrepreneurship" organized by the Department of Applied Physics, Delhi Technological University (DTU) on February 24, 2023.

4. "SPIE OPTICS+OPTOELECTRONICS 2023" International conference in Prague, Europe during 23rd - 27th Apr 2023 and successfully presented the poster presentation titled "Design and analysis of multiband metamaterial in microwave regime".

5. One Day National Workshop on "Ascertaining A Skill Centre for Glass and Glazing (ASCGG-2023) Bringing Industry and Academia Together organized by Department of Applied Physics, DTU on August 11, 2023.

6. "Optica Student Leadership Program-2023" in Tacoma, Seattle US during 08th - 12th Oct 2023.

7. "International Conference on Atomic, Molecular, Material, Nano and Optical Physics with Applications" International conference in DTU during 20th - 23rd Dec 2023 and successfully presented the poster presentation titled "A Comprehensive Design and study of microwave Zero Index metasurface".

8. "2022 Frontiers in Optics + Laser Science" Virtual Conference and presented poster entitled "ENZ metamaterial for X-band in the microwave regime" online during 17th - 20th Oct 2022.

9. High-End workshop (Karyashala) on "**Opportunistic control of Advances in Antenna Design**" sponsored by SERB organized by the Department of Electrical Engineering, NIT Tiruchirappalli from March 11- March 17, 2024.

National/State level Achievements

◊ Qualified GATE Physical Sciences (2019).

Technical Skills

◊ Operating System: Windows
◊ Tools: Microsoft Office
◊ Software Skill: Origin, COMSOL Multiphysics, CST Microwave Studio, Mendeley, MATLAB

Others

◊ Hobbies: Travelling, Cricket, Meditation
◊ Languages: English, Hindi

Declaration

I do hereby declare that all the details furnished above are true to the best of my knowledge and belief.

Place: Delhi, (India)
Date: (Ankit)